NANOGENEARTORS FOR MECHANICAL ENERGY HARVESTING AND SELF-POWERED SENSOR NETWORKS

A Dissertation
Presented to
The Academic Faculty

by

Long Lin

In Partial Fulfillment
of the Requirements for the Degree
Doctor of Philosophy in the
School of Materials Science and Engineering

Georgia Institute of Technology
August 2015

NANOGENEARTORS FOR MECHANICAL ENERGY HARVESTING AND SELF-POWERED SENSOR NETWORKS

Approved by:

Dr. Zhong Lin (Z.L.) Wang, Advisor
School of Materials Science and Engineering
Georgia Institute of Technology

Dr. Russell D. Dupuis
School of Electrical and Computer Engineering
Georgia Institute of Technology

Dr. David McDowell
School of Materials Science and Engineering
Georgia Institute of Technology

Dr. Yulin Deng
School of Chemical and Biomolecular Engineering
Georgia Institute of Technology

Dr. Preet Singh
School of Materials Science and Engineering
Georgia Institute of Technology

Date Approved: June 12, 2015

In memory of Dr. Robert L. Snyder

ACKNOWLEDGEMENTS

First of all, I would like to express my sincere gratitude to my advisor, Dr. Zhong Lin Wang, for his helpful guidance in my research and kind care of my personal life. As our group leader, he is our best role model for his solid physics and microscopy background, persistence in research, tremendous diligence and excellent working efficiency, and pioneering scientific visions; as my advisor, he always supports and encourages me without any doubt. I also want to take this chance to thank and memorize Dr. Snyder, who has been my advisor for one year, but I will always remember his positive attitude and kind smile. My best thank also goes to my committee members, including Dr. McDowell, Dr. Singh. Dr. Deng, Dr. Dupuis, and Dr. Summers for their insightful advice on my doctoral research and thesis, without which the quality of this dissertation cannot be guaranteed.

It is my great honor to join this research group with lots of kind and talented scholars. I received a lot of help from my friends in this group. Dr. Youfan Hu was my first mentor and she taught me everything about our research from the very beginning, when I was a fresh student with almost no experience about working in the lab. I have known Dr. Sihong Wang since nine years ago, and he is always my big brother and took good care of me when I came to this country for the first time. I feel fortunate to meet Dr. Fengru Fan and work with him on the original invention of triboelectric nanogenerator, which constitutes the core topic of my thesis. Besides, I would like to thank Drs. Yannan Xie, Simiao Niu, Yong Ding, Jinhui Song, Sheng Xu, Chen Xu, Yan Zhang, Caofeng Pan, Ya Yang, Guang Zhu, Yunlong Zi, Wenzhuo Wu, Xiaonan Wen, Yusheng Zhou,

Ying Liu, Ruomeng Yu, Jun Chen, Chen-Ho Lai, Qingshen Jing, Xue Wang, Jung-Il Hong, Sangmin Lee, Ken Pradel, Po-Kang Yang, Fang Yi, Li Zheng, Min-Hsin Yeh, Zong-Hong Lin, Gang Cheng, Wenxi Guo, Tiejun Zhang, Yolande Berta, and many others, for their kind help in both my research and my personal life.

Last but most importantly, I would like to thank my loved ones. My parents, Jiwu Lin and Jing Wang, gave me the best care in my childhood and offered me important education opportunities in high school. It's their unconditional love that made me who I am today. I also appreciate the love and care from my gorgeous wife, Dr. Baiyu Yang, who gives me a comfortable and warm home in a foreign country. I am really grateful and delightful to share my life with her.

TABLE OF CONTENTS

LIST OF FIGURES

SUMMARY

The worldwide energy issues and internet of things have driven long term interests to develop renewable energy sources. In this regard, the invention of nanogenerators provides us new insights on scavenging wasted mechanical energy from the ambient environment, and convert kinetic agitations into electricity for powering electronic devices. Piezoelectric nanogenerator was developed from the coupling of piezoelectric and semiconductor properties of ZnO nanowires, and its output performance has been improved by vertical integration, annealing, and surface functionalization of the nanowires. Triboelectric nanogenerators (TENG) work on the basis of contact electrification and electrostatic induction. Four fundamental working modes have been developed for various mechanical motions, and a high output power density of 35.6 W/m^2, an excellent energy conversion efficiency of up to 55%, and terrific output stability of over 300,000 cycles have been accomplished with the state-of-the-art TENG devices. The niche applications of the TENGs have been demonstrated for powering portable electronics toward the goal of fully-integrated self-powered system. Both nanogenerators were further employed as self-powered/active sensors without an external power supply, and multiple functions could be achieved including pressure detection and motion sensing. Both static and dynamic pressure sensing was realized using the open-circuit voltage and short-circuit current from the TENG, respectively. A high sensitivity of 0.31 kPa^{-1} and a low detection limit of 2.1 Pa were also fulfilled. The integration of pressure sensor array for tactile imaging was further demonstrated for its potential application in electronic skin, human-machine interface, and security monitoring.

CHAPTER 1

INTRODUCTION

1.1 Motivation

The worldwide energy crises problem has driven long-lasting attentions from scientific research and technological innovations.[1, 2] On the large scale, traditional fossil fuels (coal, gasoline, and natural gas) are running out due to the fast-growing industrialization and urbanization. Moreover, along with their benefits to provide us power for industry production or daily life usage, the incomplete combustion of fossil fuels will lead to severe environmental issues like air pollution. Considering these side effects, development of alternative clean energy sources is highly desirable for sustainable development. On a smaller scale, the fast development of internet of things (IoTs)[3, 4] introduces huge amount of tiny electronic devices with multiple functionalities, wide-spread availability, and network connectivity. However, its power source requirement may not be fulfilled by traditional power supply due to connection problems, and batteries will be limited for low lifetime and high cost of installation and replacement. In this regard, harvesting energy from the ambient environment and convert it into electricity will be a reasonable solution to solve the above-mentioned problems, with approaches like solar cells,[5-7] bio-fuel cells,[8-10] and thermoelectric cells.[11-13] However, most of the existing techniques have their own limitations. For instance, the performance of a solar cell is highly dependent on the weather or illumination conditions, making it unable to provide constant output during the night or severe weather conditions.

Mechanical energy exists in forms of vibrations, human walking, tire rotation, automobiles, etc., which is a universally available and pollution-free energy source. Such versatile mechanical energy could be scavenged at any time and in any place. Various approaches have been developed to effectively convert the mechanical energy into electricity for applications, such as those techniques based on the piezoelectric,[14-17] electromagnetic,[18-20] and electrostatic effects.[21-23] However, most of the existing techniques aim at the energy harvesting from a large scale, which makes the energy-harvesting equipment large and cumbersome, and not convenient for use in some circumstances like to power up the nano-scale electronics, implanted biosensors, and micro/nano-robots. Hence, developing new types of mechanical energy harvester with miniaturized size, convenient fabrication, and low cost is a core challenge in the state-of-art research of this field.

1.2 Mechanical energy harvesting

An electromagnetic generator usually consists of a magnet on a polyimide spring. When the generator is vibrated, there will be a net movement between the magnet and the housing component. The relative displacement can be employed to produce electrical output based on the magnetic induction between the magnet and the planar pick-up coil. As can be found from multiple types of the electromagnetic generator, the magnet and pick-up coils are key components for the energy harvesting process. The device structure of a typical example of the recently developed electromagnetic generator can be found in Figure 1.1a, which was miniaturized from previous design.[19] This design employed four magnets composed of sintered NdFeB, which were manually bonded to the top and

bottom surfaces of a cantilever beam. The measured output performance was taken in Figure 1.1b. The output power could reach 10.82 μW as the working frequency of the cantilever beam was increased to 58.5 Hz. Saha *et al.*[24] also reported a magnetic spring generator for harvesting energy from human motions, but the normalized power output was limited by the high damping loss, which was caused by the friction between moving magnet and the tube surface.

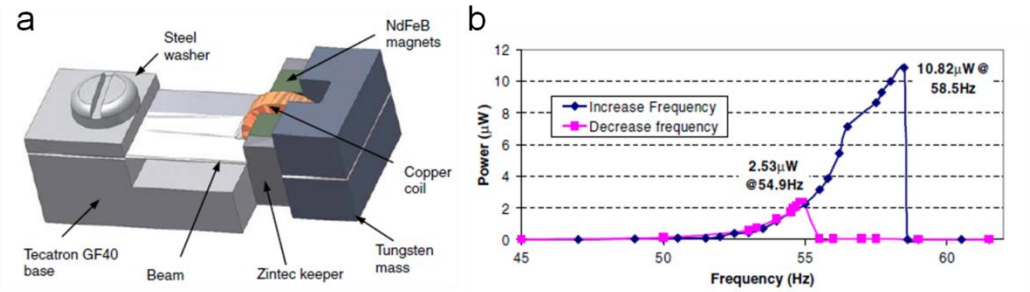

Figure 1.1 (a) The device structure of a typical electromagnetic generator. (b) The power output hysteresis effect of the micro-electromagnetic generator.[19]

The traditional electrostatic generator was utilized to produce static electricity at high voltage and low continuous current, such as the Wehrsen Machine, and the Van de Graaff generator.[21] Recent efforts have been made to minimize the total size of the generator for more specific application, like in micro-electro-mechanical system (MEMS). For example, Suzuki *et al.*[25] developed an in-plane electrostatic generator based on electrets materials, which were separated by a passive spacing gap. As displayed in Figure 1.2a, a patterned electrets material was employed to induce a repulsive electrostatic force, and a dual-phase electrode arrangement is adopted in order to reduce the horizontal electrostatic damping force. With such design, a power output of 0.56 μW could be produced (Figure 1.2b).

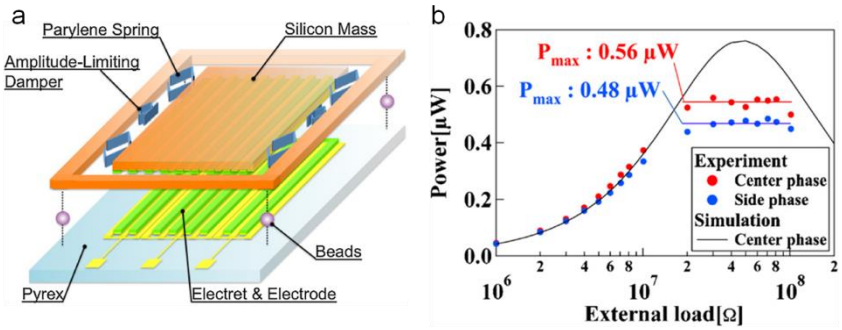

Figure 1.2. (a) The schematic structure of a typical electrostatic generator. (b) The measured output power of the electrostatic generator with variable loading resistances.[25]

1.3 Thesis scope

In this thesis, my major goal is to develop new approaches for mechanical energy harvesting with high output power, high stability, low cost, and small size. The recently invented piezoelectric nanogenerator and triboelectric nanogenerator have their unique advantages over conventional technologies, though restrictions also apply to each of them. For piezoelectric nanogenerator, its fundamental theory and basics have been well established, while the output power still needs to be boosted up for powering electronic devices, especially for the low output voltage of the single-nanowire-based nanogenerator. On the other hand, triboelectric nanogenerators have the potential to produce higher output power with much less materials limitations, but its fundamental mechanism and working modes still need to be established.

In my doctoral research, I was dedicated to improving the performance for both the piezoelectric and triboelectric nanogenerators. For piezoelectric nanogenerator, its output performance was improved by vertical integration and horizontal assembly of semiconductor nanowires. On the basis of the integrated nanogenerator, more endeavors were devoted to refrain the free carrier density (mainly free electrons for n-type ZnO

nanowires) by oxygen plasma treatment, thermal annealing, and surface functionalization of the nanowires. Its output voltage could be enhanced to 20 V, and the improved output enabled the nanogenerator to power up small electronic devices like a liquid-crystal display or electronic watch. For triboelectric nanogenerator, its working mechanism was clarified as the coupling of contact electrification and electrostatic induction. Four fundamental working modes were developed with their unique features and applicable scenarios. The output performance was optimized by two approaches. Micro-patterned surface modifications were employed to improve the triboelectric charge density, and advanced structural designs were adopted to facilitate the charge separation process. By combining the above two approaches, a few novel prototypes were fabricated to deliver a high output power density of 35.6 W/m^2, a huge instantaneous energy conversion efficiency of 55%, and outstanding output stability and device durability of up to 300,000 cycles.

The practical applications of nanogenerators can be divided into two parts, self-powered system and active sensors. The output of nanogenerators was employed for directly powering portable electronics, and it could also be integrated with energy storage unit to continuously power up more complex devices, like wireless sensor nodes or even a cell phone. On the basis of the quantitative relationship between the mechanical stimuli and the output signal of the nanogenerators, they could also be employed as self-powered active sensors for detection of external mechanical agitations, like pressure, motion, vibration, etc. The working of active sensors rely on the electrical output signals of nanogenerators, so external power supply on the device itself is not necessary, which greatly improve the convenience of its installation and application.

CHAPTER 2

IMPROVEMENT OF PIEZOELECTRIC NANOGENERATORS THROUGH ASSEMBLY OF NANOWIRES

2.1 Basics of piezoelectric nanogenerators

The development of PENG could be traced back to a few years ago. In 2006, Wang and Song[26] demonstrated the nanoscale mechanical energy conversion using ZnO NW array for the first time. In this work, the aligned NWs were deflected by a conductive atomic force microscope (AFM) tip at contact mode. The output voltage was recorded simultaneously when the AFM tip scanned over the top of the NW array (Figure 2.1a). The measured peak voltage was around 6~9 mV, and the mechanism of the NG was based on the coupling of the semiconductor and piezoelectric properties of the ZnO NWs. The Si-based AFM tip was coated with Pt and a Schottky barrier (SB) formed when the tip scanned over the NWs. The Schottky barrier served as a rectifying "gate" that led to the electrical generation. Control experiment was carried out to ensure the validity of this proposed mechanism.

Based on the basic mechanism of this work, people developed the experimental setup and improved the output performance step by step afterwards. In 2007, Wang *et al.*[27] developed a direct-current NG which was driven by ultrasonic waves. The nanogenerator was fabricated by vertically aligned ZnO NW array that was placed beneath a zigzag metal electrode with a gap (Figure 2.1b). The electrode was moving up and down driven by ultrasonic waves to bend the NWs. The generated output current could be up to around 1 nA. In 2008, Qin *et al.*[28] continued to fabricate a novel type of

NG that was based on the ZnO NWs grown around textile fibers (Figure 2.1c). The working mode was by entangling two fibers and brushing the NWs rooted on them with respect to each other. This work established a method for harvesting energy from light wind or body movement.

In 2009, Yang *et al.*[29] developed a NG based on a single ZnO NW that was transferred to a flexible Kapton substrate. The design and structure of NG is schematically shown in Figure 2.1d. This device was fully packaged with polydimethylsiloxane (PDMS) and showed excellent robustness and stability. Besides, the NG in this work showed an alternating current (AC) output, due to the different working mode compared to previous works. This work is the basis of the high output NGs based on the rational assembly of ZnO NWs later on.

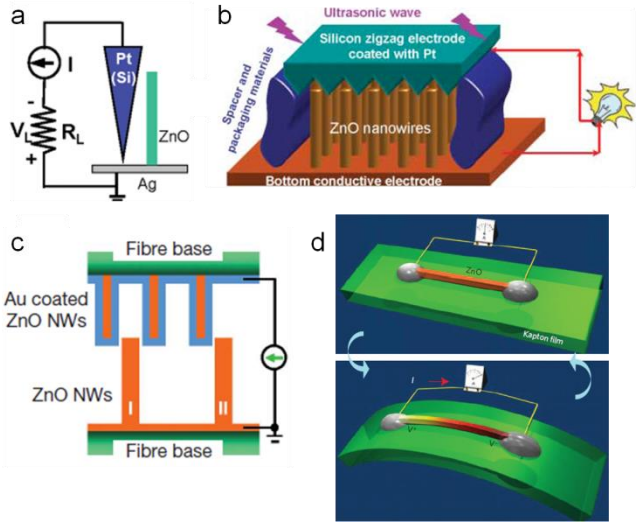

Figure 2.1 Schematic structures of the piezoelectric nanogenerators based on a single ZnO nanowire.[26-28]

Since 2010, more attention has focused on developing the high output nanogenerators based on rational integration of the ZnO nanowires. In this regard,

researchers utilized variable approaches for the integration or assembling of NWs on a flexible substrate (e.g. polyimide thin film) to obtain a stand-alone device for energy harvesting and its niche applications. Zhu *et al.*[30] employed the contact printing to transfer the as-grown vertically-aligned nanowires from the silicon substrate onto flexible Kapton substrate, and photolithography was followed to deposit stripped electrode array on the nanowires to electrically connect the NWs together in series and in parallel (Figure 2.2a). In this way, the open-circuit voltage will add up by the serial integration and the short-circuit current will add up by the parallel integration of the NWs. Based on this design and fabrication strategy, a high output voltage of ~2 V and output current of ~ 100 nA could be achieved (Figure 2.2d-e). By combining the nanogenerator with an energy storage system consisting of a capacitor and a full-bridge rectifying circuit, the harvested energy could be stored into the capacitor and was able to drive small electronics like light-emitting diodes. In the same year, Xu *et al.*[31] also developed the high output nanogenerator based on horizontally aligned ZnO NWs (Figure 2.2b), by growing ZnO nanowires directly on the pre-patterned electrode arrays through the wet chemical approach. The laterally-integrated nanogenerator (LING) also shows a high output voltage of 1.2 V, while the output current was lower (~20 nA), which was limited by the mis-oriented nanowires and the inactive bonding between the nanowires and the gold electrodes. Hu *et al.*[32] also developed the composite structure multi-layered horizontal ZnO nanowires with conical shape structure, which was infiltrated by PMMA insulating layer (Figure 2.2c). A high output voltage could also be achieved to directly power up small electronics like a liquid crystal display (LCD).

Most recently, our group has developed the PENG based on vertically aligned ZnO nanowires, along with a spin-coated PMMA layer as an insulation layer and strain buffer layer. With such design, a high output of ~ 10 V and 0.6 μA was achieved, which enabled a self-powered data transmission system by integration the PENG with an energy storage unit (capacitor), a data transmitter and a data receiver.[33]

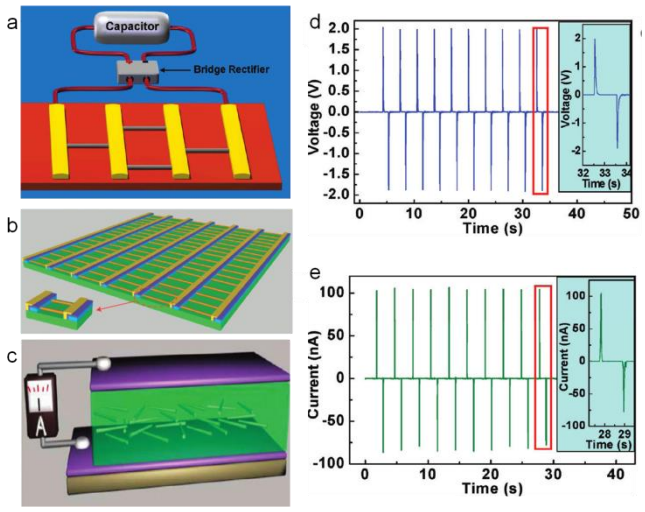

Figure 2.2 (a-c) Schematic illustrations showing the device structures of piezoelectric generators based on horizontal integration of the ZnO nanowires. (d-e) The typical output performance of the integrated nanogenerator.[30-32]

2.2 Transparent and flexible piezoelectric nanogenerator based on vertically-integrated ZnO nanowires

For practical applications of nanogenerators, the integration of transparency and flexibility characteristics is of great importance, especially for its potential applications in flexible electronics, artificial skins, and touch screens. In this regard, polydimethylsiloxane (PDMS) is an optically clear, bio-compatible, and fully rollable silicon elastomer, which is the core material for soft lithography to fabricate micro-fluidic

devices. It has been widely applied in the field of biological sensing, flexible solar cell, and tissue engineering. We also have previous investigation that utilized PDMS as a template for the growth of ZnO NW array. In this work, we successfully fabricated transparent and flexible NGs using ZnO nanowire (NW) array grown on PDMS substrate by wet chemical approach. The fully packaged NG showed good transparency, flexibility, and robustness.[34]

The device structure of the transparent flexible piezoelectric nanogenerator (TF-PENG) is schematically illustrated in Figure 2.3a. In the fabrication, the PDMS substrate was prepared by the gel-casting technique and the consecutive curing and peel-off process, through which a transparent and stretchable substrate with ideal thickness (~200 μm) was obtained. Closely packed ZnO NWs were uniformly grown on the PDMS substrate by the hydrothermal method, which is the effective component of the TF-PENG. The scanning electron microscopy (SEM) images of the NWs are shown in Figures 2.3b. The diameter of the NWs was ~ 500 nm and the length of the NWs was ~ 6 μm. It was observed that the NWs had a hexagonal cross-section, and were grown densely to form a textured film, which was similar with the results in our previous works. Then, polymethyl methacrylate (PMMA) was spin-coated on the NWs as an insulation/buffer layer. Finally, transparent ITO electrodes were deposited on the top and bottom surface of the composite structure. The effective size of the TF-PENG is 1.5 cm × 1 cm.

The working mechanism of the nanogenerator is based on the piezoelectric property of the ZnO textured film, according to our established model. When the flexible NG device is deformed by an external force, a piezoelectric potential (piezopotential) will

be introduced in the ZnO textured film. As a result, a potential difference will be generated across the top and bottom electrodes due to induced charges, and it will drive the electrons flowing in the external load until equilibrium. When the external force is released and the NG recovers to its original shape, the piezopotential vanishes and the accumulated electrons will flow back in the opposite direction. Thus, an alternating current output signal is expected from the electrical measurement.

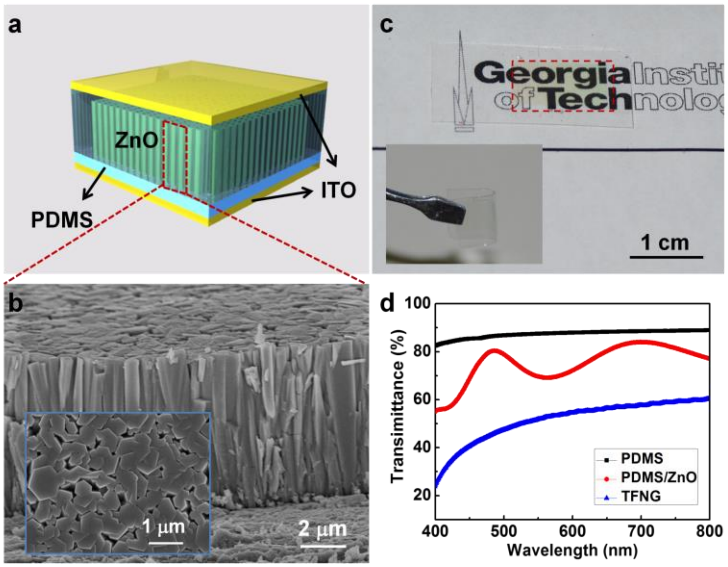

Figure 2.3 (a) A schematic of the device structure of the vertically-integrated piezoelectric nanogenerator (b) cross-sectional SEM image of the densely grown ZnO nanowires. (c) The photograph of the device showing its flexibility and transparency. (d) The transmittance measurement of the nanogenerator device.[34]

The as-fabricated TF-PENG showed good transparency and flexibility characteristics, which was revealed by the photograph of the TF-PENG in Figure 2.3c. The enclosed rectangular region indicated effective area of the TF-PENG, which was deposited with ITO electrode. The inset photograph indicated that the stretchable PDMS substrate could even be folded by the tweezers, without any obvious impairment to the structure of the device. Figure 2.3d showed the measured transmittance of the PDMS

substrate and TF-PENG device using ultraviolet-visible (UV-vis) spectrophotometer. It was observed that the transmittance of the PDMS film was over 80%, and that of the fully packaged device was around 50% to 60% in the visible range. The major limit of the transmittance was the scattering effect of the coated ITO electrode. The transmittance of the final device could be significantly enhanced if we used commercialized ITO electrode with better quality and higher transmittance.

To test the electrical output performance of the TF-PENG, we used a linear motor to apply a bending force to the device. Since the thickness of the PDMS substrate (~ 200 μm) was much larger than the length of the NWs (~ 6 μm), it could be estimated that the NWs only experienced compressive stress in the bending process, which is consistent with the condition in the numerical calculation. Figures 2.4a and 2.4b show the measured output performance of the NG device. With the strain of 0.12% at a strain rate of 3.56% s^{-1}, the open-circuit voltage and short-circuit current were measured to be 8 V and 0.6 μA, respectively, corresponding to a power density of ~5.3 mW/cm^3. This output is high enough for powering up small electronic devices, and it is also comparable to our previous results. Since the NG was extraordinarily flexible owing to the unique characteristic of the PDMS substrate, the whole device could serve as energy harvesting component in various working conditions, such as driven by wind blowing, body movement, or vehicle tire rotation.

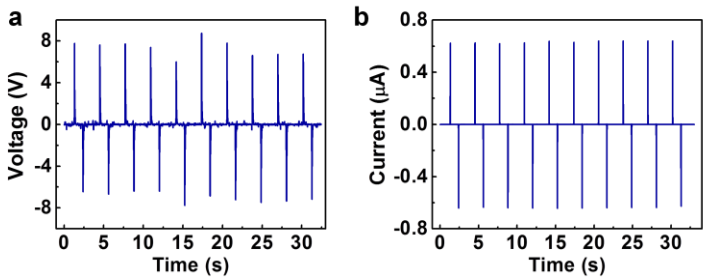

Figure 2.4 The typical output performance of the piezoelectric nanogenerator based on vertically-aligned ZnO nanowires.[34]

2.3 Performance enhancement of ZnO piezoelectric nanogenerator

Based on our former experimental and calculation results, the carrier density in ZnO nanowires (NWs) plays a key role on the output performance of the nanogenerator (NG).[35, 36] Our experimentally observed output voltage is much lower than the theoretically calculated piezopotential present in the material if doping occurs. This is because that the positive side of the piezopotential introduced by mechanical deformation will be partially screened by free electrons, which are the dominant charge carriers in n-type ZnO NWs. While the negative side of the piezoelectric potential preserves as long as the donor concentration is not too high, which is the case for the unintentionally doped, as-grown n-type ZnO. The calculation results show that the piezopotential at the positive side is reduced by almost a factor of 10 comparing to the negative side with a donor concentration of 10^{17} cm^{-3}. Thus we can expect that the strain-induced piezopotential can be remarkably enhanced as long as the carrier density in ZnO could be greatly depressed. According to this theoretical expectation, we have figured out several approaches to effectively enhance the output performance of the PENG, including plasma treatment, annealing, and surface passivation of the as-grown ZnO nanowires.[37]

There are always several monolayers of hydroxide (OH) due to H adsorption at the as-grown ZnO film surface, which introduce an electron accumulation layer at the surface.[38] And this phenomenon is also observed in the ZnO nanowire system. Oxygen plasma contains various oxygen ions and radicals such as O^+, O_2^+, and the main species O*. This oxygen radical atoms, O*, can combine with the surface adsorbed H atoms, and diffusion through ZnO bulk to fill oxygen vacancies, which are doubly charged electron donors for ZnO.[39, 40] Thus using oxygen plasma treatment can efficiently suppresses this surface accumulation layer and also the oxygen vacancies in ZnO, by which one order of magnitude reduction of carrier concentration has been obtained. In our investigation, after the ZnO NW arrays grown on the substrates, the device was treated with oxygen plasma for 30 minutes. Then the PMMA spin-coating on and electrodes deposition procedures were followed up as usual to finish the device fabrication.

Normally, ZnO NWs grown by hydrothermal method have a large defect concentration. But benefiting from the low growth temperature, it is still one of the best choices to accommodate flexible electronics. To improve the crystal quality, different post-growth methods have been investigated. One of them is annealing the ZnO NWs in different environments. Prior research showed that the oxygen-vacancy-related defects could be significantly reduced by annealing in air above 200 °C. Also the presence of the OH groups on the surface of the ZnO will be desorbed after annealing at temperatures of 150 °C and above. All of these facts indicate that we can anneal our device in atmosphere to reduce the carrier density and improve the output performance. In order to meet the requirement of high temperature annealing, we changed the NG's substrate from PS to polyimide film, which can resist a temperature as high as 400 °C. After the growth of

ZnO NW arrays on the Kapton film, the device was put in a furnace to be annealed at 350 °C for 30 minutes.

The third pre-treatment method we chose is the surface passivation of ZnO NWs with certain polymers. It is well known that metal oxides surfaces are rich in defects, predominantly oxygen vacancies, which are electron donors and also serving as the binding sites for chemical adsorption processes. Surface passivation can eliminate these defects and also make the surface to be more chemical inert, such as to be more resistive to H atom adsorption. Researches on ZnO NWs FET showed that the on-off ratio of the device can be greatly enhanced by reducing the off-states conductivity by surface passivation. In our experiment, the surface of the ZnO nanowire arrays were sequentially coated with positive charged poly (diallydimethylammonium chloride) (PDADMAC) and negative charged poly (sodium 4-styrenesulfonate) (PSS) through a layer-by-layer self-assembling method. Prior research has shown that this coating can reduce the dark current for the ZnO UV sensors.

Based on the above pre-treatment methods of the ZnO NWs, the measured output voltage reached 20 V, and the output current exceeded 6 μA. The corresponding power density is 0.2 W/cm^3 or 80 W/kg, which is 20 times larger than the previous best ZnO NW based NG. In addition to the elimination of the surface oxygen vacancies, this dramatic improvement of the output performance may come from the introduction of a depletion layer at the ZnO NWs' surface by further transfer electrons from NWs to the positive charged polymer PDADMAC. The actual mechanism of how these polymers worked with the ZnO surface is not fully understood yet. We have tested the NGs

passivated only with PDADMAC or PSS. There was no obviously performance improvement observed for such treatment.

2.4 Piezoelectric nanogenerator based on assembly of GaN nanowires

The concept of piezoelectric nanogenerator not only applies to ZnO nanowires (NWs), but can also be extended to other type of semiconductor nanomaterials, such as GaN,[41] CdS,[42] InN,[43] as demonstrated by measurement using atomic force microscopy. Owing to the large direct band gap, good thermal stability and high mobility, GaN has shown outstanding optoelectronic properties, and reveals great application potentials in a lot of fields. But it has been rarely used for NGs especially with high output performance. Here, by utilizing rational assembly of GaN nanowires, a high output GaN nanogenerator was demonstrated with an output voltage of 1.2 V. The working principle was further verified using finite element analysis.[44]

The growth of GaN NWs was based on a promotion of previously described vapor-liquid-solid (VLS) process. First, a 2 nm-thick Ni film was deposited on the (001) Si substrate by magnetron sputtering. This thin metal film served as a catalyst for the growth of GaN NWs. Then, the as-prepared substrate was placed in the middle of an alumina boat, while gallium metal was placed on both ends of the boat as a Ga source. The placement of Ga metal on both ends could effectively prevent oxidation of the product. Finally, the whole boat was put in the middle of a horizontal tube furnace and was evacuated to a pressure below 8×10^{-3} torr to remove oxygen and moisture. With an ammonia gas flow of 30 sccm (standard cubic centimeters per minute), the furnace was heated to 900 ˚C and then kept at for 30 minutes. The GaN NWs were formed due to the

chemical reaction at high temperature between Ga metal and NH_3. Compared to the previous work using sapphire substrate and metal-organic chemical vapor deposition (MOCVD) for depositing GaN thin film, this method was significantly more cost effective. An SEM image of the as-synthesized GaN NWs is shown in Figure 2.5a. It can be observed that the length of the NWs ranges from 10 to 20 μm, and the diameter varies from 100 to 500 nm. From the inset high magnification image, it was shown that the cross section of the NWs is a triangle. The aspect ratio of the NWs may vary due to different parameters in the growth process, such as temperature, flow rate of carrier gas, and relative position of the substrate in the tube furnace. Figure 2.5b shows the EDS analysis of the NWs, which indicates the main composition of the NWs is GaN, and the copper signal would most probably come from the background of the copper grid. Based on the TEM image in Figure 2.5c and the inset diffraction pattern, the growth orientation of the NW is $<10\bar{1}0>$. This orientation is perpendicular to the c axis of the NWs, which is consistent with a previous study of GaN NWs. The high resolution TEM image of the GaN NWs is shown in Figure 2.5d. The planar distance of the crystal planes which are perpendicular to the direction of the NW is measured to be 0.273 nm, which further confirmed that the orientation of the NWs is along $<10\bar{1}0>$ direction.

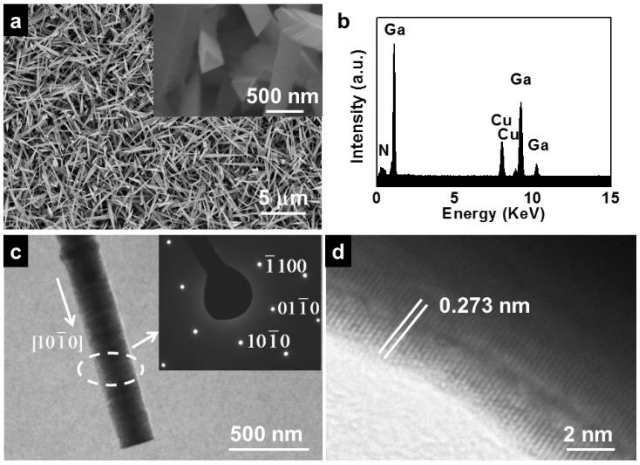

Figure 2.5 Crystal Structure and composition of the as-synthesized GaN NWs. (a) Top-view SEM image of the GaN NWs. The inset is a high-magnification SEM image showing the triangular cross-section of the NW. (b) EDS analysis of the GaN NWs. (c) High magnification TEM image of a single GaN NW, the inset is the corresponding selected-area diffraction pattern. (d) High-resolution TEM image of a single GaN NW.[44]

NGs were fabricated using the GaN NWs employing an approach previously demonstrated for conical shaped ZnO NWs. As shown in Figure 2.6, the GaN NG was composed of a multi-layer of NWs infiltrated with polymethyl methacrylate (PMMA), which was sandwiched by two metal electrodes of Cr/Au. In the first step, the Cr/Au electrode was deposited on a Kapton film by electron beam evaporation. Then, a layer of PMMA was deposited on this electrode by spin-coating. In the next step, the GaN NWs were suspended in ethanol by an ultrasonic wave and then dispersed on the substrate. Another thinner layer of PMMA was spin-coated after the ethanol evaporated from the substrate. After five cycles of GaN NWs and PMMA alternating deposition, another thicker layer of PMMA was spin-coated on. And finally, the top electrode of Cr/Au was deposited on the composite structure to serve as the top electrode. The effective size of the NG was 5 mm $\times$ 5 mm. For the measurement of electrical output, the as-fabricated GaN NG was attached to a flexible polystyrene (PS) substrate and then an external force was applied to bend the PS substrate by a linear motor. For simplicity, it was assumed that the NWs only experienced compressive strain due to a much larger thickness of the PS substrate relative to that of the assembled NG. The triangular cross section, the crystal structure and the orientation of the NWs play very important roles in the NG's high output performance. A piezoelectric polarization across the top and bottom electrodes was produced when the NG was bent. The potential difference will drive the electrons

flowing in the external circuit, from the bottom electrode to the top electrode. When the applied force is withdrawn, the strain in the NWs as well as the potential difference between the two electrodes disappears. The accumulated electrons at the top electrode will flow back, and thus an AC output signal is produced. This working mechanism is similar to that of our previously demonstrated ZnO NG, while the major difference is that the overall component of the c axis across the thickness of the NG results from the triangular cross section of the NW, rather than the conical shape of the NW in the ZnO NG.

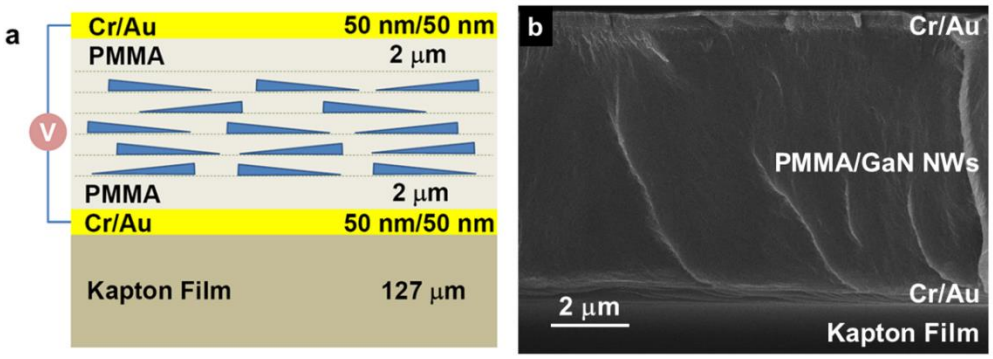

Figure 2.6 (a) Schematic illustration of the structure of the GaN NG. (b) Cross-sectional SEM image showing the composite structure of the GaN NG.[44]

The typical electrical output of the assembled NG is shown in Figure 2.7 a and b. The measured output voltage and the output current could be up to 1.2 V and 40 nA, respectively. The corresponding output current density was 0.16 $\mu A/cm^2$. For verification purposes, we also measured the output of the NG with a reverse connection to the external measuring circuit. It can be seen in Figure 2.7c and d that the sign of the output signal of the reverse connected NG was just opposite to that of the forward connected one. Thus it was confirmed that most of the measured signal came from NGs rather than from environmental noise. To further confirm the validity of measurement and exclude

the possible effect of environmental noise or systematic errors, we conducted a control experiment comparing the electrical output of the NG devices without the GaN NWs to that of the normal NG devices. As could be observed in Figure 2.8a and b, the output voltage and output current of the devices without the GaN NWs were two orders and three orders of magnitude lower than those of the devices with the GaN NWs, respectively. Therefore, it was ensured that possible noises in this measurement system could be neglected.

Though the performance of the GaN NG was not higher than that of the previously demonstrated ZnO NG with similar structure, it was still more promising in some specific cases. First, an ultimate goal for our NG projects was to develop self-powered nano-systems. GaN was widely used for optoelectronic devices such as light-emitting diode and quantum well lasers. The GaN-based NG had potential applications for fabricating hybrid devices which could harvest energy from the environment and drive functional parts of the devices. Second, defects such as oxygen vacancies were inevitable during the synthesis of ZnO NWs, which was a major drawback of the ZnO NG due to the screening effect from high carrier density, while the unintentionally doped GaN NWs were relatively free of such defects, and thus much higher performance could be anticipated if advanced technique such as MOCVD or molecular beam epitaxy (MBE) was employed to grow the GaN NWs with higher qualities.

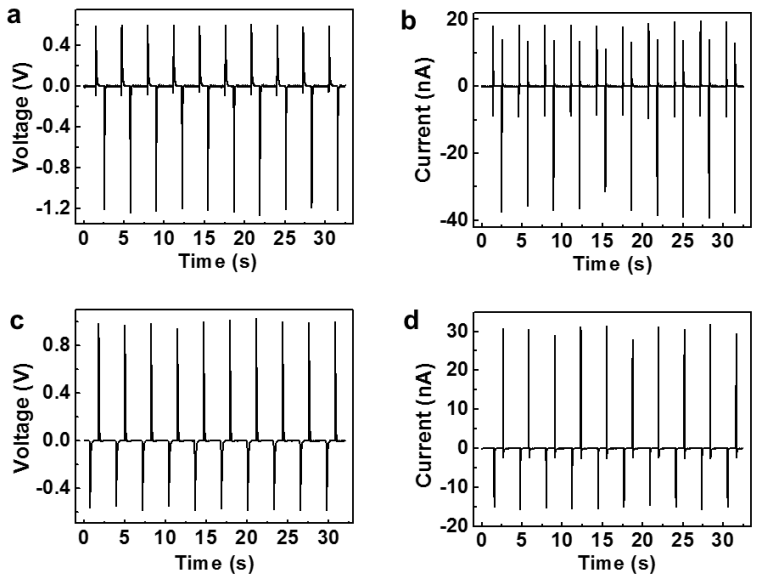

Figure 2.7 (a) Output voltage of the NG with forward connection. (b) Output current of the NG with forward connection. (c) Output voltage of the NG with reverse connection. (d) Output current of the NG with reverse connection.[44]

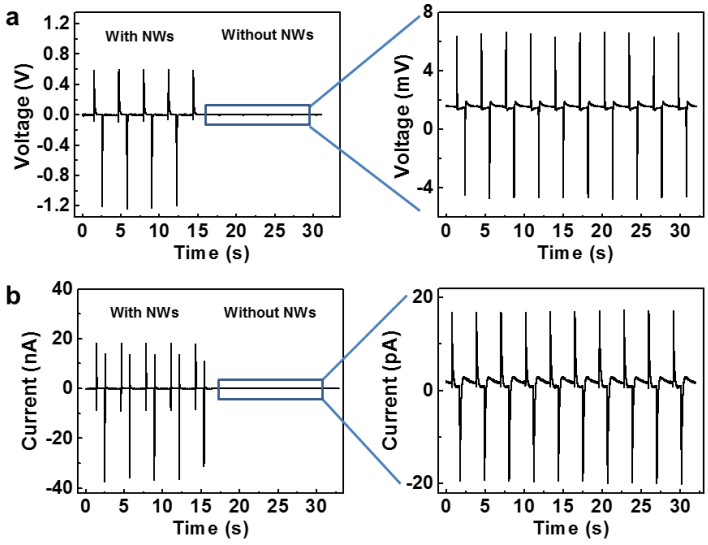

Figure 2.8 Comparison of electrical measurement between normal NG devices and the devices without the GaN NWs. (a) Comparison of output voltage between normal NG devices and the devices without the GaN NWs. The right image is the output voltage of devices without GaN NWs at high magnification. (b) Comparison of output current between normal NG devices and the devices without the GaN NWs. The right image is the output current of devices without GaN NWs at high magnification.[44]

To understand the mechanism of harvesting energy with this structure, we calculated the potential across the thickness of the NG structure with a simple model using finite element analysis (FEA), as shown in Figure 2.9a and b. The three side surfaces of the GaN NW were $(000\bar{1})$, $(1\bar{2}11)$, and $(\bar{1}2\bar{1}1)$. The NG structure is a "capacitor like" plate structure in which the GaN NWs and PMMA serve as a composite "dielectric media". Since the cross section of the NW is an isosceles triangle, we assume that each of its three side surfaces has an equal possibility to lie flat on the substrate. Based on this assumption, three NWs with different orientations were placed in a unit cell. The whole structure was considered as a cantilever with its one end being fixed and a periodic force of 40 MPa being applied at the top edge of the other end. Lipmann theory was used to calculate the piezopotential introduced inside the NW. For simplicity of the simulation, the NWs were taken to have a uniform size of 19.5 μm in length. The dimension of the unit cell for the simulation was 20 μm × 7.5 μm × 2 μm. In this case, the density of NWs in the unit cell was 20000 NWs/mm^2, which matches the density of NWs in the realized structure. The material constants of the GaN NW were taken as a = 0.3189 nm, c = 0.5185 nm, C_{11} =3 90 GPa, C_{12} = 145 GPa, $C1_3$ = 106 GPa, C_{33} = 398 GPa, C_{44} = 105 GPa, piezoelectric constants e_{15} = e_{31} = -0.49 C/m^2, e_{33} = 0.73 C/m^2, relative dielectric constants k_{11} = k_{22} = 9.28, k_{33} = 10.01, and the density of GaN 〉 = 6150 kg/m^3. For the purpose of simplicity, the NWs were assumed to be insulating. The calculation result is shown in Figure 2.9c. It is shown that the calculated potential across the thickness of this structure is 1.5 V. The measured output voltage of 1.2 V was consistent with this calculation result. The measured output voltage was a little lower

than the calculation result and this was probably due to the screening effect of the GaN NWs, since the GaN NWs were not ideally insulating.

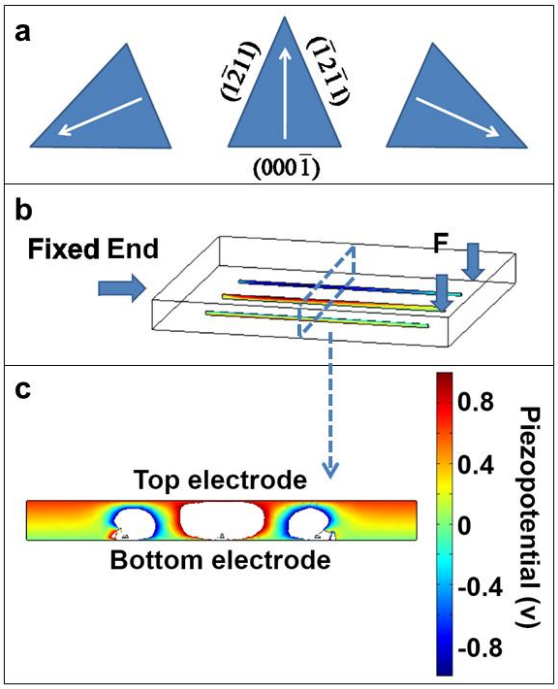

Figure 2.9 (a) Schematic of the cross section of the NWs with three possible orientations. The arrows show the direction of c axis in each NW. (b) Schematic model showing the setup for numerical calculation of the potential across the thickness of the NG. The entire structure is like a one-end (left-hand side) fixed beam, with a transverse force applied at the free end. (c) Taking a cross-section at the midpoint of the NWs, the calculated potential difference between the top and bottom electrodes of a NG is presented. The blank region close to the NWs indicates that the local potential is over the range of color display.[44]

In summary, we have successfully fabricated high output NGs using GaN NWs with triangular cross section. The GaN NW shows the orientation of $<10\bar{1}0>$ along the NW direction, with c axis perpendicular to the NW. The as-fabricated NG is a "capacitor-like" plate structure, in which GaN NWs and PMMA serve as "dielectric media". The output voltage and output current density could be up to 1.2 V and 0.16 μA/cm2, respectively. The calculated piezopotential is consistent with the measured output. This

study shows that GaN NWs can be a good candidate for fabricating high output NGs for driving small electric devices.

CHAPTER 3

PERFORMANCE ENHANCEMENT OF TRIBOELECTRIC NANOGENERATORS

3.1 Basics of triboelectric nanogenerators

Most recently, using the electrostatic charges created on the surfaces of two dissimilar materials when they are brought into physical contact, the contact induced triboelectric charges[45-47] can generate a potential drop when the two surfaces are separated by mechanical force, which can drive electrons to flow between the two electrodes built on the top and bottom surfaces of the two materials. This is the birth of the triboelectric nanogenerator (TENG).[48] Ever since the first report of the TENG in January 2012, the area power density reaches 500 W m^{-2},[49] volume power density reaches 15 MW m^{-3}, and an instantaneous conversion efficiency of ~ 70% has been demonstrated.[50] For low frequency agitation and if the energy generated by all the residual vibrations are acquired, a total energy conversion efficiency of up to 85% has been shown experimentally.[51] The TENG can be applied to harvest all kinds of mechanical energies that are available but wasted in our daily life, such as human motion,[52] walking,[53] vibration,[54-56] mechanical triggering,[57] rotating tire,[58-60] wind,[61-63] flowing water[64-66] and more. Alternatively, a TENG can also be used as a self-powered sensor for actively detecting the static and dynamic processes arising from mechanical agitation using the voltage and current output signals of the TENG, respectively, with potential applications as mechanical sensors and for touch pad and smart skin

technologies.[67-72] The TENG also has the potential of harvesting wave energy in ocean based on a new approach, which could be a new paradigm for large scale energy.[73-75]

Triboelectrification[76-79] is an effect that is known to each and every one probably ever since the ancient Greek time, but it is usually taken as a negative effect and is avoided in many technologies. Discharges caused by triboelectricity have many disaster damages to industrial processes, electronics, human life and nature, such as wild fire. But this effect exists almost everywhere in our life and for any materials we use each day, so that it is not limited to any specific materials. Our goal here is to use triboelectricity for converting mechanical energy into electricity based on new materials and new designs. As for TENG, in the open-circuit condition, a potential difference between two electrodes attached on the back sides of the films is created by the coupling of triboelectrification and electrostatic induction. The triboelectric charges are generated due to the charge transfer between two thin organic/inorganic films that exhibit distinct surface electron affinity, and the potential difference results from the separation of the triboelectric charges; in the short-circuit condition, electrons are driven to flow between two electrodes attached on the back sides of the films through the load to balance the potential difference resulted from mechanical action. Here we first introduce the four fundamental modes of the TENG (Figure 3.1), which are the basics for various prototypes of the TENGs.[80]

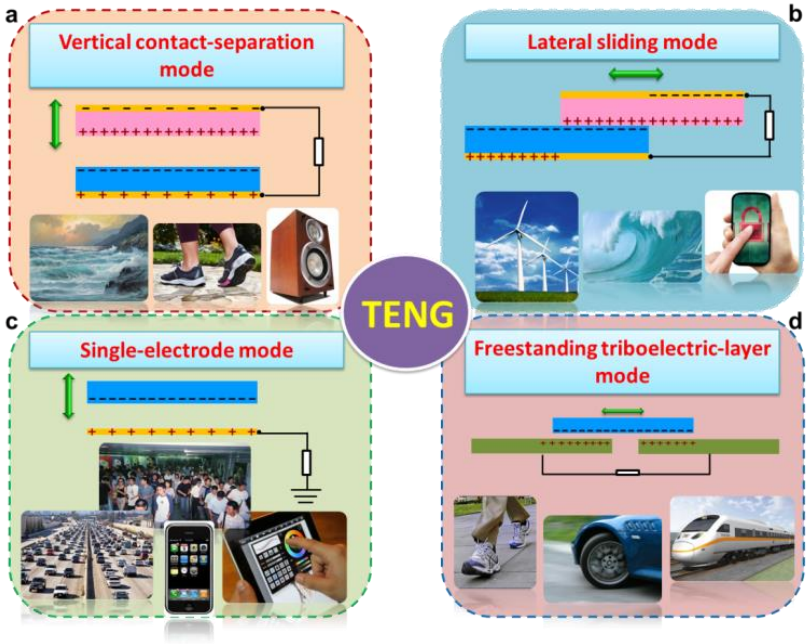

Figure 3.1 The four fundamental working modes of the triboelectric nanogenerators. (a) The vertical contact-separation mode. (b) The lateral sliding mode. (c) The single-electrode mode. (d) The free-standing mode.[80]

The vertical contact-separation mode was the first invented operation mode for the TENGs. A physical contact between the two dielectric films with distinct electron affinity (at least one is insulative) creates oppositely charged surfaces. Once the two surfaces are separated by a gap, a potential drop is created between electrodes deposited on the top and the bottom surfaces of two dielectric films, as demonstrated in Figure 3.1a. If the two electrodes are electrically connected by a load, free electrons in one electrode would flow to the other electrode in order to balance the electrostatic field. Once the gap is closed, the potential drop created by the triboelectric charges disappears, the induced electrons will flow back. A periodic contact and separation between the two materials drives the induced electrons to flow back and forth between the two electrodes, resulting in an AC output in the external circuit.

As shown in Figure 3.1b, when two materials with opposite triboelectric polarities, for instance, PTFE and aluminum, are brought into contact, surface charge transfer takes place due to the triboelectrification effect. Since PTFE holds a higher electron affinity than aluminum, electrons are injected from aluminum into PTFE. When the PTFE and Al are fully aligned, the electric field created by the triboelectric charges does not produce a potential drop, because the positive charges on aluminum are fully compensated by the negative ones on PTFE. Once a relative displacement is introduced by an externally applied force in the direction parallel to the interface, triboelectric charges are not fully compensated at the displaced/mismatched areas, resulting in the creation of an effective dipole polarization in parallel to the direction of the displacement. Therefore, a potential difference across the two electrodes is generated. A sliding back and forth between the two will result in a periodical change of the electric potential difference, which will drive free electrons to flow alternatively across the electrodes. The in-plane sliding mode holds several important advantages compared to the vertical contact-separation mode. The generation of triboelectric charges from the relative sliding between two surfaces is much more effective than the pure contact, which contributes to a greatly enhanced output power for practical applications. And furthermore, the in-plane sliding mode is easy to develop more advanced design for high-performance TENGs. For instance, through a grating structure, the total transported charge is greatly enhanced. With constant sliding velocity, finer grating shortens the time to transport induced charges between the electrodes, which enables substantial enhancements of both the magnitude and frequency of the output current.

For both the vertical contact-separation mode and in-plane sliding mode triboelectric nanogenerators, the moving objects need to be bonded with an electrode and a lead wire. Such a device configuration largely limits TENGs' versatility and applicability for harvesting energy from an arbitrary, freely moving object, because the object has to be connected to the entire system by an interconnect. A single electrode mode TENG was developed to solve this problem. As demonstrated in Figure 3.1c, which consists of, for instance, a PTFE moving object and an aluminum layer electrically connected to the ground. In the original position, PTFE and aluminum are fully in contact with each other, which will result in that electrons are injected from aluminum to PTFE since PTFE has higher surface electron affinity than aluminum. Once the negatively charged PTFE slides apart or separates, a decrease of the induced positive charges on the Al occurs, and the electrons will flow from ground to aluminum till the two plates are entirely separated, in order to balance the electric potential. Then, when the PTFE slides backward or comes to contact again, the induced positive charges on the aluminum increase, driving the electrons to flow from aluminum to the ground till the two plates fully overlapped to re-establish an electrostatic equilibrium. This is a full cycle of electricity generation process of the single-electrode mode TENG. In the single electrode mode, although the induced electrons transfer across the electrode is not the best effectiveness due to the electrostatic screening effect, one of the triboelectric layers can move freely without any restriction.

The freestanding triboelectric-layer mode triboelectric nanogenerator is also capable of scavenging energy from the mechanical motion without an attached electrode, as shown in Figure 3.1d. If we make a pair of symmetric electrodes underneath a

dielectric layer and the size of the electrodes are of the same order as the size of the moving object, and there is a small gap between the object and the electrode, the object's approaching to and/or departing from the electrodes create an asymmetric charge distribution via induction in the media, provided the object was prior-charged by a triboelectric process, which causes the electrons to flow between the two electrodes to balance the local potential distribution. The oscillation of the electrons between the paired electrodes in responding to the back and forth motion of the object produces an AC current output. Compared to the single-electrode mode, there is no screening effect in this mode, and the electrostatically-induced electron transfer can reach the same amount of the triboelectric charges on the free-standing layer. In this working mode, there is no direct physical contact between the two triboelectric layers, compared to the in-plane sliding mode, it will cause no material abrasion and heat generation under long-term continuous working. This distinguishes the free-standing mode with ultra-robustness as well as high energy conversion efficiency.

3.2 Transparent triboelectric nanogenerators based on micro-patterned plastic films

In this work, instead of using the relatively flat polymer sheets, we have fabricated some patterns on the polymer surfaces to increase the triboelectric power output.[70] To make patterned polydimethylsiloxane (PDMS) films, Si wafer molds were firstly fabricated by traditional photolithography method, followed by dry or wet etching process to fabricate different recessed features including lines, cubes, and pyramids. The surface of the molds was initially treated with trimethylchlorosilane to prevent the PDMS film from sticking to the master. The liquid PDMS elastomer and cross-linker were

mixed, degassed and uniformly spin-coated on the surface of the master. After curing thermally, a uniform PDMS layer was peeled off and contained the inverse of the original pattern features on the surface of the mold. Finally, the PDMS film was fixed on the insulation surface of a clean indium tin oxide (ITO)-coated polyethylene terephthalate (PET) substrate by a thin PDMS bonding layer, and then the entire structure was covered with another ITO-coated PET film to form a sandwich-structured device. A detailed fabrication protocol and typical structure of a flexible transparent nanogenerator (FTNG) is schematically shown in Figure 3.2. One significant advantage of this technique is that hundreds of replicas of patterned PDMS films can be produced from one single mold. Silicon-based molds can be replaced by metal molds (Ni or Al) due to their excellent mechanical properties and longevity. The entire preparation process of the device is simple and low-cost, making it possible to be scaled-up for large-scale production and practical applications.

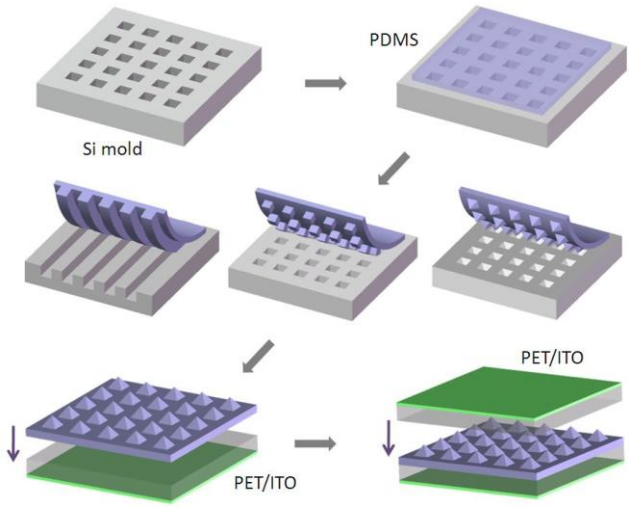

Figure 3.2 Schematic illustration of the fabrication process of the FTNG and the pressure sensor devices.[70]

Optical and scanning electron microscopy (SEM) analysis of the resulting PDMS pattern arrays show that the above-mentioned fabrication protocol yields regular and uniform microstructures across the whole area of a 4-inch wafer mold (Figure 3.3). The shape and lateral dimensions of the polymer structure are well controlled by the initial patterns on the surface of the wafer mold. Here, we fabricated three kinds of PDMS pattern arrays, including lines, cubes, and pyramids. As shown in Figure 3.3a-c, the size of single PDMS features is limited to about 10 μm. Smaller features down to 5 μm were also produced with consistent quality. High magnification SEM images illustrate that all of the features are regular and remarkably uniform, demonstrating that this procedure is an efficient method in preparing large-scale uniform plastic microstructures. Importantly, each pyramid feature has a perfect geometric structure and a sharp tip, which is beneficial for increasing the friction area and the efficiency in the power generation process of the FTNG. In addition, the prepared PDMS film is stretchable and transparent, as illustrated in Figure 3.3d.

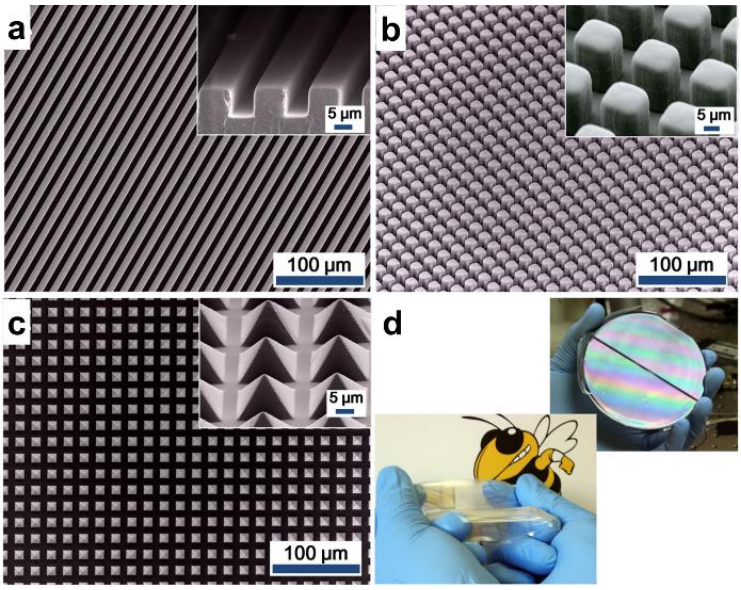

Figure 3.3 Structure characterization of the patterned PDMS thin film. (a) SEM image of the patterned PDMS thin film with line features. The inset is a 75˚-tilted high

magnification image showing the size and cross section structure of the features. (b) SEM image of the patterned PDMS thin film with cubic features. The inset is a 45˚-tilted high magnification image showing the height of the cubes. (c) SEM image of the patterned PDMS thin film with pyramids features. The inset is a 45˚-tilted high magnification image showing the pyramid structure of the features. (d) Photographs showing the appearance of the as-fabricated PDMS thin film. Top-right: the photograph of as-fabricated PDMS thin film on the Si mold. The interference fringes on the surface of the PDMS film indicate the uniform patterned features at large scale. Bottom-left: the peeled-off PDMS thin film showing its flexibility and transparency.[70]

To investigate the electrical output performance of the polymer FTNG, we made a detailed comparative characterization of the devices with different PDMS features. Figure 3.4a-b shows the open-circuit voltage and short-circuit current output of the typical FTNGs with four different PDMS feature types: film (unstructured plane), line, cube and pyramid. The result clearly shows that the order of the output efficiency of different FTNGs follows film < line < cube < pyramid. When we used a linear motor in a cyclic agitation to periodically bend and release FTNG (at a frequency of 0.33 Hz and with a strain of 0.13%), the maximum output voltage and current signal for pyramid-featured devices are up to 18 V and 0.7 μA (corresponding to a current density of 0.13 $\mu A/cm^2$), respectively, which are almost four times as high as the previously reported TEG using flat films and can also compare favorably with that received based on piezoelectric materials and complex designs. The dramatic increase in the electrical output of the structured films over the unstructured films can be attributed to two main factors: (1) the triboelectric effect of the microstructured films far surpassed that exhibited by the unstructured films with similar thickness. A regular rougher surface has a larger contact area and can generate more surface charges during the friction. (2) The capacitance in the structured films is significantly improved due to the presence of the air

voids and the increase in effective dielectric constant. It has also been demonstrated that a completely sealed device with few air voids/bubbles and weak sliding shows a rather low output due to the weak friction. Therefore, the PDMS films with pyramid or cube structures in particular give almost 5-6 times improvement in the power generation compared with that in the unstructured films. It should be noted that when the size of the features is reduced to 5 μm from 10 μm, the output voltage of the generator has no obvious improvement. The possible reason is that the total contact area didn't increase significantly according to our patterned design and the smaller features were more susceptible to defects as a result of imperfections in the Si mold.

The detailed power generation mechanism of the triboelectric generator has been illustrated in our previous report. Generally, a dipole layer induces an inner potential layer in a bending or releasing process, which will drive the free electrons to flow across the external load to countervail the impact of the inner potential change (Figures 3.4c). The current *I* generated across an external load can be defined as follows,

$$I = C\frac{\partial V}{\partial t} + V\frac{\partial C}{\partial t} \tag{3.1}$$

where *C* denotes the capacitance of the system and *V* is the voltage across the two electrodes. The first term is the variation in the potential across the top and bottom electrodes owing to the electrostatic induced charges. The second term is the change in the capacitance of the system as the distance between the top and bottom electrode is changed due to the mechanical deformation of the unit. Therefore, the power generation performance of the FTNG is closely related to the capacitance change of the system. Hence, through rational design, we have significantly improved its ability in the power generation utilizing polymer patterned arrays to increase the triboelectric effect and the

capacitance change. Here, PDMS film plays an important role and benefits the performance in two aspects: (1) it is a soft, transparent material, and could easily be fabricated into a patterned array with various features, (2) the location of PDMS in the triboelectric series is far away from that of PET, which is critical for achieving a higher performance. Furthermore, since the entire structure is based on polymer materials, the FTNG exhibits excellent mechanical robustness and stability, and it can still work properly after being tested for ~105 cycles (Figure 3.4d).

The goal of our design is to integrate flexible, high-output and transparent properties into a single nanogenerator. To achieve the purpose of transparent devices, we therefore assembled the entire device with only two transparent polymer materials (PET and PDMS) and a transparent electrode material (ITO). To systematically characterize the transparency of FTNG components and the full devices with different PDMS patterns, UV-vis spectroscopy is used to study the transmittance of the devices, as shown in Figure 3.4e. The commercial ITO-coated PET film showed a transmittance of 85% in the visible and near infrared region. After coated with a layer of unstructured PDMS film, the transmittance is almost unchanged. A full film-featured nanogenerator exhibits a high transmittance of ~75%. Since the microstructures have a strong light scattering effect, the other three full FTNGs with different PDMS features show a lower transmittance (approximately 50%). Figure 3.4f shows the photograph of a FTNG adhered on the screen of a smart phone, which indicates the high transparency of the FTNG and its potential application in touchscreen, high-definition LCD, and other self-powered electronic displays.

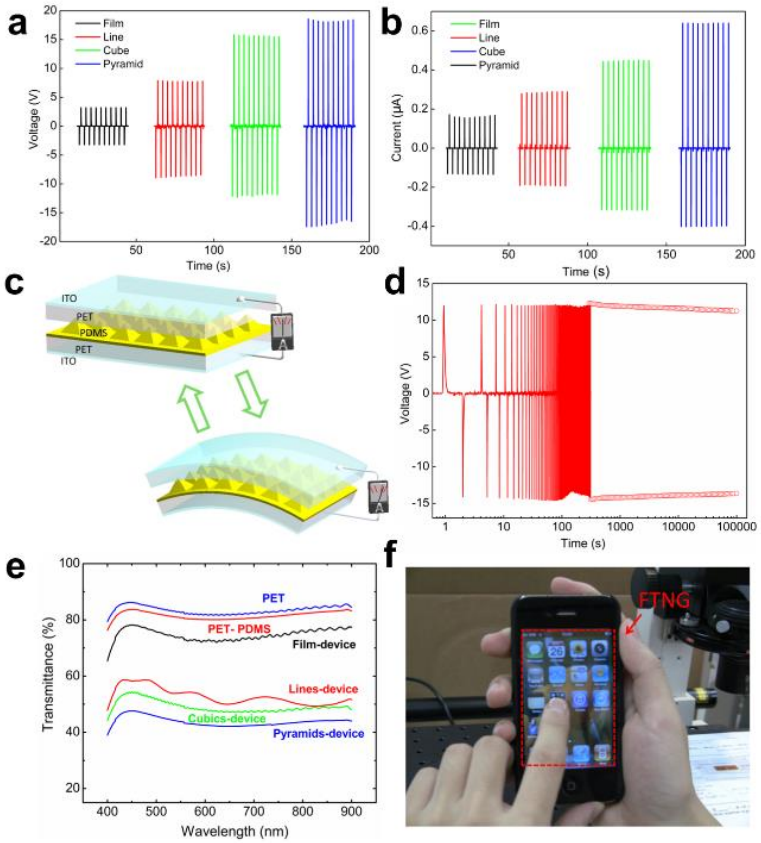

Figure 3.4 Electrical output and optical measurement of the FTNG. (a) Output voltage of the FTNG using PDMS thin film with flat surface and various patterned features, respectively. (b) Output current of the FTNG using PDMS thin film with flat surface and various patterned features, respectively. (c) Schematic illustration of the charge-generating process of the triboelectric generator. Pushed by the bending force from the linear motor, the device will be switching back and forth between the normal state (top-left) and the bending state (bottom-right), and there will be an alternating flow of electrons in the external circuit driven by the induced triboelectric potential. (d) Stability test for the FTNG. (e) The UV-vis spectra of various types of substrates and FTNG devices. (f) The photograph of a FTNG device attached on the screen of a smart phone which indicates the high transparency of the NG device.[70]

In summary, we have demonstrated a new flexible transparent nanogenerator based on the triboelectric process and it can be used as a self-powered high-sensitive pressure sensor. Three types of regular and uniform PDMS patterned arrays at the micrometer scale are achieved through a common and scalable approach. This novel

design can significantly improve the output efficiency of the nanogenerator by increasing the triboelectric effect and the capacitance change. For a typical FTNG with pyramid-featured PDMS pattern, the electrical output achieved a peak voltage of 18 V and current of 0.7 μA with a peak current density of ~0.13 $\mu A/cm^2$, which is four times as high as that of the previously reported triboelectric generator. As the entire structure of FTNG was fabricated by transparent polymer materials and electrode, the film-featured devices show transparency of ~75%, resulting in a transparent flexible nanogenerator. Further, owing to the simple and low-cost production process, the FTNG exhibits great advantages in industrial production and practical applications as well as manufacturability, durability and capability of integration with other processing technologies. Finally, the FTNG shows its potential application in self-powered systems for touchscreens, electronic displays, and even personal electronics.

3.3 Arch-shaped contact-mode triboelectric nanogenerators

A rapid expansion of electronic devices towards wireless, portability, and multi-function desperately needs the development of independent and maintenance-free power sources. The emerging technologies for mechanical energy harvesting are effective and promising approaches for building self-powered systems, because of a great abundance of mechanical energy existing in our living environment and human body. Since 2006, piezoelectric nanogenerators (PNGs) have been developed to efficiently convert tiny-scale mechanical energy into electricity. Recently, another creative invention is the cost-effective and robust triboelectric nanogenerators (TENGs) based on the universally known contact-electrification effect. TENG harvests mechanical energy through a

periodic contact and separation of two polymer plates. However, in order to realize sustainable driving of electronic devices/systems, the output of TENG must be significantly improved through a rational design.

The two different types of nanogenerators presented above have a similar underlying physical process for producing electricity: generation of immobile charges (ionic charges for PNG or electrostatic charges on insulators for TENG), and a periodic separation and contact of the oppositely charged surfaces to change the induced potential across the electrodes, which will drive the flow of free electrons through an external load. The electrical output and efficiency is radically determined by the effectiveness of the above two processes. As for the charge generation in TENG, maximizing the generation of electrostatic charges on opposite sides is critical, which can be achieved by selecting the materials with the largest difference in the ability to attract electrons and the modification of surface morphology. In another aspect, the effective periodic switching between separation and intimate contact of the two charged plates is vitally important to determine the electrostatic potential across the two electrodes, which is the driving force for the free electrons. For the plate-structured TENG, it is not easy to achieve both complete contact and separation of the two oppositely charged plates upon pressing and releasing, especially under the electrostatic attraction between them. A firmly attached contact of the two oppositely charged surfaces is unfavorable for electricity generation. If we simply use a spacer between the two plates, it will then hinder the complete contact of the two plates. In this paper, we completely solved this problem through an arch-shaped TENG with a steady gap between the plates at strain-free conditions. This was achieved through ingeniously introducing surface thermal stress during thin film deposition. Based

on this unique structure, the voltage and current reached 230 V and 0.13 mA with an instantaneous maximum power density of 3.56 mW/cm^2 and 128 mW/cm^3 (note the latter was calculated using the entire volume of the device here and afterward unless specified). The power of a single device is high enough to continuously drive a LED. With the first realization of charging a lithium ion battery (LIB) to full capacity, the TENGs were combined with LIBs to form power modules for driving a wireless sensor system and a commercial cell phone. This is an unprecedented progress in rational optimization of the TENG design and its first application for self-powered systems, unambiguously demonstrating its feasibility for powering portable electronics, sensors for health care, environmental and infrastructure monitoring and security.

The arch-shaped TENG[81] is based on the contact electrification between patterned polydimethylsiloxane (PDMS) as the top plate and patterned Al foil as the bottom plate (Figure 3.5a). According to the triboelectric series, the purposely-chosen PDMS and Al are almost at the two ends with very large difference in ability to attract and retain electrons. The unique arch-shaped structure of the TENG from the naturally-bent top plate, which helps to carry out the action of effective charge separation and contact using the elasticity of the film, is achieved by the following innovative fabrication process (Figure 3.5b-c): The top part starts from a piece of flat Kapton film (Figure 3.5b<i>). A layer of 500-nm SiO_2 film is deposited using plasma-enhanced chemical vapor deposition (PECVD) at 250 °C (Figure 3.5b<ii>). Upon cooling down to room temperature, the Kapton will shrink to a much larger extent than the SiO_2 film because of the large difference in thermal expansion coefficients, so that thermal stress across the interface will make the plate bent naturally towards the SiO_2 side. Then, the pre-fabricated PDMS

film with pyramid patterns is glued to the inner surface through a thin PDMS bonding layer (Figure 3.5b<iii>). Finally, the electrode is deposited on top (Figure 3.5b<iv>). As for the bottom plate, an aluminum foil (Figure 3.5c<i>) is patterned with a typical photolithography process: defining the photoresist to the array of square windows (Figure 3.5c<ii>); depositing a layer of aluminum on top (Figure 3.5c<iii>), and finally lift-off, leaving the patterned Al cubes on the foil (Figure 3.5c<iv>). At last, the two as-fabricated plates of the same size are attached face to face and sealed at the two ends. The soft Al plate will be forced to bend outward under the contraction from the other plate, so that a gap will form naturally in between. The patterned surfaces of PDMS film (Figure 3.5d) and Al foil (Figure 3.5e) are fabricated to enhance the triboelectric charging and are characterized using scanning electron microscopy (SEM). Both the arrays are uniform and regular across a very large area.

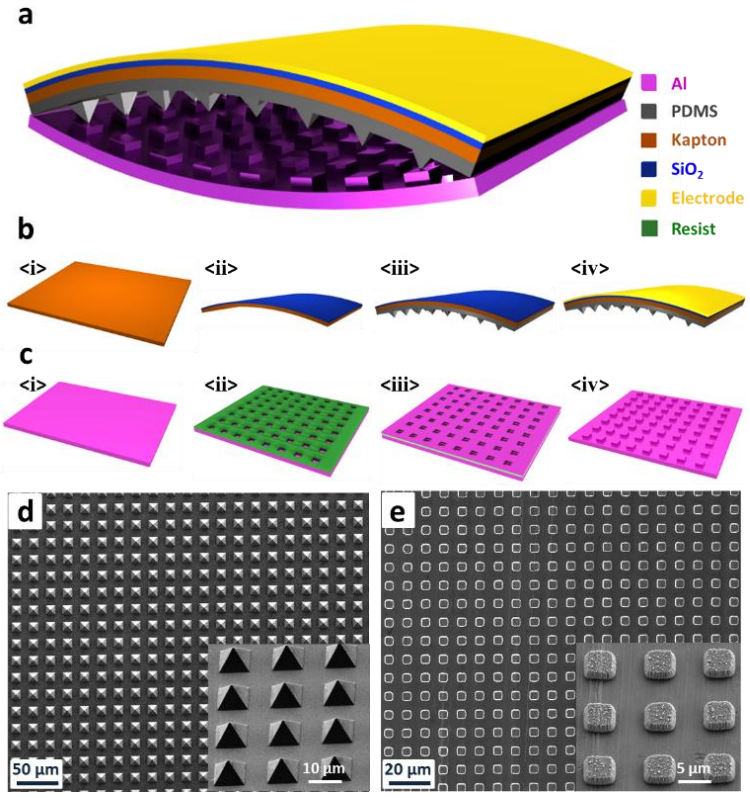

Figure 3.5 Structure and fabrication process of the arch-shaped triboelectric nanogenerator (TENG). (a) Schematic diagram showing the structural design of the arch-shaped TENG, the inset is the photograph of a typical arch-shaped TENG device. (b, c) The fabrication flow chart for (b) the top plate and (c) bottom plate of the TENG. (d, e) Top view SEM images of (d) the PDMS surface with pyramids patterns and (e) Al surface with cubic patterns, the insets are high-magnification images in tilted angle.[81]

The operation of the arch-shaped TENG is realized by applying a cycled compressive force onto the whole area of the device, so that the bending plates will be periodically pressed to flatten and contact closely with each other. Once released, the two plates will separate apart due to the stored elastic energy and revert instantaneously back to their original arch shape due to resilience. The working principle of the polymer-metal TENG is schematically depicted in Figure 3.6 using the numerically simulated electrostatic potential distribution arising from triboelectric charges (using COMSOL package). These semi-quantitative results show that a cycled generation of the potential difference between the two electrodes drives the flow of electrons through an external load. At the original state before the contact of the triboelectric films (Figure 3.6a), there is no charge transferred, thus no electric potential. Upon the pressing of the two films towards each other, they will be brought into fully surface contact and possibly relative sliding would occur, which results in electrons transfer from a material in the positive side of the triboelectric series to the one in the negative side in the series. Accordingly, electrons will be injected from Al to PDMS surface, leaving positive charges on Al foil. Previous theoretical study on triboelectricity reveals that such charge transfer process will continue in the first few hundreds of cycles until the accumulated charges reach a saturation and equilibrium; the negative charges will preserve on the PDMS surface due to the nature of insulator. But the positive triboelectric charges on the conductive Al foil

would attract the electrons in the opposite electrode to flow through external load, which is the observed current in this case. This process is different from the mechanism proposed for the polymer-polymer based TENG. After cycles of deformation, when the device is pressed and the surfaces with charges are in close contact with each other, all of the triboelectric charges will stay on the inner surfaces with the same surface density (σ_0) (Figure 3.6b). Thus, these charges with opposite signs will be virtually in the same plane, and there will be little potential difference across the two layers due to the negligible charge separation. Once the pressing force is released, the TENG will immediately rebound back to its original arch shape due to the elasticity of the film so that a gap will form again between the two plates. From the numerical simulation result, if the charge transfer has not happened at the moment, the electric field generated by the separated surface charges will give rise to a much higher potential on the Al foil side than the top electrode (TE) (Figure 3.6c). Such a potential difference will drive the flow of positive charges from Al foil to TE through the external load until the potential difference is fully offset by the transferred charges, rendering the TE with a surface charge density of ($\Delta\sigma$), while the Al is left with ($\sigma_0 - \Delta\sigma$) (Figure 3.6d). Subsequently, when the TENG is pressed again to reach the close contact of the two plates, these redistributed charges will inversely build a positive potential on TE (Figure 3.6e), which will drive all of the transferred charges ($\Delta\sigma$) to flow back to the inner surface of the Al foil. Then a cycle is achieved and the device will go back to the equilibrium state depicted in Figure 3.6b. This is a full cycle of electricity generation.

From the above simulation result, we can easily tell that both the voltage and current outputs are related to the amount of charges transferred ($A\Delta\sigma$, A is surface area of

the plate), which is determined by the triboelectric charge density (σ_0) and the separation distance of the two plates. As σ_0 is regarded as a constant, we did an analytical calculation based on the simplified model of quasi-infinite flat plates, to give an idea on the magnitude of the distance required for the optimum output. The relationship of the ratio between $\Delta\sigma$ and σ_0, with the planar separation distance, is shown in Figure 3.6f. We can see that, when the separation distance starts to increase from 0 to 0.7 mm, $\Delta\sigma$ keeps a very rapid increase from 0 to ~ 90% of σ_0. Then, the slope of this curve starts to decrease. Thus, it can be concluded that both an intimate contact and a subsequent separation of nearly 1 mm are required for the phenomenal transferring of charges. This is just the unique innovation and advantage of the purposely designed arch-shaped structure, which introduces sufficient resilience for separating the plates but without sacrificing the intimate contact and electrification.

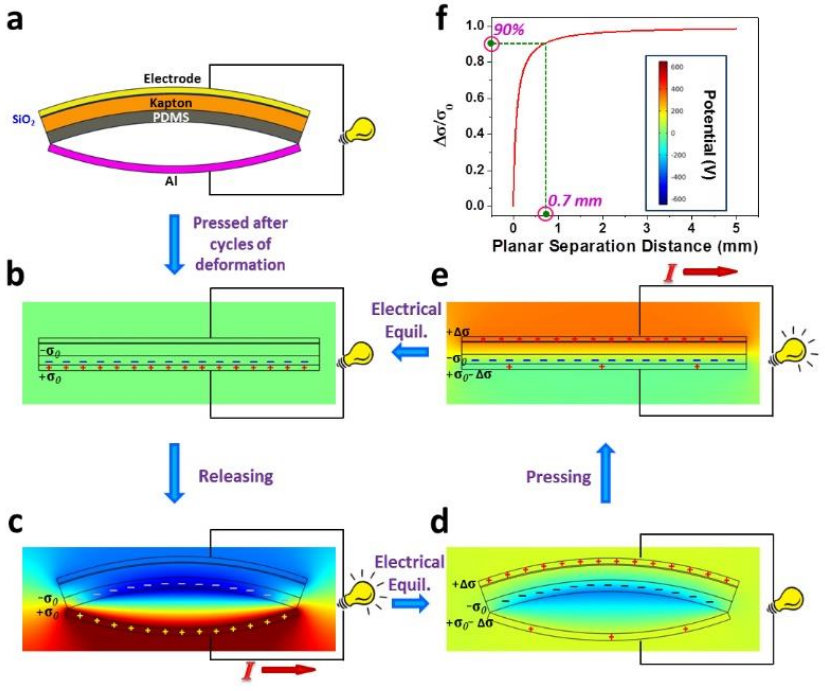

Figure 3.6 The working principle of the polymer-metal based TENG. (a) A two-dimensional sketch showing the initial state of the TENG before any deformation. (b-e)

The finite element simulation of the periodic potential change between the two electrodes upon cyclic deformation, showing the driving force for the back-and-forth charge flow generated by the TENG. A cycle is generally divided into four states, (b) device under pressing, (c) deformation released, (d) charges transferred, and (e) device gets pressed again, and finally charge transferred again to cycle back to (b). (f) The relationship of the ratio between transferred charge density ($\Delta\sigma$) and triboelectric charge density (σ_0), with the planar separation distance, which shows the importance of the effective charge/plate separation. The inset is the scale of the voltage for the simulation results presented in (b-e).[81]

Under the above described periodic deformation scenario, the electric output measurement was performed on an arch-shaped TENG device in a size of 3 cm×2.8 cm, with the triggering frequency of 6 Hz and controlled amplitude. Since the accumulation of the triboelectric charges increases and reaches equilibrium in a certain period of time after multiple cycles, the output will gradually go up in the first stage upon deformation. Then, the open-circuit voltage (V_{OC}) will stabilize at 230 V (Figure 3.7a), measured by an electrometer with infinite input resistance. From the inset of Figure 3.7a, when the bottom Al is connected to the positive probe of the electrometer, upon the release of the pressing force a positive voltage is generated because of the immediate charge separation. Since in an open-circuit condition the electrons cannot flow to screen the induced potential difference between the two electrodes, the voltage will hold at a plateau until the subsequent pressing deformation in the second half cycle. As shown in Figure 3.7b, the peak value of the short-circuit current (I_{SC}) reaches 94 μA, corresponding to the half cycle of pressing that is in higher straining rate than releasing. The integration of the each current peak gives the total charges transferred in a half cycle of deformation. Moreover, when the connection polarity to the electrometer is switched, both the voltage and current signal will be completely reversed. The gap from the arch-shaped structure is a key factor

for the enhanced output, because without the SiO_2-film-introduced bending, there will be much smaller and unstable electrical output.

Besides the triboelectric charge density and the separation distance of the two plates, another factor that could make an influence on the output of the TENG is the deformation frequency, which affects the straining rate. Since the mechanical energy from the environment is always irregular and varies in frequencies, it is necessary to study the dependence of TENG's output on the frequency. Thus, we tested the TENG device in a series of 9 different frequencies, from 2 to 10 Hz, with the amplitude of the triggering motor remaining constant. As shown in Figure 3.7c, V_{OC} almost remains the same at different frequencies. The probable reason is that at the open-circuit condition, it doesn't involve the dynamic process of charge transfer. The voltage is only determined by the triboelectric charge density and the plate separation at any given time. But for the short-circuit current, it presents a very clear increasing trend with the increase of frequency, from 35 μA at 2 Hz to 130 μA at 10 Hz (Figure 3.7d), because the deformation rate increases with deformation frequency, which leads to a higher flow rate of charges, i.e., higher current, but the total amount of charges transferred is constant at given triboelectric condition and separation distance. This is confirmed by the integration of every single current peak from each of the 9 different frequencies (inset of Figure 3.7d). Therefore, the instantaneous power output increases with the increase of frequency, so that it will be more eligible to drive electronic devices with larger power consumption. From the above results, when the frequency reaches 10 Hz, the instantaneous power output reaches up to 3.56 mW/cm^2 and 128 mW/cm^3.

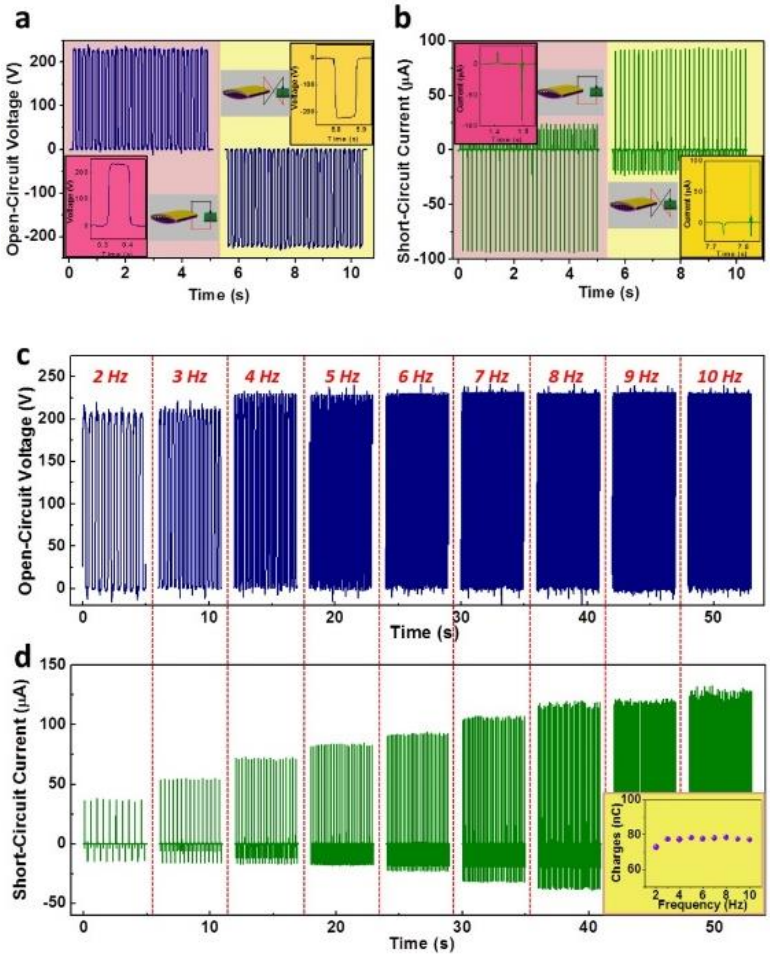

Figure 3.7 Characterizing the performance of the arch-shaped contact-mode TENG. (a) The open-circuit voltage and (b) the short-circuit current of the TENG under the deformation frequency of 6 Hz. These are studies under both the forward connection (Al connected to the positive probe) shown at the left-hand side and reverse connection shown at the right-hand side. The insets are the magnified output curve in one cycle, and the sketch of the corresponding connection polarity. (c-d) The influence of the deformation frequency on (c) the open-circuit voltage and (d) the short-circuit current. The inset in (d) is the integration of a single current peak from each frequency, which gives the total charges transferred in a half cycle, showing that the total contact charges generated is almost independent of the deformation frequency.[81]

In practice, the output power to the load depends on the match between the load and the power source. When the working TENG (under frequency of 6 Hz) is directly connected to the loads of different resistances, we can find that the current through the

load will generally decrease from I_{SC} when the resistance increases from zero (Figure 3.8a), but the voltage across the load will follow an opposite trend and saturate to V_{OC} when the resistance gets infinitely large. The instantaneous power on the load will reach the maximum value of 9 mW at a load resistance of ~3 MΩ (Figure 3.8b). Based on the above results, we have estimated the energy conversion efficiency for this structure. Since the thickness of the substrate used here has little influence on the electricity generation process but does consume a lot of mechanical energy, the output efficiency can be dramatically high if the thickness of the plate is reduced according to the feasible engineering fabrication while still maintain the mechanical integrity of the TENG. Based on experimentally achievable design and fabrication, the efficiency of this structure with the same gap distance could be as high as 10~39%. In the other case, when the TENGs are used to drive polar devices such as diodes, the AC signals of the NG needs to be rectified before connected to the load. We can find that both the rectified voltage and current follow a similar trend (Figure 3.8c) with the scenario of no rectification, and the only difference is that the voltage will not saturate but continues to increase as the load resistance above 100 MΩ. The maximum output power is 7.2 mW at a load of ~2 MΩ (Figure 3.8d), which is a bit smaller than the maximum power of 9 mW without rectification, simply because of the energy loss of the rectifier unit.

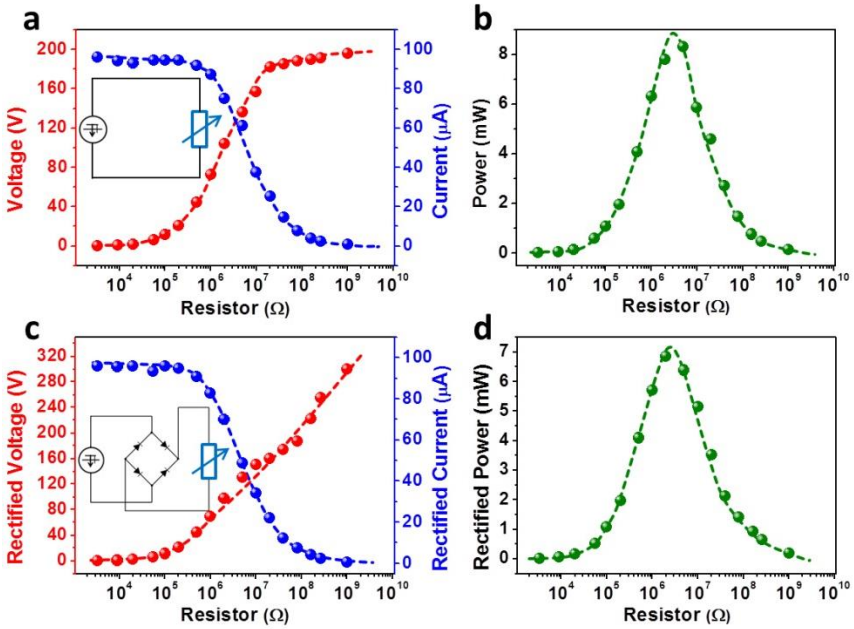

Figure 3.8 The arch-shaped TENG as a direct power source to drive electronic devices. (a-b) When the TENG driving a load without rectification, the dependence of (a) the output voltage, current and (b) instantaneous power on the load resistance. (c-d) When the TENG driving a load with rectification, the dependence of (c) the output voltage, current and (d) instantaneous power on the resistance of the load. All of the dots are measured values and the solid lines are fitted curves.[81]

In summary, by rational design of an arch-shaped structure based on the contact electrification between a polymer and a metal film, we demonstrated a novel type of triboelectric nanogenerator with much improved power output of 3.56 mW/cm^2 and 128 mW/cm^3 (voltage of 230 V and current of 0.13 mA); and an estimated conversion efficiency of as high as 10-39% is possibly achievable. Such high output is achieved through controllable and revolutionary improvement on the effectiveness of charge separation and re-contact process by purposely introducing thermal stress in the device fabrication. The mechanism for the first polymer-metal based TENG is illustrated through numerical simulation. The application of using the TENG as a power source has been demonstrated for two scenarios. This study demonstrates a ground breaking

progress in development of high power triboelectric nanogenerators, with outstanding applications as an effective power source for self-powered systems in sensor networks, portable electronics, biosensing and health care, environmental and infrastructure monitoring and security.

3.4 In-plane sliding-mode triboelectric nanogenerator

The previously-demonstrated TENGs are all based on the vertical separation of two triboelectrically-charged (tribo-charged) planes to generate the electric polarization/field in the direction perpendicular to the planes. To realize such vertical charge separation, an air gap is mandatory to be created after the releasing of the external force, which usually requires sophisticated design of the device structures and makes the TENG difficult for packaging and practical use for some cases. In this study, we demonstrated a new TENG that are designed based on the in-plane sliding between the two surfaces in lateral direction. With an intensive triboelectrification facilitated by sliding friction, a periodic change in the contact area between two surfaces leads to a lateral separation of the charge centers, which creates a voltage drop for driving the flow of electrons in the external load. With the help of finite-element simulation, the working principle has been elaborated. Under this new working mode, the open-circuit voltage of the sliding- TENG reaches 1300 V, with a peak short-circuit current density of 4.1 mA/m^2 and a peak power density of 5.3 W/m^2, which is capable to drive hundreds of electronic devices (such as LEDs) instantaneously. In this demonstration of the in-plane charge separation based TENG, we systematically studied the influence of the sliding parameters (the displacement and the velocity) on the electrical outputs, which

illuminated the distinct characteristics of the TENGs in this new working mode. This work will open up a new category of TENGs, with numerous advantages and potential applications of harvesting different types of naturally-existing mechanical energies, as well as active sensors.[82]

The sliding-triboelectric nanogenerator is structurally composed of two plates (71 mm × 50 mm) with glass slides as the supporting substrates to ensure the surface flatness (Figure 3.9a). Polyamide 6,6 (Nylon) and polytetrafluoroethylene (PTFE) films, the two polymers at the opposite ends of the triboelectric series, are purposely chosen as the triboelectric layers adhered on surfaces of the glass slides, respectively, for effective electrification during sliding. On each polymer film, a layer of metal electrode was deposited on the side next to the glass slide (named as top electrode for the one on Nylon and bottom electrode for the one on PTFE). The two plates are kept in parallel to each other and the polymeric surfaces are in intimate contact. As driven by the mechanical motion/vibration along the long-edge of the plate, the two plates slide against each other, with the contact area changing periodically. In order to enhance the triboelectric charge density on the surface, the PTFE film was dry-etched using inductive coupled plasma (ICP) to create aligned nanowire-structures (Figure 3.9b), which will increase the surface roughness and the effective surface area. As shown in the scanning electron microscopy (SEM) images (Figure 3.9c), the PTFE surface is uniformly covered with nanowire-structures, with an average length of ~ 1.5 μm. As illustrated in Figure 3.9d, during the real-time measurement, the PTFE-covered plate was bonded to a stationary stage, while the Nylon side was fastened to a parallel flat-end rail guide, which was connected to a linear motor for inducing an in-plane sliding motion.

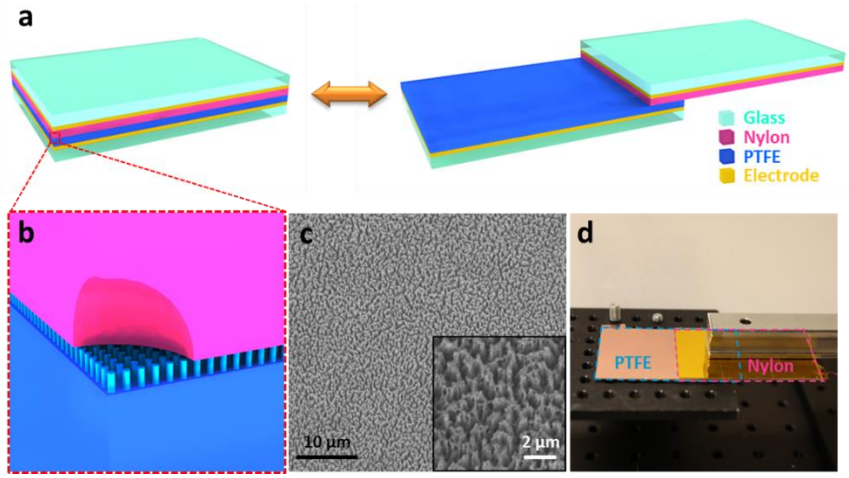

Figure 3.9 Device structure of a sliding-triboelectric nanogenerator (TENG). (a) The schematic diagram showing the structural design of the TENG in two sliding states: the overlapping position (on the left) and the separation position (on the right). (b) The magnified schematic of the surface between the two polymeric films, showing the fabricated nanowire array on PTFE surface. (c) SEM image of the PTFE surface with etched nanowire structure at the tilted view of 30°, the inset is the SEM image in higher magnification. (d) The photograph of a typical sliding-driven TENG on the measurement stage.[82]

The sliding-induced electricity generation mechanism is schematically depicted in Figure 3.10a. In the original position (Figure 3.10a-I), the two polymeric surfaces fully overlap and intimately contact with each other. Because of the large difference in the ability to attract electrons, the triboelectrification will leave the Nylon surface with net positive charges and the PTFE with net negative charges with equal density. Since the tribo-charges on the insulators will only distribute in the surface layer and will not be leaked out for an extended period of time, the separation between the positively-charged surface and negatively-charged surface is negligible at this overlapping position, and thus there will be little electric potential drop across the two electrodes. Once the top plate with the positively-charged surface starts to slide outward (Figure 3.10a-II), the in-plane charge separation is initiated due to the decrease in contact surface area. The separated

charges will generate an electric field pointing from the right to the left almost parallel to the plates, inducing a higher potential at the top electrode. This potential difference will drive a current flow from the top electrode to the bottom electrode in order to generate an electric potential drop that cancels the tribo-charge-induced potential. Because the vertical distance between the electrode layer and the tribo-charged polymeric surface is negligible compared to the lateral charge separation distance, the amount of the transferred charges on the electrodes approximately equals to the amount of the separated charges at any sliding displacement. Thus, the current flow will continue with the continuation of the on-going sliding process that keeps increasing the separated charges, until the top plate fully slides out of the bottom plate and the tribo-charged surfaces are entirely separated (Figure 3.10a-III). The measured current should be determined by the rate at which the two plates are being slid apart. Subsequently, when the top plate is reverted to slide backwards (Figure 3.10a-IV), the separated charges begins to get in contact again but no annihilation due to the insulator nature of the polymer materials. The redundant transferred charges on the electrodes will flow back through the external load with the increase of the contact area, in order to keep the electrostatic equilibrium. This will contribute to a current flow from the bottom electrode to the top electrode, along with the second half cycle of sliding. Once the two plates reach the overlapping position, the charged surfaces get into fully contact again. There will be no transferred charges left on the electrode, and the device returns to the state in Figure 3.10a-I. In this entire cycle, the processes of sliding outwards and inwards are symmetric, so a pair of symmetric alternating current peaks should be expected.

This in-plane charge-separation-induced potential difference and charge transfer can be verified through numerical simulation using COMSOL. The model constructed here has the same structure and dimensions (71 mm × 50 mm in surface) with the real device, and those two tribo-charged surfaces are assigned with a charge density of ±70 $\mu C/m^2$, respectively. The device is in open-circuit condition, which means no electron transfer between the two electrodes. As shown by the simulation results, when the two plates are in the fully aligned stacking position, which corresponds to the state in Figure 3.10a-I, there is no potential difference generated (Figure 3.10b). When the top plate slides about half way out (with a displacement of 41 mm), there will be a 2950 V potential difference between the two electrodes (Figure 3.10c); and this potential difference will increase to 1.03×10^5 V when the top plate just slides out of touching the bottom plate (with a displacement of 71 mm) (Figure 3.10d). In these simulation results of Figure 3.10b-d, the background planes show the potential distribution in the free space of air surrounding the TENG, as a result of the in-plane charge separation. We have also simulated the voltage between the two electrodes at a series of displacements from 11 mm to 91 mm. As shown in Figure 3.10e, the voltage keeps increasing when the displacement gets larger, even after the plates slide out of each other. This is because the voltage is the path-integral of the electric field along the displacement. On the other hand, the amounts of transferred charges between the two electrodes under these different displacements are also simulated through equating the potential of the electrodes at the short-circuit condition. As shown in Figure 3.10e, the amount of transferred charges increases linearly with the displacement before the top plate slides out of the bottom plate (with the displacement smaller than 71 mm). But different from the trend of the voltage,

the amount of transferred charges will saturate at the total amount of tribo-charges on one surface after the plates have fully slid out of each other, because there is no further charge separation here. So, the effective displacement region for generating electricity is between 0 mm and 71 mm, where the contact area of the two plates is changed during the relative sliding of the two plates.

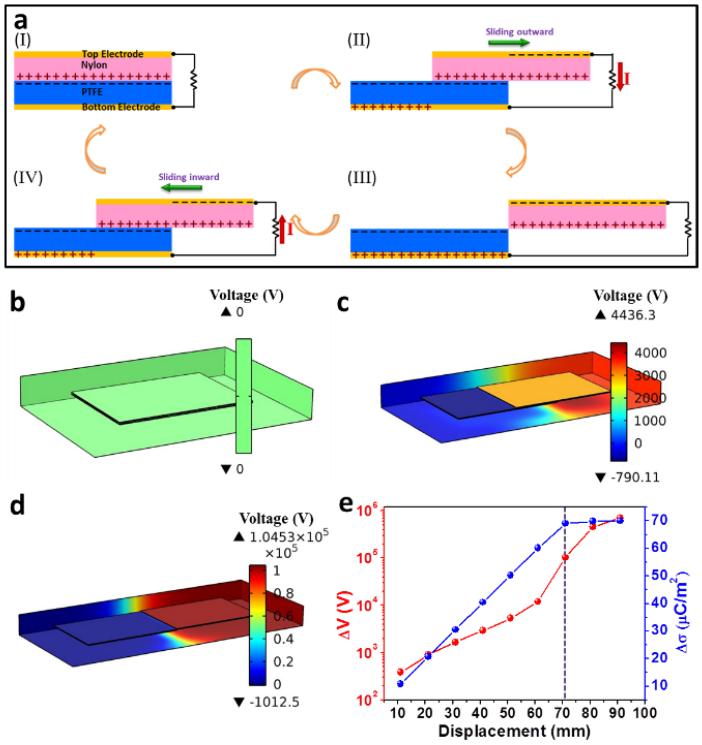

Figure 3.10 Working mechanism of the TENG based on in-plane charge separation. (a) The sketches that illustrate the electricity generation process in a full cycle of the sliding motion. (b-d) Finite element simulation of the potential difference between the two electrodes at consecutive sliding displacements: (b) 0 mm (the overlapping position); (c) 41 mm (sliding half way out); (d) 71mm (fully sliding out). (e) The curves of the simulated potential difference ΔV (red) and transferred charge density $\Delta\sigma$ (blue) *vs.* the sliding displacement from 11 mm to 91 mm, in which the two plates fully slide out of each other at 71 mm (marked by the purple dot line).[82]

The electrical output of the sliding-TENG was measured, with one plate guided by the linear motor in the direction parallel to the long-edge of the plates. The sliding

displacement was 71 mm, which was the same with the length of the plate and thus covered the entire effective region for generating electricity (as mentioned above). The sliding movement was in a symmetric acceleration-deceleration mode (the instantaneous sliding velocity was plotted as the pink curve of Figure 3.11d), with the acceleration rate of ±20 m/s^2. The open-circuit voltage (V_{OC}) was measured by an electrometer with very large input resistance. The electrode at the back of Nylon film was connected to the positive probe. When the plates in the TENG slid from the contact position to the separated position, the V_{OC} jumped from 0 to ~1300 V (Figure 3.11a), which reflects the induced potential difference between the two electrodes by the in-plane charge separation. At the separation position, the V_{OC} decayed a little bit, due to the slow charge leakage through the electrometer. When the TENG slid back to the contact position, the V_{OC} jumped back to 0. The density of the transferred charge ($\Delta\sigma$) was also measured at the short-circuit condition. As shown in Figure 3.11b, the charges with a density of ~105 μC/m^2 transferred back and forth between the two electrodes, while the plates slid in and out. Since the plates got fully separated in each cycle, the transferred charge density should approximately equal to the triboelectric charge density on the polymeric surfaces, according to the relationship in Figure 3.10e. With these experimental results, the measured V_{OC} is smaller than the simulated potential difference in Figure 3.10d, which is possibly due to the limitation of the electrical measurement system to record such a high voltage and the imperfection from the ideal open-circuit condition. The transfer of the charges between the electrodes in the outer circuits produced an alternating-current output, with the peak short-circuit current density (J_{SC}) of 4.1 mA/m^2 at a maximum sliding velocity of 1.2 m/s (Figure 3.11c). The area under each current density peak is

the amount of charge density transferred in each sliding motion. The enlarged J_{SC} curve in one single cycle is displayed in Figure 3.11d, together with the corresponding curve of the sliding velocity. We can find that the current output has a symmetric profile and synchronizes very well with the velocity of the sliding motion. With such a power output converted from the sliding motion, hundreds of commercial light-emitting diodes (LEDs) can be instantaneously driven by a single TENG device (Figure 3.11e).

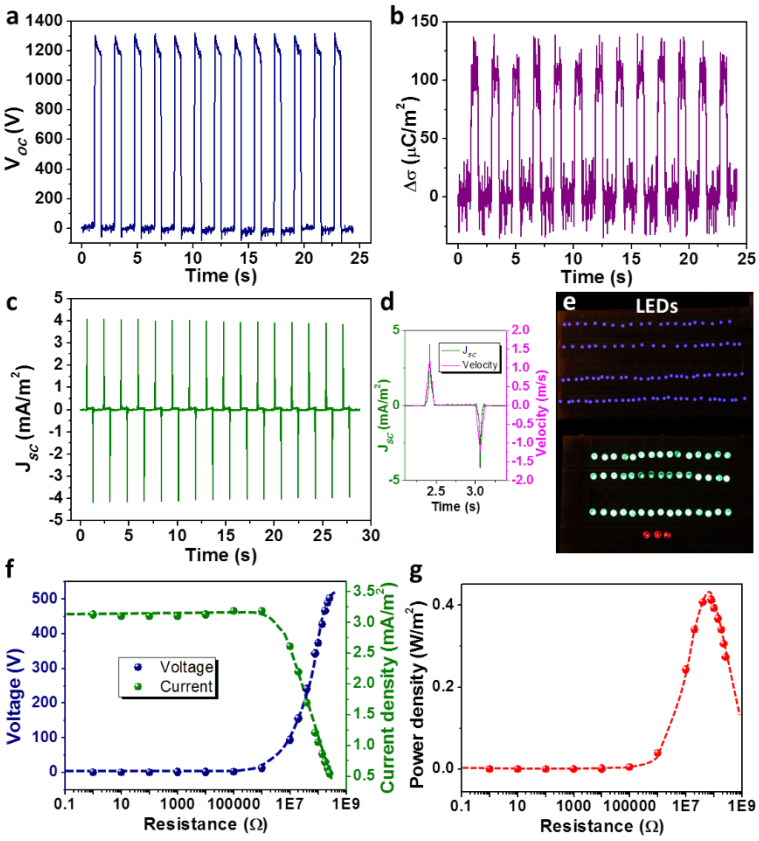

Figure 3.11 Performance of the TENG driven by the cycled sliding motion. (a) The open-circuit voltage (V_{OC}), (b) the density of transferred charges ($\Delta\sigma$), and (c) the short-circuit current density (J_{SC}) under the in-plane sliding with the displacement of 71 mm and the acceleration of 20 m/s^2. (d) The enlarged profile of J_{SC} within one cycle (green curve), with the corresponding curve of the instantaneous sliding velocity (pink). (e) The snapshot of ~160 commercial LEDs in serial-connection directly driven by a TENG under sliding. (f-g) The dependence of (f) the output voltage (blue), current density (green) and (g) the power density on the resistance of the external load.[82]

In practice, the TENG's effective output power to the loads depends on the match with the resistance of the load. As shown in Figure 3.11f, when the resistance is below ~1 MΩ, the output current density and the voltage have little changes from the short-circuit condition: the current density remains at a value of J_{SC} while the voltage stays close to 0. This is because the TENG has infinitely-large inner resistance. When the resistance goes beyond 1 MΩ, the current density will drop with the increase of the resistance; while the voltage on the load rises up. Consequently, the instantaneous power density on the load (Figure 3.11g) remains close to 0 with the resistance below 1 MΩ, and reaches the maximum value of 0.42 W/m^2 at a resistance of ~50 MΩ. This is the maximum output power density on the device.

The output of the planar-sliding-driven TENG is directly determined by the parameters of the sliding motion—the displacement and the velocity, because the flow of electricity originates from the tribo-charge separation under sliding. As simulated in Figure 3.10e, before the two plates fully slide out of each other (with a displacement smaller than 71 mm), the voltage increases monotonically with the displacement. Also, if we assume a uniform tribo-charge distribution on the polymeric surface, the total amount of transferred charges will have a linear relationship with the displacement, which can be expressed in charge density as:

$$\frac{\Delta\sigma}{\sigma_0} = \frac{\Delta L}{L_0} \tag{3.2}$$

where $\Delta\sigma$ is the transferred charge density, σ_0 is the tribo-charge density on the polymeric surface, ΔL is the sliding displacement and L_0 is the length of the plate

which is 71 mm. According to the definition of current density (J), it has the following relationship:

$$J = \frac{d\Delta\sigma}{dt} \tag{3.3}$$

where t is the time. After merging the equation (3.2) into (3.3), we will have

$$J = \frac{\sigma_0}{L_0} \cdot \frac{d\Delta L}{dt} = \frac{\sigma_0}{L_0} v \tag{3.4}$$

where v is the instantaneous velocity of the sliding. So, the current density should be proportional to the instantaneous velocity at which the two plates are being separated.

A systematic study of these relationships between the electrical outputs (V_{OC} and J_{SC}) and the sliding conditions was carried out experimentally. In the first group of experiments, the electrical outputs were measured under a series of 7 different sliding displacements from 11 mm to 71 mm, with an acceleration kept at 20 m/s^2. As shown in Figure 3.12a, the V_{OC} increases with the displacement, which is in accordance with the simulation results in Figure 3.10e. And the measured transferred charge density $\Delta\sigma$ displays a linear relationship with the displacement (the inset of Figure 3.12b), which can be linearly fitted with the correlation coefficient of 0.981. As for the peak value of J_{SC} which is in proportional to the maximum velocity v_m, it also has a positive correlation with the displacement (Figure 3.12b). This is because v_m has such a relationship with the displacement:

$$v_m = \sqrt{a \cdot L} \tag{3.5}$$

where a is the acceleration and ΔL is the total displacement (the displacement for each acceleration and deceleration process is $\Delta L/2$, respectively).

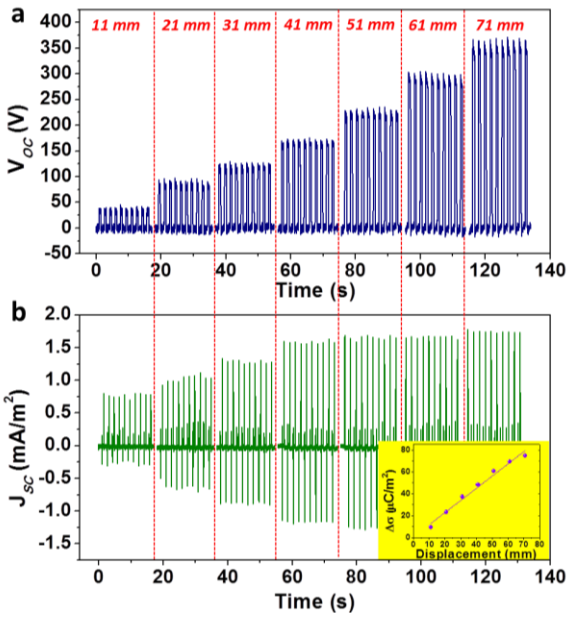

Figure 3.12 Influence of the sliding displacement on the electrical outputs. (a) The open-circuit voltage (V_{OC}), (b) the short-circuit current density (J_{SC}), and the measured transferred charge density (Δσ) (the inset of b) under 7 different sliding displacements from 11 mm to 71 mm.[82]

When the sliding displacement remains at a constant value of 71 mm, the maximum velocity of the sliding is solely determined by the acceleration. Thus, we varied the acceleration to investigate the velocity's influence on the output. As shown in Figure 3.13a, V_{OC} has very little increase with the rising acceleration, which is also consistent with the theoretical expectation that V_{OC} is only determined by the displacement. However, the changing rate of the voltage will depend on the sliding velocity. The higher the velocity, the faster the voltage increases/decreases in sliding. Through differentiating the curve of V_{OC}-t, the maximum slopes of voltage at the rising edges is plotted with the corresponding maximum sliding velocity in Figure 3.13b, which shows a clear positive correlation. As for the output current, the peak value of J_{SC} gets larger at higher acceleration, because of the larger maximum velocity in sliding (Figure

3.13c). However, the sliding velocity has no influence on the transferred charge density $\Delta\sigma$ under the constant displacement (Figure 3.13d).

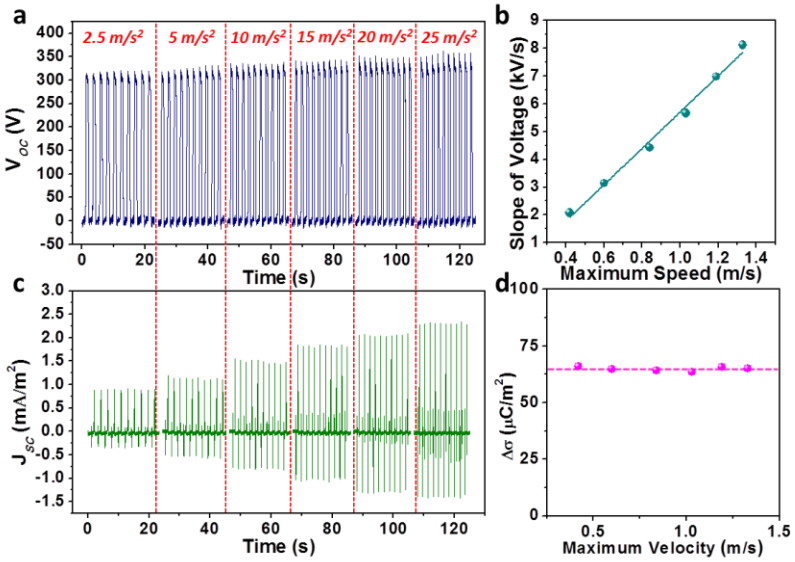

Figure 3.13 Influence of the sliding velocity (acceleration) on the electrical outputs. (a) The open-circuit voltage (V_{OC}) under 6 different sliding accelerations (which correspond to different maximum velocity). (b) The plot of the maximum slope of the voltage change *vs.* the maximum velocity. The dots are measured value and the line is the fitted result. (c) The short-circuit current density (J_{SC}) under 6 different sliding accelerations. (d) The plot of the measured transferred charge density ($\Delta\sigma$) *vs.* the maximum velocity.[82]

Because the essence in the working mechanism of the sliding-TENG is the cycled switching between the separation and full contact of the opposite tribo-charges, there should be little electricity generated in the following two cases: (1) If the sliding motion does not result in the change of the contact area between two plates, for example, if a smaller plate slides inside the perimeter of a larger plate at all time, then little output can be measured. This is because there is no polarization generated in this case. (2) If the two plates do not fully in tight contact with each other at the overlapping position, there is always a vertical gap distance between them, which results in two cases. One, little triboelectric charges are generated. The other case is that, if there are triboelectric charges

on the plates, the gap between them in the vertical direction quickly decays the strength of electrostatic interaction, resulting in a reduced output. When we gradually increase the vertical distance between the two plates of the TENG from 0 to 2 mm, the output voltage, current and transferred charges all quickly decay to zero.

The working principle of this in-plane-separation based TENG is essentially similar to that of the existing vertical-separation based TENG. However, the characteristics of the electrical output differ a lot. As shown in the experimental comparison of the TENGs in these two modes with the same materials and dimensions (Figure 3.14), the short-circuit current of the TENG in the planar-sliding mode has a much smaller peak value (~15 μA) but a longer pulse (Figure 3.14a), compared to a much larger peak value of (~240 μA) but a much shorter pulse by the TENG in the vertical-touching mode (Figure 3.14b). This results from the difference in the charge separation process: in the planar-sliding mode, the length of the effective displacement is very large (71 mm in this experimental case), thus the charge transfer takes much longer time, while in the vertical-touching mode, the effective displacement length is much smaller (less than 1 mm), resulting in a much faster charge flow. Thus, the sliding-TENG should generally deliver a smaller peak instantaneous power than the TENG of the vertical-touching mode. However, as for the total amount of charges flowing through the external load for each displacement, the TENG of the planar-sliding mode delivered a larger value (380 nC) than the TENG of the vertical-touching mode (330 nC), which stands for a higher triboelectric charge density on the polymeric surface. The probable reason is that the lateral sliding between the two polymeric surfaces provides much more frictions, thus could more effectively facilitate the triboelectrification than the vertical-touching mode.

As a power source, the electricity generated by the TENGs needs to be regulated and stored in an energy storage device before powering electronic devices. It is the total amount of charges, rather than the peak current, that acts as the key factor for the efficiency of charging an energy storage device. As shown in Figure 3.14c-d, the TENGs in these two modes were used to charge a capacitor of 22 μF. It took 313 cycles for the sliding-TENG to charge such an empty capacitor to 10 V, while it took 365 cycles for the TENG in the vertical-touching mode. So, the proposed TENG in the planar-sliding mode shows the superiority when combined with an energy storage device. Besides the above advantage, this new TENG in the planar-sliding mode has several other unique advantages. Firstly, this novel design of TENG does not need a gap between the two plates. Thus it will be unnecessary to have elastic supporting components (such as springs) between the two plates to ensure the effective charge separation. This brings up a lot of convenience in packaging the TENG device. Secondly, there is no need for a large amount of mechanical energy input to trigger this type of TENG, which can help to improve the energy harvesting efficiency. The mechanical energy only needs to overcome the work done by the sliding friction between the two plates. Thirdly, this TENG is simple in structure, easy in fabrication, compact in volume, stable in performance, cost-effective and robust. With these great advantages, such in-plane charge-separation-based TENGs can harvest mechanical energies in the form of relative sliding that are supplied by many different working configurations, for example, the relative rotation of two contacting plates, the vibration of the piston, the rotation of the axis to its tube, and so on. Besides, those mechanical energies that can drive the relative sliding between two objects can also be harvested using this principle of in-plane charge-

separation-based TENG, which can greatly expand the application of this type of TENG to scavenge mechanical energy from wind power, oceanic wave, human activities, and so on.

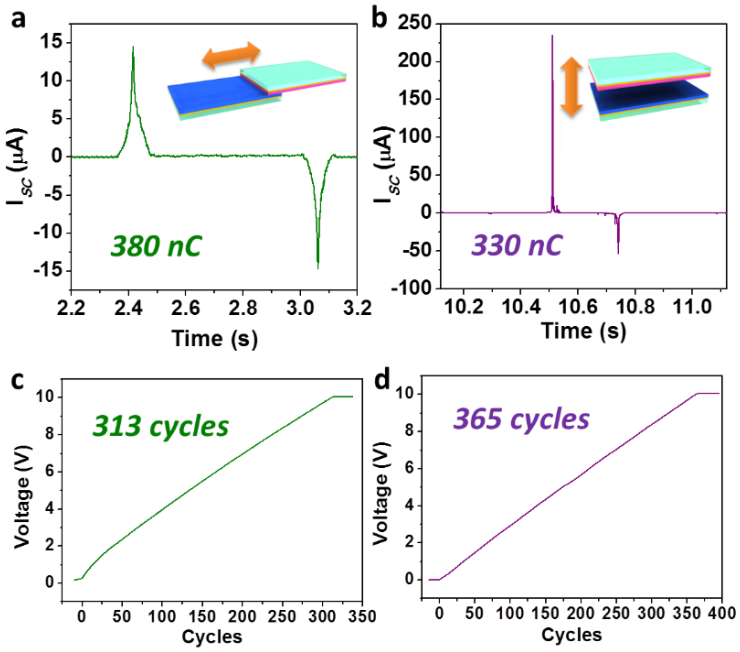

Figure 3.14 Comparison between the TENGs of the planar-sliding mode and the vertical-touching mode. (a-b) The profiles of the short-circuit current (I_{SC}) peaks within one cycle: (a) the TENG of the planar-sliding mode, (b) the TENG of the vertical-touching mode. The insets are the schematics showing the corresponding working modes. The amounts of transferred charges from a single displacement have been marked in the figures. (c-d) Capacitors of 22 μF were charged from 0 V to 10 V by the TENGs of the two modes, respectively: (c) the TENG of the planar-sliding mode, which takes 313 displacement cycles; (d) the TENG of the vertical-touching mode, which takes 365 displacement cycles.[82]

In summary, we have demonstrated a newly designed triboelectric nanogenerator based on the in-plane separation of triboelectric charges. Through converting the mechanical energy in the planar-sliding motion, the TENG delivered an open-circuit voltage of 1300 V and a short-circuit current density of 4.1 mA/m^2, with the maximum instantaneous power of 5.3 W/m^2, which was able to drive hundreds of electronic devices (such as LEDs) simultaneously. The dependence of the electrical outputs on the sliding

motion has been systematically studied, both theoretically and experimentally. Compared with the existing vertical-touching based TENG, the sliding-based TENG drives a larger amount of charges through the external load in each cycle, which is more efficient in charging an energy storage device. This study opens up a new direction in triboelectric nanogenerators, and paves a way for a lot of potential applications in harvesting mechanical energy from human activities, rotating tires, mechanical equipment, wind power, ocean waves and so on. Furthermore, with the relationship between the electrical output and the sliding motion being calibrated, the sliding-based TENG could potentially be used as a self-powered displacement/speed/acceleration sensor.

3.5 Segmentally-structured rotary disk triboelectric nanogenerator

Here in this work, we developed a segmentally-patterned disk-shaped TENG, in which a periodic overlapping and separation process of the two groups of sectors on the two concentric and closely-contacted disks is achieved by relative rotation. This design not only introduces the sliding triboelectrification between the two contacting surfaces of the sectors, but also facilitates a rotation-induced periodic, in-plane charge separation for electricity generation. This in-plane charge-separation-based working mechanism was demonstrated with the combination of numerical calculations and experiments. With this rotation-based TENG, both finer segmentations and larger rotation speed lead to a faster charge transfer between the electrodes through an external circuit, producing a large current output at a high frequency (117. 6 μA and 29.0 mA/cm^2 of 66.7 Hz at a rotating speed of 1000 rpm). Owing to its high output current and large frequency, multiple light-emitting diodes (LEDs) were lit up continuously, and a power storage unit such as a

capacitor was quickly charged. The disk TENG is an important progress toward the practical application of nanogenerators and self-powered systems.[59]

The basic structure of the disk TENG is composed of two disk-shaped components with four sectors each, as schematically illustrated in Figure 3.15a. In the fabrication of the TENG device, two polymethyl methacrylate (PMMA) sheets were firstly processed by laser cutting to form the desired four-sector-structured cyclostyle that served as the templates for the effective contacting parts of the TENG. Then, a 50-μm-thick Kapton film with Au electrode deposited on the back side was manually-patterned into this exact shape and then securely attached onto one of the templates, while a piece of Al foil tailored into the same shape was attached on the other template. The Al part and Kapton part was brought to a face-to-face intimate contact and the Al part was driven to spin on the surface of the Kapton around their common axis. To promote the triboelectrification and increase the effective contact area between the two layers, Kapton nanorod (NR) array was created on the Kapton surface by a top-down approach through inductive coupled plasma (ICP) reactive ion etching, as displayed in the inset of Figure 3.15a. Scanning electron microscopy (SEM) images of the Kapton NRs are shown in Figure 3.15b. After a two-minute ICP etching, the NRs were uniformly distributed on the surface of Kapton, with an average diameter and length of 150 nm and 600 nm, respectively. The length of the NRs increases with the etching time. Figure 3.15c is a photograph of the two parts of the disk-shaped TENG with a diameter of 4 inches. The total effective area of the TENG device is 40.54 cm^2.

The disk TENG in this work presents a different working mode from the vertical contact-separation based configuration. The working principle of the disk TENG is based

on the triboelectrification and the relative-rotation-induced cyclic in-plane charge separation between Al and Kapton, as shown in Figure 3.15d. In the relative rotation, the Al surface and Kapton surface slide one relative to the other, so that the electrons will be injected from the Al foil to the inner surface of the Kapton film, leaving net positive charges on the Al foil and net negative charges on the Kapton film. The electricity generation process of the disk TENG can be divided into four stages: in Stage I, the two disks are at an overlapping position. Since the two charged surfaces are closely contacted with no polarization, there will be no potential difference between the two electrodes, thus no current flow in the external load. When the Al foil rotates in reference to the Kapton film, the corresponding two segments start to have a partially mismatched contact area (Stage II), the in-plane tribo-charges are thus separated in the direction almost parallel to the sliding direction, which will induce a higher potential on the Al layer than the Kapton's electrode, thus the electrons in the electrode attached to the Kapton film will be driven to flow to the Al foil through an external load (forming a current flow in the reverse direction), so that an opposite potential is generated to balance the potential difference created by the separated tribo-charges. In this process, the electrons keep flowing until the two disks reach fully mismatch in the contacting segmented areas (e.g. for 45^{o} of rotation in this case), which is represented by Stage III. At this moment, both the induced potential difference and the amount of transferred charges between the two electrodes reach the maximum values. In Stage IV as the top plate continues spinning, the Kapton surface begins to get contacted with another adjacent sector of Al foil, and the potential difference between two electrodes will drop with the decrease of the mismatch area. As a result, the electrons will flow back in the opposite direction from the Al foil to

the electrode attached to the Kapton film. Thus, the entire process will result in an alternating-current (AC) output. Such a charge transfer cycle will start over from Stage I when the two plates reach a complete overlapping again.

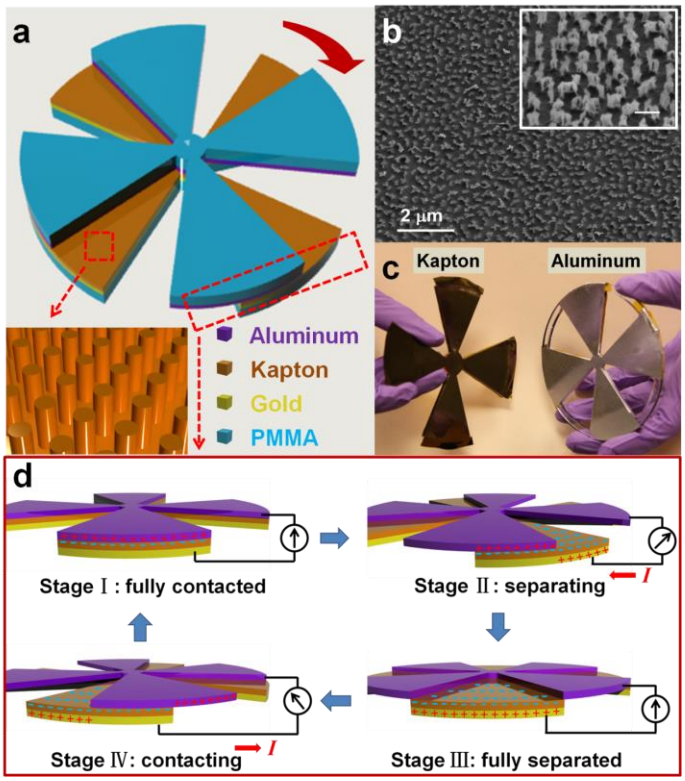

Figure 3.15 The basic structure and proposed working principle of the disk TENG. (a) A schematic illustration showing the structure design of the disk TENG. The inset (bottom left) is an enlarged figure showing the Kapton nanorod array created on the surface area. (b) A top-view SEM image of the Kapton nanorods showing its uniformity in a large range. The inset is a high magnification SEM image of the Kapton nanorods in 30˚-tilted view. The scale bar is 500 nm. (c) A photograph showing the two parts of a real disk TENG. (d) Schematic illustrations showing the proposed working principle of the disk TENG with the electrons flow diagram in four consecutive stages within a full cycle of electricity generation. Please note that only one pair of sectors (the cross-section area entangled in Figure 1a was shown with surface charges for clarity of illustration, and the surface charges on the interface area between Al foil and Kapton film are hidden and are not drawn for easy presentation.[59]

To gain a more quantitative understanding of the proposed working principle of the disk TENG, we employed finite element simulation to calculate the potential

difference between the two electrodes and the transferred charge density at consecutive stages in a full cycle of charge transfer. The triboelectric charge density on the inner surface of Kapton film and Al foil was assigned as 75 $\mu C/m^2$. Figure 3.16a shows the calculation results in the four stages with rotation angles of 0˚ (Stage I), 22.5˚ (Stage II), 45˚ (Stage III), and 67.5˚ (Stage IV), respectively. In Stage I, the two layers are in full contact with each other, and there is no potential difference or charge transfer. Subsequently, as the top plate spins across this position, introducing the charge separation in the lateral direction, both the potential difference and the density of transferred charges between the Al foil and the Kapton's electrode will build up, via 1.62 kV and 34.5 $\mu C/m^2$ at 22.5˚ of half separation (Stage II), and finally to the peak values of 14.71 kV and 69.3 $\mu C/m^2$ at the fully separated position of 45˚ (Stage III). In the second half of this cycle (Stage IV), both the potential difference and transferred charge density decrease as the contact area begins to recover, and they show a symmetric behavior at the angle of 67.5˚ compared with Stage II.

The calculated potential difference and transferred charge density in a full cycle (from the 0˚ position to the 90˚ position with the step angle of 4.5˚) were depicted in Figure 3.16b. It can be observed that the transferred charge density displays a linear relationship with the rotating angle in each of the half cycles, while the potential difference presents a sharper peak, with an elevated slope around the fully separated position (the rotating angle of 45˚). Assuming a constant value of triboelectric charge density (σ_0) and uniform distribution of these charges on the inner surface of Al and Kapton, the amount of transferred charges should ideally equal to the amount of separated charges, which is proportional to the separated area (ΔA, for one sector).

Therefore, the transferred charge density ($\Delta\sigma$) has the following relationship with the rotating angle ($\Delta\theta$):

$$\frac{\Delta\sigma}{\sigma_0} = \frac{\Delta A}{A_0} = \frac{\frac{1}{2}\Delta\theta \cdot R^2}{\frac{1}{2}\theta_0 \cdot R^2} = \frac{\Delta\theta}{\theta_0} \tag{3.6}$$

where θ_0=45˚ is the rotating angle from the fully contacted position to the adjacent fully separated position, and A_0 is the maximum separated area for one sector. Then we can get

$$\Delta\sigma = \sigma_0 \cdot \frac{\Delta\theta}{\theta_0} \tag{3.7}$$

These theoretical expectations were further confirmed by electrical output measurements of the open-circuit voltage (V_{OC}), transferred charge density ($\Delta\sigma$), and short-circuit current density (J_{SC}), as shown in Figure 3.16c-e. The measurement was accomplished by rotating the Al-side disk at a constant speed of 45 rpm, with vertically intimate contact with the inner surface of Kapton (the detailed measurement setup is described in Methods). The output profiles of both the V_{OC} and the $\Delta\sigma$ show excellent consistency with the calculation results, with the V_{OC} showing a sharp peak and the $\Delta\sigma$ showing a linear "triangle waveform" behavior. Based on Equation (2), the dependence of J_{SC} on the angular speed (ω) can be deduced as:

$$J_{SC} = \frac{d(\Delta\sigma)}{dt} = \frac{d}{dt}(\sigma_0 \cdot \frac{\Delta\theta}{\theta_0}) = \frac{\sigma_0}{\theta_0}\frac{d(\Delta\theta)}{dt} = \frac{\sigma_0 \cdot \omega}{\theta_0} = \frac{\sigma_0}{\theta_0} \cdot 2\pi \cdot \frac{n}{60} \tag{3.8}$$

where n is the rotation speed measured in a unit of rounds per minute (rpm). Therefore, as long as the angular speed (ω) remains constant, the J_{SC} should remain a constant value in each half cycle, with a symmetric AC manner in a full cycle. The measurement result of the J_{SC} in Figure 3.16e is also in agreement with this anticipated trend, which shows a

"square waveform" behavior, differing a lot from the "pulse-like" current peak behavior in the previous works. This novel characteristic of NG's output performance may bring up new applications in various fields.

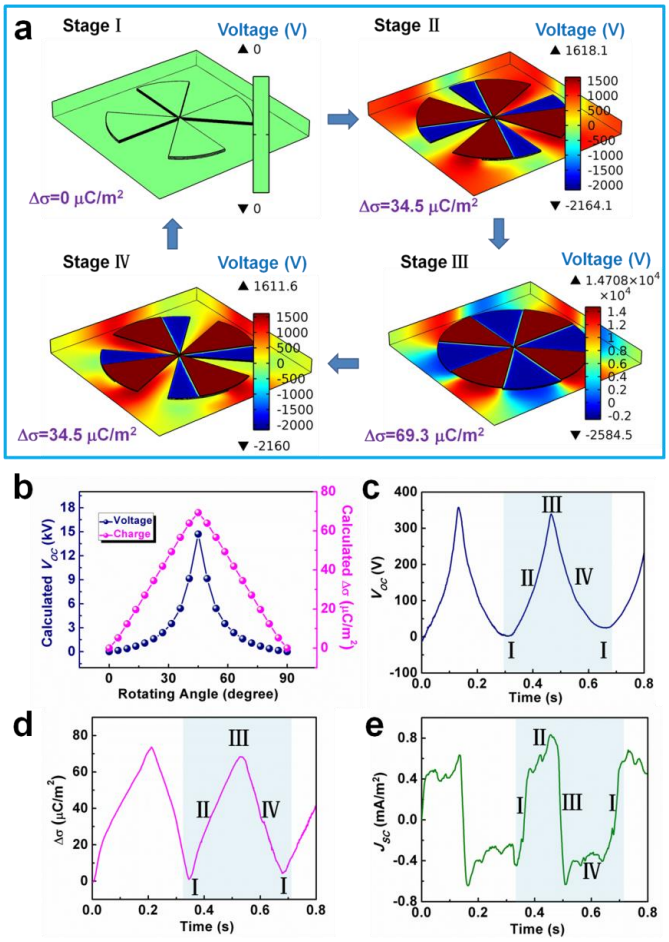

Figure 3.16 Numerical calculations of the charge transfer process of the disk TENG. (a) The numerical calculation of the potential difference and transferred charge density between two electrodes in four different stages within a full cycle of rotational motion: (I) fully contact, (II) half separated, (III) fully separated, and (IV) half contact. (b) A summary of the calculated open-circuit voltage and transferred charge density in a full cycle of rotation. The calculation takes place from the 0˚ position to the 90˚ position, and the step angle is 4.5˚. (c-e) The measured (c) open-circuit voltage, (d) transferred charge density, and (e) short-circuit current density in a full cycle of rotational motion at 45 rpm.[59]

The electricity generation process of the disk TENG relies on the magnitude and the rate of the triboelectric charge separation. In this regard, the configuration of the device, which is the number of sectors (N) that the entire disk is divided into, can be expected to play a significant role in the output performance of the TENG. For this purpose, we studied three types of TENG devices with the disks divided into 1 sector (Configuration 1, semi-circle), 2 sectors (Configuration 2), and 4 sectors (Configuration 3), respectively. Both theoretical calculations and measurements (with a rotation speed of 100 rpm) were carried out to demonstrate the effect of configurations on the output performance, as given in Figure 3.17. From the numerical calculation results in Figures 3.17a, c, and e, it could be found that as N increases from 1 to 4, both the calculated potential difference and transferred charge density drop to some extent. This trend is also observed in the measurement results of the V_{OC} and the $\Delta\sigma$ (Figure 3.17b, d, f), in which the V_{OC} falls from 315 V to 230 V, and the $\Delta\sigma$ decreases slightly from 43.6 $\mu C/m^2$ to 40.8 $\mu C/m^2$. The decreases of the V_{OC} and the $\Delta\sigma$ may result from the lower magnitude of polarization due to the shrunk separation distance for finer segments. On the contrary, the J_{SC} shows a phenomenal ascending trend from Configuration 1 to Configuration 3, mainly owing to the obvious increasing of the charge transferring rate due to the smaller rotation angle from fully contact to fully separation. Above all, it could also be found that the frequencies of all the three types of output signals double with the doubled segmentations. The experimental results fit well with the theoretical calculations on the basis of the following equation:

$$f = \frac{n}{60} \cdot N \tag{3.9}$$

where *n* is the rotating speed, and *N* is the number of divided sectors in a device. This group of comparisons shows a clear trend that with finer segmentation patterns, the amount of electricity generated by the TENG within a single rotation cycle will be largely increased owing to the multiple times (N) of charge transferred across the external load, which can greatly boost up the power conversion efficiency. Based on this finding, through patterning the disk with much finer segmentations using the techniques of photolithography and etching in the future work, the current output could be greatly improved.

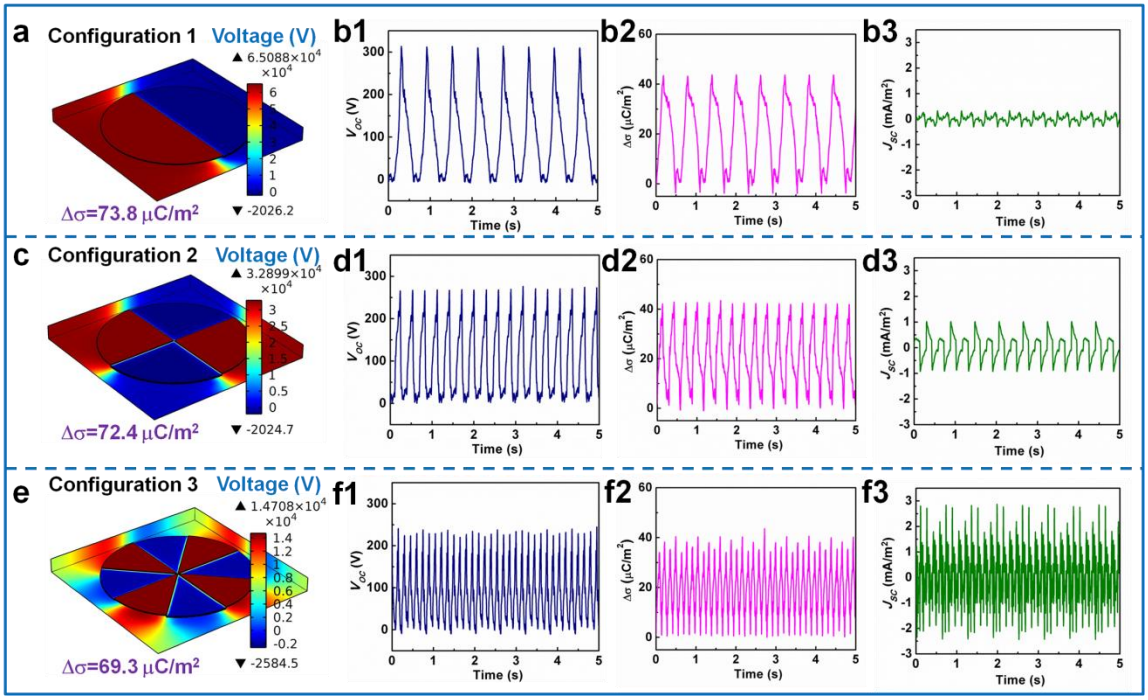

Figure 3.17 The configuration dependence of the output performance of the disk TENG. (a) The calculated open-circuit voltage and transferred charge density for the disk TENG with Configuration 1, in which the whole disk was divided into one sector (half of the full round shape). (b) The measured (b1) open-circuit voltage, (b2) transferred charge density, and (b3) short-circuit current density of Configuration 1 at 100 rpm. (c) The calculated open-circuit voltage and transferred charge density for the disk TENG with Configuration 2, in which the whole disk was divided into two sectors. (d) The measured (d1) open-circuit voltage, (d2) transferred charge density, and (d3) short-circuit current density of Configuration 2 at 100 rpm. (e) The calculated open-circuit voltage and transferred charge density for the disk TENG with Configuration 3, in which the whole disk was divided into four sectors (equivalent to the structure discussed in Figures 1 and 2). (f) The

measured (f1) open-circuit voltage, (f2) transferred charge density, and (f3) short-circuit current density of Configuration 3 at 100 rpm.[59]

As we have discussed in the theoretical analysis, the J_{SC} will increase linearly with the rotating speed *n*, while the V_{OC} and the $\Delta\sigma$ should not be influenced by the velocity, as long as the configuration of the device is fixed and the initial surface charge density keeps constant (Equation 3.8). To verify these relationships, a group of electrical measurements with variable rotating speeds were conducted on the TENG with Configuration 3, which is presented in Figure 3.18. Figures 3.18a and c show the measured open-circuit voltage and transferred charge density with different rotating speeds. Both the V_{OC} and the $\Delta\sigma$ almost keep constant with the rotating speed increased from 50 to 500 rpm. Though a slight decay at high speed occurs, which might result from the relatively low sampling rate of the voltage/charge meter, it is negligible with the V_{OC} of around 230 V and $\Delta\sigma$ of about 40 $\mu C/m^2$, as summarized in Figure 3.18b and d. Besides, the averaged slopes of the V_{OC} curve were also analyzed and shown in Figure 3.18b, with an increasing trend with ascending rotating speed because of the rising of the charge separation rate. Different from the V_{OC} and the $\Delta\sigma$, the J_{SC} is strongly enhanced with higher rotating speed (Figure 3.18e), and the good linear fitting in Figure 3.18f is coherently consistent with the behavior predicted by Equation (3.8). This linear relationship between the J_{SC} and the rotating speed implies that the magnitude of the output current of the disk TENG could be utilized to actively measure the angular speed of a rotating disk structure, which has potential applications in automobile braking systems or transmitting instruments. Moreover, though the magnitude of both the V_{OC} and the $\Delta\sigma$ is independent of the rotating speed, their frequencies, as well as the frequency of

the J_{SC} will be directly related to the velocity (Equation 3.9). The frequency analysis provides another reliable approach of employing the disk TENG as a self-powered velocity sensor. In the practical application, this could be simply realized by Fourier Transform of any output signal to acquire the frequency information.

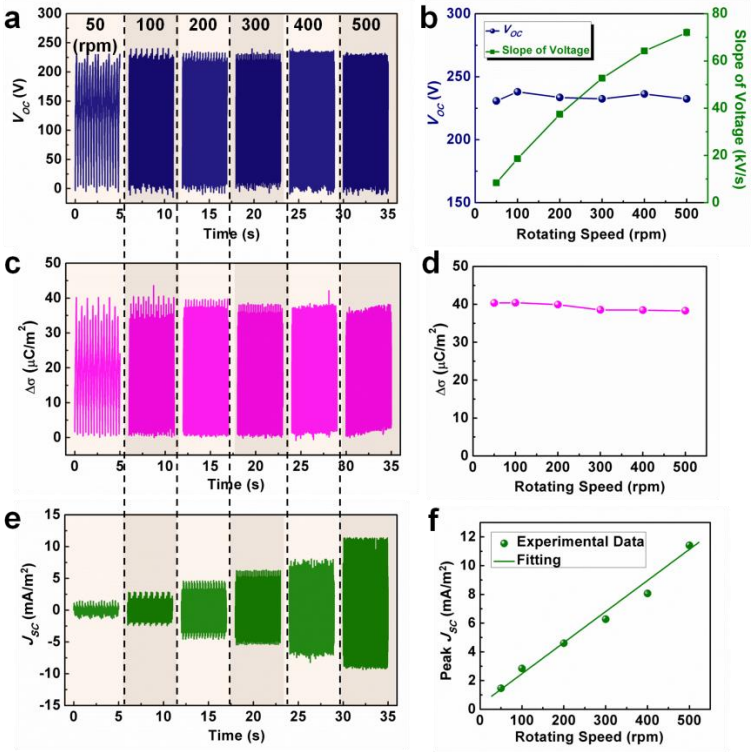

Figure 3.18 The influence of the rotating speed on the output performance of the disk TENG. (a) The measured open-circuit voltage with different rotating speeds from 50 to 500 rpm. (b) The summarized relationship between the open-circuit voltage/slope of the voltage and the rotating speed. (c) The measured transferred charge density with different rotating speeds from 50 to 500 rpm. (d) The summarized relationship between the transferred charge density and the rotating speed. (e) The measured short-circuit current density with different rotating speeds from 50 to 500 rpm. (f) The summarized relationship between the short-circuit current density and the rotating speed.[59]

This unique design of the segmentally-patterned disk TENG realizes multiple times of charge transfers within a full rotation cycle, which enables a fast charge transfer rate at high rotating speed. This will contribute to a large output current at a high

frequency. The current output of the demonstrated disk TENG at 1000 rpm could reach 29.0 mA/m^2 (Figure 3.19a), corresponding to 117.6 μA for the entire device area of 40.54 cm^2. The frequency of the J_{SC} is as high as ~66.7 Hz, which is even a bit higher than the frequency of the commercial electric power (50 Hz). After rectification, a high-magnitude and high-frequency DC like output was achieved (Figure 3.19b), which can be used to drive portable electronic devices (e.g. 60 serially-connected commercial LEDs) instantaneously, as shown in Figure 3.19c. As we can see from 4 consecutive frames in Figure 3.19c (with a time interval of only 0.1 s), the disk TENG achieves a continuous lighting-up of the LEDs, rather than just flashing in the previous works. Besides, such high frequency and large magnitude of electrical output imply a large averaged output current density and power density, which also shows its superiority when combined with energy storage units (e.g. batteries and capacitors) for long-term applications. As shown in Figure 3.19d, a 22 μF capacitor was charged by the disk TENG with variable rotating speeds at 100, 500, 1000, and 1500 rpm. The ultra-fast charging of energy storage unit by the disk TENG will largely improve the practicability of the TENG as an energy harvester in a self-powered system, and boost up the advancement of self-charging power cell.

For different practical applications, the energy harvester is usually applied on external loads with variable resistances, so that the output will deviate from the short-circuit or open-circuit conditions. In this regard, the output performance of the disk TENG was systematically studied at different loads. Figure 3.19e shows the resistance dependence of both output current density and voltage, from 10 Ω to 1 GΩ. The output current density decreases with the increasing resistance while the output voltage shows

the reverse trend, but both the current and voltage tend to saturate at both high and low ends of the resistance. The power density was also calculated by:

$$\frac{P}{A} = U \cdot \frac{I}{A} = U \cdot J \tag{3.10}$$

where P is the output power, A is the surface area of one disk unit in the TENG, U and I are the voltage and the current on the load with a certain resistance, respectively, and J is the current density. The power density was also plotted as a function of external resistance in Figure 3.19f. The output power density firstly increases at a low resistance region and then decreases at a higher resistance region. The maximum value of the power density of ~1 W/m^2 occurs at ~10 MΩ.

The disk TENG based on in-plane charge separation process has several advantages over the TENG based on vertical-to-plane charge separation process. Firstly, this novel working mode enables the energy harvesting from rotational motion, which largely broadens the range of applications of TENGs for a range of centric type of motion. Secondly, such continuous-motion-driven TENG generates the electricity with adjustable frequency and at high frequency, because it does not rely on the resilient bouncing of the TENG after mechanical triggering. This could help to realize a direct and continuous driving of electronic devices and fast charging of storage units. Thirdly, the in-plane charge separation does not require the presence of an air gap, making the TENG device more suitable for multi-layer integration and fully packaging. Last but not least, with the innovative design of device configuration, this is the first to realize the nanogenerator working at constant velocity of rotation, and a reliable self-powered angular speed sensor could be obtained.

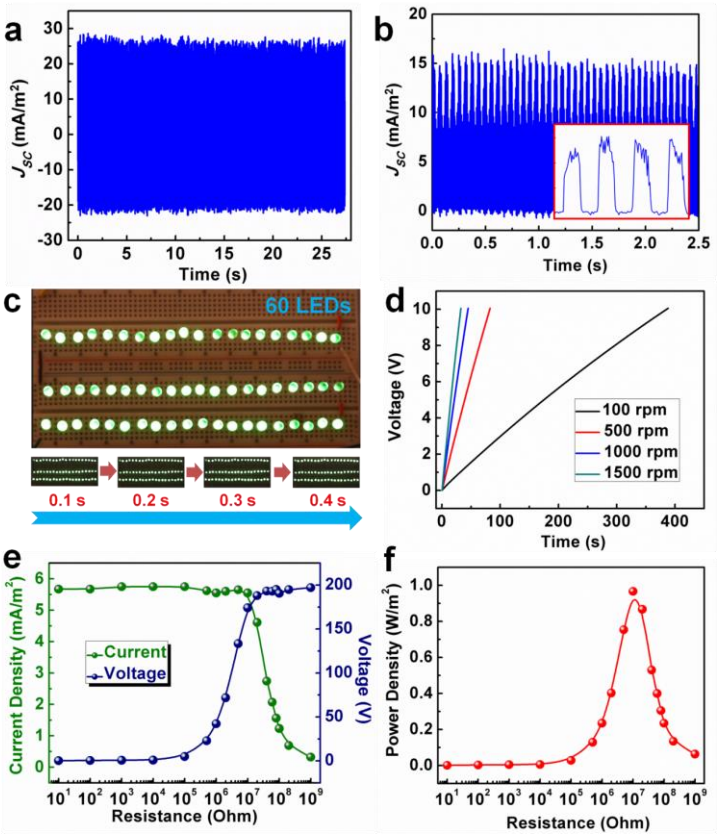

Figure 3.19 The disk TENG as a power source with high current output and frequency. (a) The measured output current for Configuration 3 at 1000 rpm. (b) The rectified output current for Configuration 3 at 1000 rpm. The inset is an enlarged view of the rectified output current with "square waveform" output profile. (c) Top: a snapshot showing the instantaneous and continuous powering of 60 green LEDs in series by the disk TENG working at 1000 rpm. Bottom: four consecutive frames captured from a video with the time interval of 0.1 s. (d) The measured voltage of a 22 μF capacitor charged by the disk-TENG at variable rotating speeds. (e) The relationship between the output voltage/current and the resistance of an external load. (f) The relationship between the effective power density and the resistance of the external load. The maximum power is received when the external resistance is 10 MΩ.[59]

In summary, we present a novel design of disk-shaped triboelectric nanogenerator based on in-plane charge separation mechanism, which can convert rotational mechanical energy into electricity. Finite element simulation was employed to gain a comprehensive understanding about the fundamental working principle as well as the output characteristics of the TENG, and the experimental results are in good agreement with the

theoretical predictions. Through experimental comparison, we find an enhancement of the output current from finer segmental patterns, which can serve as the guidance for future research on the disk TENG. A linear relationship is present between the current/frequency and the rotating speed, which enables its application as a self-powered angular speed sensor. The disk TENG makes it possible to harvest rotational mechanical energy at a high frequency with a high magnitude of power density, showing unprecedented superiority and practicability in both driving electronic devices directly and continuously as well as charging energy storage units. This work opens up a new field in mechanical energy harvesting, and pushes forward a significant step towards the practical application of nanogenerators by using rotary motion, such as the brake system in an automobile.

3.6 Robust and high-efficiency rolling triboelectric nanogenerator

Up to current stage, four different working modes of the TENGs have been developed to accommodate applications in various types of mechanical motions, including the contact mode, the sliding mode, the single-electrode mode, and the freestanding mode. However, as an energy harvesting approach, the energy conversion efficiency and device durability are still essential issues, which may be limited by the relatively large frictional resistive force between triboelectric surfaces during the operation of the TENG, especially for the working modes based on sliding electrification. To improve the efficiency of the TENG and the robustness of the surface for anti-wearing purpose, most of efforts have been focused on enhancing the output power through sophisticated structural designs or surface modification.

Here in this work, we designed a novel working mode of rolling triboelectric nanogenerators (RTENG) that can deliver ultrahigh energy conversion efficiency without scarifying its robustness and stability. For the first time, rolling electrification between cylinder-shaped steel rods and planar thin films of fluorinated ethylene propylene (FEP) was employed for converting the kinetic energy of rolling rods into electric power. The rolling triboelectric nanogenerator (RTENG) has a sandwiched structure composed of two FEP thin films and steel rods rolling between them. The rolling motion of the steel rods between the FEP thin films introduces triboelectric charges on both surfaces and led to the change of potential difference between each pair of electrodes on the back of the FEP layer, which drives the electrons flow in the external load. As power generators, each pair of output terminals can work independently that delivers an open-circuit voltage of 425 V, an instantaneous charge transfer of 0.145 μC, and a short-circuit current density of 5 mA/m^2. The two sets of output terminals can also be integrated to present an overall power density of up to 1.6 W/m^2. The impact of variable structural factors were investigated to achieve optimization of the output performance, such as the velocity of the rolling motion, the gap distance between adjacent electrodes, and the diameter of the steel rods. Owing to the low friction coefficient of the rolling movement, a high energy conversion efficiency of up to 55% has been demonstrated, with much smaller wearing of triboelectric surfaces as compared with sliding friction. Based on the basic concept of rolling electrification, many other prototypes of RTENGs have been successfully derived, like the rotating disk structure, the grating structure, and other structures based on rolling balls. This work demonstrates a new working mode of high-efficient and robust TENGs towards large scale energy harvesting.[83]

The device structure of the RTENG is schematically illustrated in Figure 3.20a, which is composed of a group of rolling steel rods sandwiched by two layers of FEP thin films. Each FEP thin film was deposited with two separated copper electrodes on its back side, respectively. Polymer nanowire structures were created on both inner surfaces of the FEP thin film through inductively coupled plasma (ICP) etching to enhance the tribo-charge density upon rolling electrification. During the operation of the RTENG, the bottom layer FEP film (BL-FEP) was securely attached onto a three-dimensional stage, and the top layer FEP film (TL-FEP) was driven by a linear motor to oscillate back and forth, which also initiated the rolling motion of the steel rods. As the TL-FEP moved from the left-hand end to the right-hand end of the BL-FEP, the steel rods would also move from the left-hand part to the right-hand part of the BL-FEP, until the TL-FEP stopped and started to move back. Figure 3.20b-e depicts the working principle of the RTENG based on a step-by-step analysis of the charge transfer process. As the steel rods gets contacted with the entire area of both FEP films, due to their different abilities in attracting electrons, there will be net negative charges on the inner surface of the FEP films, and net positive charges on the surface of the steel rods. By assuming even distribution of the negative charges on the FEP surface and the symmetric layout of the electrodes, the negative charges will not lead to electric output, and the potential difference between each pair of electrodes will only rely on the relative location of the positively-charged steel rods. Initially (Figure 3.20b), the positively-charged steel rods are located beneath the right-hand electrode (RE) of the TL-FEP, and over the left-hand electrode (LE) of the BL-FEP. Hence, for the top layer, the RE poses a higher electrical potential than the LE, leading to an instantaneous electrons flow from the LE to the RE to

reach an equilibrium state. The opposite potential polarity (the potential of the LE is higher than that of the RE) exists in the bottom layer. As the TL-FEP starts to slide towards the right-hand side along with the positively-charged steel rods, the potential difference between the RE and the LE on the top layer will be gradually reduced, until it reaches the equal potential condition in Figure 3.20c. As the TL-FEP continues moving forward, the electrical potential on the LE will be higher than that of the RE, and the potential difference will reach the maximum when the TL-FEP stops at the right-hand side of the BL-FEP (Figure 3.20d). In the next half cycle of rolling motion, the TL-FEP moves back from the right-hand side to the left-hand side, and the potential difference between the LE and the RE first drops to zero (Figure 3.20e) and then becomes negative until reaching the original position (Figure 3.20b). In this process, due to the moving of the positively-charged rolling rods in reference to the BL-FEP, the revolution of potential difference in the bottom pair of electrodes will follow a reverse trend as compared to the top layer. In terms of the short-circuit condition, the change of potential difference in the first half cycle of motion will lead to electrons flow from the RE to the LE in the top layer, and the electrons will flow back from the LE to the RE in the second half cycle. Similar to the revolution of potential difference, the short-circuit electrons flow follows an opposite direction in the bottom layer as compared to the top layer.

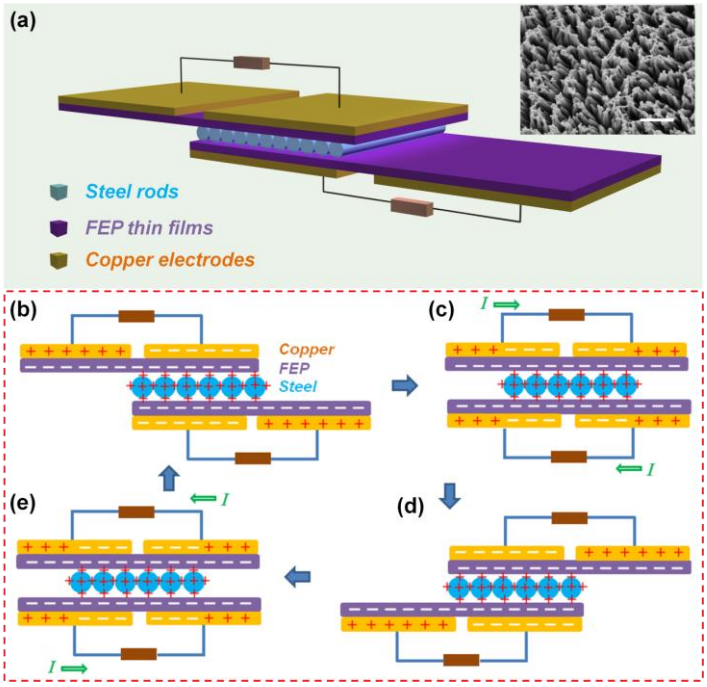

Figure 3.20 The structure and working principle of the rolling triboelectric nanogenerator. (a) Schematic illustration showing the device structure of the RTENG. Inset (top right): the scanning electron microscopy (SEM) image of the nanowire structure created on the inner surface of the FEP thin film. The scale bar is 1 μm. (b-e) A step-by-step illustration showing the working principle of the RTENG.[83]

To gain a more quantitative understanding about the working mechanism of the RTENG, finite element method (FEM) was utilized to calculate the open-circuit potential distribution between the two electrodes at different states of motion. In the established two dimensional model, a pair of FEP thin films with the length of 85 mm and with the thickness of 100 μm was selected, and each pair of copper electrodes on the back side of the FEP were separated with a 5 mm gap. Twenty steel rods with a diameter of 2 mm were sandwiched between the two FEP films, which were assigned with a triboelectric charge density of 60 $\mu C/m^2$. The reference state was selected as the condition that the electric potential was zero at infinity. The calculated potential distribution is shown in Figure 3.21a-d, which corresponds to the four different states in Figure 3.20b-e. From the

calculation results, it can be found that the revolution of potential distribution on both pairs of electrodes is consistent with what is proposed in the schematic working mechanism. Taking the electrodes on the top layer as an example, the potential on the RE is much higher than that on the LE at the first state when the steel rods are located beneath the RE of the top layer (Figure 3.21a). As the steel rods roll to the middle position between the LE and RE, an equal-potential state is achieved (Figure 3.21b). The potential difference between the RE and LE becomes negative when the rolling rods are located beneath the left-hand side of the top layer (Figure 3.21c). The other equal-potential state will be obtained when the top layer moves back and reaches the middle position of the two electrodes (Figure 3.21d), which is similar to the condition of Figure 3.21b. When it comes to the electrodes on the bottom layer, an opposite polarity but the same magnitude of potential difference can be calculated. The highest potential difference can reach up to 100 kV, which is a substantial driving force for the external charge flow.

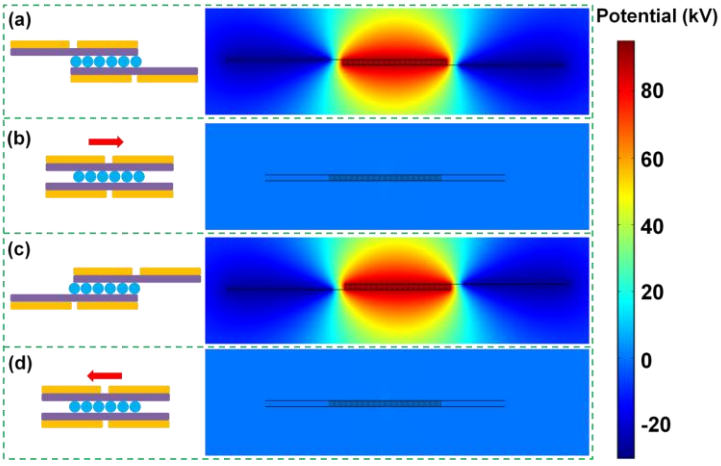

Figure 3.21 Numerical calculations of the potential distribution across the electrodes of the RTENG. (a) The calculated potential distribution when the rolling rods are on the left part of the bottom layer. (b) The calculated potential distribution when the rolling rods slide toward the right part of the bottom layer. (c) The calculated potential distribution when the rolling rods are on the right part of the bottom layer. (d) The calculated

potential distribution when the rolling rods slide back to the left part of the bottom layer.[83]

There are two sets of output terminals in the RTENG, and they can work well independently, as demonstrated in the output performance characterizations in Figure 3.22. The measurement results of the open-circuit voltage (V_{OC}), amount of transferred charges (Q), and short-circuit current density (J_{SC}) of the output terminals on the top layer were displayed in Figure 3.22a-c, respectively. It can be observed that despite the relatively low contact area between the rolling rods and the planar surface of the FEP film, the top layer of the RTENG can deliver high output performance as V_{OC} = 425 V, Q = 0.145 μC, and J_{SC} = 5 mA/m^2. Figure 3.22d-f shows the measured output performance from the output terminals of the bottom layer, and the results of similar magnitude could be obtained. For the measurement of the J_{SC}, it should be noted that both of the left electrodes were connected to the positive end of the measurement probe (Insets of Figure 3.22c and 3.22f), and the measurement results indicate reverse polarity, which is in consistency with the proposed direction of charge flow and further demonstrates the validity of the working principle. Furthermore, it seems that the output current of the bottom layer is a little more stable than that of the top layer, which might be owing to the fact that the bottom electrodes are stationary, while the top electrodes undergo reciprocating movement with the TL-FEP. The two sets of output terminals can be further integrated and rectified for higher output current and convenient applications, as shown in the schematic circuit diagram in Figure 3.22g, where the LE of the top layer and the RE of the bottom layer were connected, and vice versa. The integrated J_{SC} can reach up to 9-10 mA/m^2, which almost doubles the output current density from a single layer (Figure

3.22h). The output current was also measured with different resistances connected in the load, and an optimum output power density of ~ 1.6 W/m^2 was delivered (Figure 3.22i).

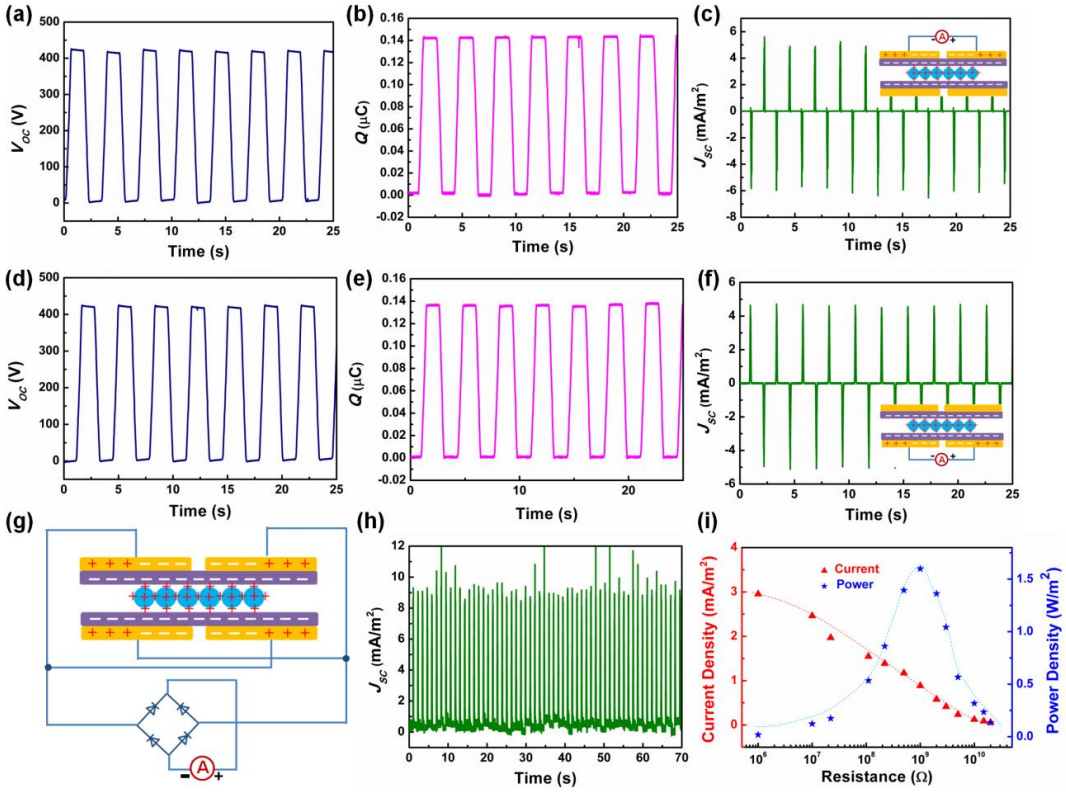

Figure 3.22 General output performance characterization of the RTENG. (a-c) The measurement results of the open-circuit voltage, amount of transferred charges, and short-circuit current density of the RTENG from the top output terminals, respectively. Inset of Figure (c): the connection polarity for the measurement of the short-circuit current. (d-f) The measurement results of the open-circuit voltage, amount of transferred charges, and short-circuit current density of the RTENG from the bottom output terminals, respectively. Inset of Figure (f): the connection polarity for the measurement of the short-circuit current. (g) A schematic showing the polarity of connection to integrate and rectify the output current from both the top and bottom output terminals. (h) The measured short-circuit current density after integration and rectification from the top and bottom output terminals. (i) The measured output current and output power with variable load resistances.

In order to achieve a comprehensive understanding about the working performance of the RTENG, the dependences of the output performance on various structural parameters were investigated, including the sliding velocity, the electrode

separation distance, and the diameter of the rolling rods, as shown in Figure 3.23. For convenience purpose, all of the measurements in this section were carried out on the bottom output terminals. First, with other parameters kept constant, the output performances with variable sliding velocities were measured (Figure 3.23a-b), and it can be found that while the V_{OC} remains unchanged with the sliding velocity, the J_{SC} is raised with increasing velocities from 0.1 to 0.5 m/s. The different trends can be attributed to the fact that the V_{OC} is a static signal that only depends on the amount of tribo-charges and the magnitude of the charge separation; on the other hand, the J_{SC} is a dynamic signal that is also highly proportional to the rate of the charge transfer process. Hence, the maximum output power also increases with the sliding velocity. Second, with the horizontal separation distance between two electrodes on each FEP thin film increasing from 1.6 to 25.4 mm, the V_{OC} shows a slight enhancement, but the J_{SC} decays drastically. Theoretically, the V_{OC} should have increased with the elevation of gap distance, since a larger distance between the two electrodes leads to a smaller capacitance, which is inversely proportional to the V_{OC} with constant amount of transferred charges; however, this increasing trend can hardly be recorded due to the non-ideal inner resistance of the voltage meter. The increase of the separation distance also results in longer time for the charge transfer process and hence lower J_{SC}, which is consistent with the measurement results. Based on these results, it is easy to understand that total power output declines with larger gap distance. Third, as displayed in Figure 3.23e-f, both the V_{OC} and J_{SC} decrease with the elevation of the diameter of the rolling rods. Assuming constant charge density on the steel rods with variable diameters, the surface charges on each single rod can be considered as equivalent charge centers at axial line of the cylinder structure.

Hence, as the diameter of the rolling rods grows larger, the distance between the charge center and the electrodes keeps increasing, which renders lower potential difference than that with the smaller rolling rods. All in all, combining the results demonstrated by Figure 3.23c-f, it can be concluded that lower rod size and gap distance are favorable for the overall output performance of the RTENG.

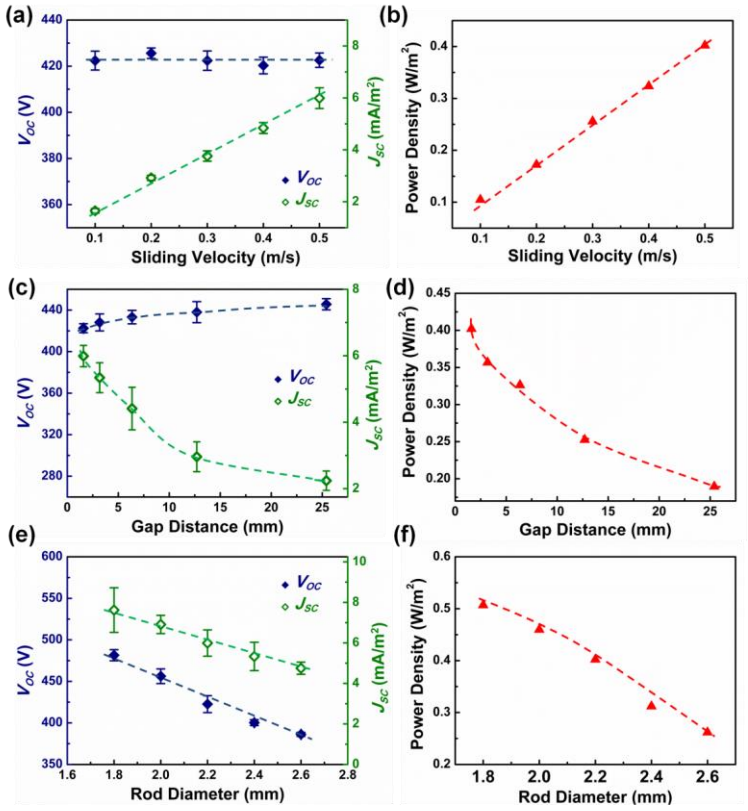

Figure 3.23 The dependences of the output performance of the RTENG on variable structural parameters. (a) The impact of the sliding velocity on the open-circuit voltage and the short-circuit current density of the RTENG. (b) The impact of the sliding velocity on the optimum output power density of the RTENG. (c) The impact of the gap distance between two electrodes on the same FEP thin film on the open-circuit voltage and the short-circuit current density of the RTENG. (d) The impact of the gap distance on the optimum output power density of the RTENG. (e) The impact of the rod diameter on the open-circuit voltage and the short-circuit current density of the RTENG. (f) The impact of the rod diameter on the optimum output power density of the RTENG.[83]

Rolling rods structure was utilized to minimize the frictional force in the power generator without scarifying the output power, and thus it may enhance the energy conversion efficiency. In this regard, the energy conversion efficiency was evaluated by measurement of the resistive force in both open-circuit condition and variable load resistances. It can be found that the resistive force became larger when load resistances were connected (Figure 3.24a), for the reason that the current flow or energy consumption in the load will yield higher electrostatic resistance to the rolling motion. Hence, by assuming constant frictional energy loss from heat dissipation, the energy conversion efficiency could be calculated by the amount of additional work done with external load divided by the total work through the following equation:

$$\eta = \frac{E_{output}}{E_{input}} = \frac{\int F dt - \int F_0 dt}{\int F dt} \tag{3.11}$$

Here, η is the energy conversion efficiency, E_{output} is the electrical energy output, E_{input} is the mechanical energy input, F is the resistive force measured with a certain load resistance, and F_0 is the resistive force measured with open-circuit condition. The calculation results are displayed in Figure 3.24b, indicating that the instantaneous efficiency can be up to 55% when the external resistance of the load is compatible with the internal impedance of the RTENG at current motion status. This energy conversion efficiency is different from the total energy conversion efficiency defined previously that accounts all of the electricity generated by the residual vibration of the device. The high energy conversion efficiency can be attributed to the low frictional coefficient between the rolling rods and the planar FEP surface, which is considered a unique advantage of this design. From the measurement of normalized friction coefficient (Figure 3.24c), it

can be found that the frictional coefficient of the rolling rod structure is substantially lower than that of the planar structures. This high-efficient RTENG could be employed for harvesting energy from gentle finger movement, which was then utilized for driving portable electronics, like light-emitting diodes (Figure 3.24d). Furthermore, the durability of the RTENG was verified by monitoring the surface morphology of the polymer nanowire structures over a long period of operations, as shown in Figure 3.24e. Two samples of the nanostructured FEP thin films were set up to undergo the rolling friction and sliding friction for 1000 cycles, respectively. The scanning electron microscopy (SEM) images of both samples were taken before and after the rolling or sliding frictions. It is clearly indicated that the sample applied with rolling friction had little degradation in the nanowire structures, while the most of the nanowires on the other sample enduring sliding friction were destroyed by the frictional force. With this comparison, the high durability of the RTENG was successfully demonstrated, which confirmed another unique advantage of the RTENG as compared to the traditional sliding TENGs.

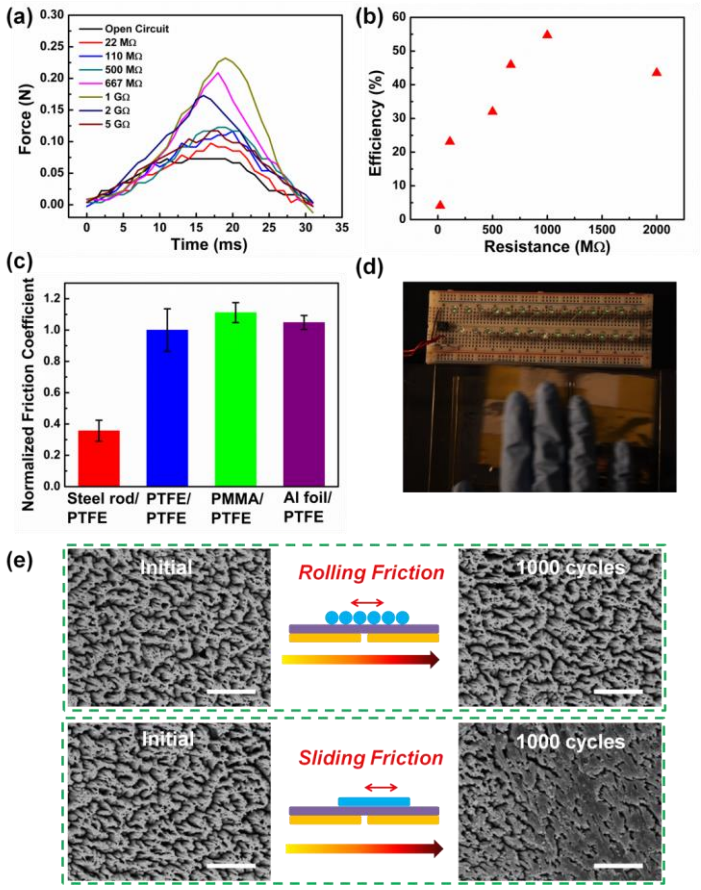

Figure 3.24 The characterization of the energy conversion efficiency of the RTENG. (a) The measurement of the resistive force during the energy conversion process of the RTENG with variable loading resistances. (b) The calculated energy conversion efficiency with variable load resistances. (c) The normalized friction coefficient between different types of materials customized for triboelectric nanogenerators. The friction coefficient between PTFE films were set as the reference value. (d) A capture of live demonstration indicating the instantaneous powering of portable electronics by the RTENG. (e) The comparison of the impact of surface morphology between rolling friction steel rods (top) and sliding friction by steel foils (bottom). The left two SEM images show the surface morphologies of the two samples before the friction and the right two SEM images show the surface morphologies after the friction, respectively. The scale bars are 2 μm for all the images.[83]

In addition to the basic structure of the above-mentioned RTENG, the concept of rolling electrification was further explored with other prototypes based on rolling balls, as presented in Figure 3.25. The first three configurations are basic structures employing the

rolling electrification between a group of rolling balls and planar thin films. Figure 3.25a shows the schematic structure of the first configuration. A group of dielectric PTFE balls are confined by an acrylic bracket, and they get negatively charged upon contact with the underlying copper electrodes. As the PTFE balls are allowed to freely roll between the pair of copper electrodes, which induces change of potential difference between the two electrodes and the charge flow in the external load. Figure 3.25b-c exhibits another two types of rolling-ball-based RTENG with similar working principle as described in Figure 6a. Specifically, the configuration in Figure 3.25b utilizes the rolling electrification between steel balls and planar FEP thin film, and the potential difference change will be induced on the pair of copper electrodes on back side of the FEP thin film. In Figure 3.25c, two separate sets of steel rods are directly connected with the underlying copper electrodes, and a freestanding FEP thin film will be rolling between the two groups of balls to generate electric power. The measured output performances of these three configurations are similar in profile and magnitude, but lower than that demonstrated in the rolling-rods-based structure. One possible reason might be the relatively lower contact area between the rolling balls and the planar films. To further enhance the performance of the rolling-ball-based TENG, two advanced designs were fulfilled including the linear-grating RTENG (Figure 3.25d) and the disk-rotation RTENG (Figure 3.25e). As revealed by Figure 3.25d, the steel balls are confined in several separate strips, and the concurrent movement of the rolling balls will introduce potential difference between the two sets of copper electrodes. With this configuration the output current is improved due to a larger rate of charge transfer, and more importantly, multiple cycles of charge transfer can be achieved through one single cycle of reciprocating movement. In

the disk-rotation RTENG as shown in Figure 3.25e, the rolling balls are confined in several parts of a disk-patterned acrylic bracket, and the underlying FEP thin film is deposited by complementary disk-patterned electrodes. This configuration was designed to accommodate the energy harvesting from rotating motions with tunable frequency, and the output current can be further employed for self-powered angular speed sensor based on the linear relationship between the magnitude of current output and the rotation speed.

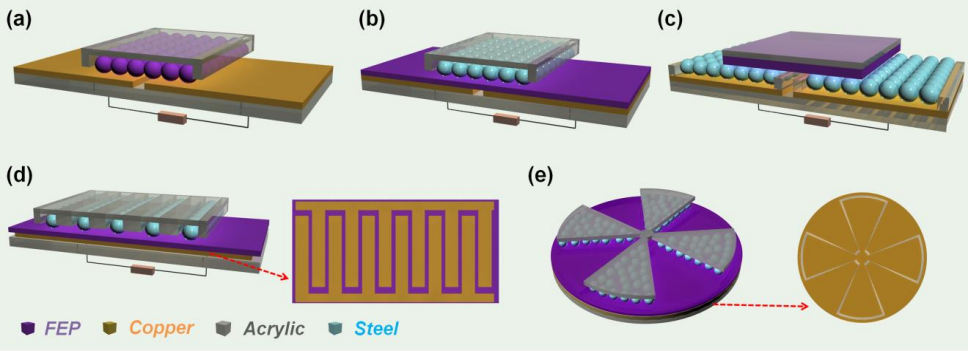

Figure 3.25 The schematic structure of the configurations of the rolling TENGs. (a) The schematic structure of the RTENG based on the rolling electrification between a group of PTFE balls and two separated copper electrodes. (b) The schematic structure of the RTENG based on the rolling electrification between a group of steel balls and a piece of FEP film deposited by two separated copper electrodes. (c) The schematic structure of the RTENG based on the rolling electrification between two groups of steel balls and a piece of freestanding FEP film. (d) The schematic structure of the RTENG based on the rolling electrification between several strips of steel balls and a piece of FEP film deposited by two sets of complementary grating copper electrodes. The inset is the detailed structure of the grating electrodes. (e) The schematic structure of the RTENG for rotational mechanical energy harvesting. This type of RTENG is composed of rolling balls distributed into four segments of a patterned disk structure, and a piece of disk-shaped FEP film deposited with two complementary copper electrodes, as shown in the inset image.[83]

To sum up, a high-efficient and robust approach for energy harvesting was demonstrated based on rolling electrification with much lower resistive force. Due to asymmetric screening of the triboelectric charges on the steel rods, a potential difference is induced between each two electrodes on the back of the FEP thin film, which is the

driving force for the external charge flow. Based on this basic working principle, a high output power of 1.6 W/m^2 and an excellent instantaneous energy conversion efficiency of up to 55% were demonstrated, due to very low frictional energy loss during the operation of the RTENG. The durability of the device was verified through tracking the surface morphology by SEM, indicating tremendously low wearing of materials. A comprehensive investigation was conducted to figure out the parameter effects on the output power of the rolling nanogenerator. Various other prototypes based on rolling spheres and different structural designs were also successfully fabricated to convey the basic concept of rolling electrification for effective and efficient energy harvesting. This work presents a new mode of triboelectric nanogenerator and brings up the development of this energy technology into a new horizon.

3.7 Stretchable triboelectric nanogenerators

Flexible and stretchable electronics have attracted long-lasting attentions for their promising applications in next-generation functional devices, including flexible circuitries, stretchable displays, stretchable sensors, epidermal electronics, and implantable devices. This new class of electronics allows devices to be deformed into complex shapes while maintaining the device performance and reliability. However, a sustainable power source is highly desired to drive those electronic devices, and the implementation of traditional power supply remains a challenge due to inconvenient operations and indispensable wire connections. In this regard, a more efficient way is to integrate a power generator to scavenge the ambient energy, especially for the mechanical energy from stretching motions. Attempts have been made to develop flexible

and stretchable power generators, but their output performances still need further enhancement for practical applications. In this work, we developed a new type of stretchable TENG (STENG), which was fabricated by assembling serpentine-patterned electrodes and a wavy-structured Kapton film. Owing to the unique structural design, the STENG could be operated at both compressive and stretching mode. At the traditional compressive mode, a high output power density of 5 W m^{-2} was delivered at a load resistance of 44 MΩ. At the stretching mode, the STENG was capable of withstanding a tensile strain of up to 22% and its output performance was up to 70 times larger than that of the planar TENG in the control experiment. Moreover, the STENG was able to provide reliable output performance on curved surfaces (with curvatures of up to 36 cm^{-1}). This research presents an unprecedented advancement in energy harvesting and self-powered sensors, and paves the way for the next-generation stretchable electronics and bio-integrated systems.[84]

The device structure and fabrication process flow of the STENGs are schematically illustrated in Figure 3.26a. The STENG is composed of a wavy-structured Kapton thin film sandwiched by two layers of serpentine copper electrodes deposited on stretchable polydimethylsiloxane (PDMS) substrates. First, the super high stretchability of the PDMS substrates was achieved by mixing the elastomer base and curing agent at a 30:1 ratio, by which an optimized stability of the deposited electrode was achieved. Then, serpentine copper electrodes were deposited on the PDMS membranes by a two-step sputtering approach. It has been well-recognized that the serpentine patterns can provide extraordinary stability to metal electrodes even under tensile strain. In this work, the unique advantage of the serpentine electrode was successfully verified by a controlled

experiment, in which the conductivities of both linear and serpentine electrodes were monitored upon a series of tensile strains, and the resistance of the serpentine electrode was much lower and more stable than that of the linear electrode, especially under high tensile strains. Finally, a wavy-structured Kapton film was fabricated by a high-temperature annealing process and inserted between the two layers of electrodes. It can serve as both the triboelectric material and the spacer layer based on its reversible elastic deformation upon compressing or stretching. Nanowire structures were introduced on both surfaces of the wavy-structured Kapton film by the inductively-coupled plasmon (ICP) etching process to enhance the triboelectric effect and the effective contact area with the electrodes, as shown in the scanning electron microscopy (SEM) images in Figure 3.26b. The photographs in Figure 1c and d show the morphology of the serpentine electrode and the wavy-structured Kapton film, respectively. It was clearly observed that the STENG could be conformably attached onto human skin, and the spacing of the STENG was attributed to the wavy-structured Kapton film. The device area of the obtained STENG is approximate 40 cm^2, with 7.5 cm in length and 5 cm in width.

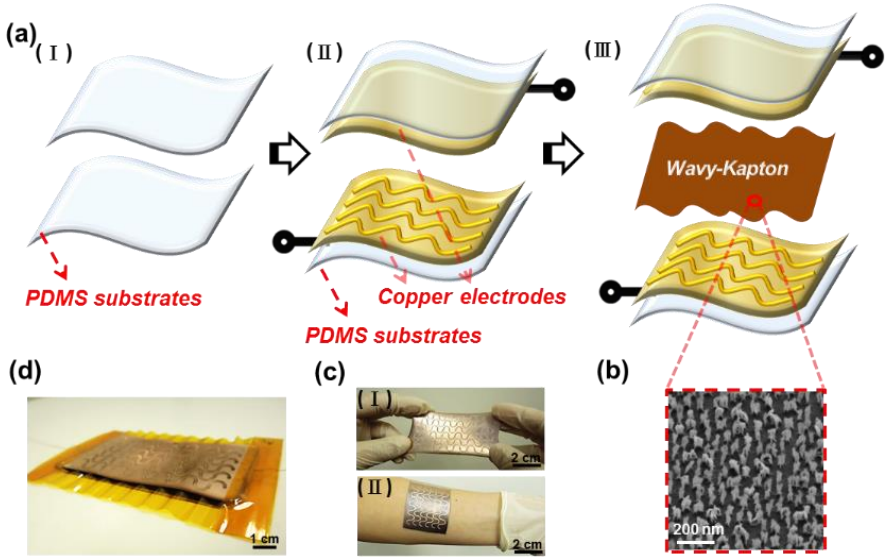

Figure 3.26 Structure and photographs of the STENGs (a) Schematic fabrication process flow and device structure of the wavy-STENG. (b) SEM image of nanowire structures on the surface of the Kapton thin film. (c) Photographs of the serpentine-patterned electrodes on the human skin and under stretching condition. (d) Photograph of the fully-assembled wavy-STENG.[84]

Figure 3.27 illustrates the working principles of the STENG, which is based on the parallel integration of two single-electrode TENGs with synchronized operations. Owing to the unique structural design, the STENG is capable of working at both the compressive mode (Figure 3.27a) and the stretching mode (Figure 3.27b). As shown in Figure 3.27a, at the initial state, top and bottom electrodes are separated owing to the stiffness of the wavy-structured Kapton thin film and there is no electric output (I). By applying a vertical compressive force on the STENG, the copper electrodes and the Kapton thin film are brought into fully contact, leading to contact electrification between the electrode surface and the Kapton surface (II). Due to their different surface affinities, the electrons will be transferred from the surface of the electrodes to the surface of Kapton, leaving net negative charges on the Kapton surface and net positive charges on the electrode surface. As the compressive force is releasing, the tribo-charged surfaces get separated owing to the elastic resilience of the wavy-structured Kapton film. The separation of charges will induce potential difference between both electrodes and the ground in the open-circuit condition, which will drive the electrons flowing from the ground to the electrodes in the short-circuit condition. When the compressive force is fully released and the device recovers to its original shape (IV), the open-circuit potential difference will reach its maximum value, since the largest distance between the tribo-charged layers is achieved. Once the STENG is pressed again (V), the potential difference will start to drop in the open-circuit condition, and the electrons will flow back

to the ground in the short-circuit condition until it reaches the fully contact condition (II). Hence, with a periodic compressive force applied onto the STENG, a cyclic AC output current will be generated across the load between the electrodes and the ground. In conventional designs of the TENGs with vertical contact-separation working mode, an additional spacer was usually indispensable for the charge separation process; while the wave-structured Kapton thin film can serve as both the triboelectric layer for charge generation and the spacer for charge separation, which greatly simplifies the device structure and improves its flexibility.

In the stretching mode, the working principle is quite similar to that of the compressive mode, despite that the direction of the applied force is aligned with the parallel direction of the STENG. The STENG is first stretched to the maximum length, and the wavy-structured Kapton thin film will be elongated to flat structure and gets into fully contact with the two electrode layers. Similarly, positive and negative charges will be generated on the surface of the electrode and the Kapton film, respectively, due to the contact electrification between them (II). In the next three steps, the stretching force is first released and then applied again, which will lead to the shrinkage and elongation of the device back and forth. Under the circumstances, the separation distance between the electrode layers and the Kapton film changes in the same manner as that in Figure 3.27a, which will introduce a similarly cyclic process of the open-circuit potential difference and short-circuit charge transfer between the electrodes and the ground (III to V).

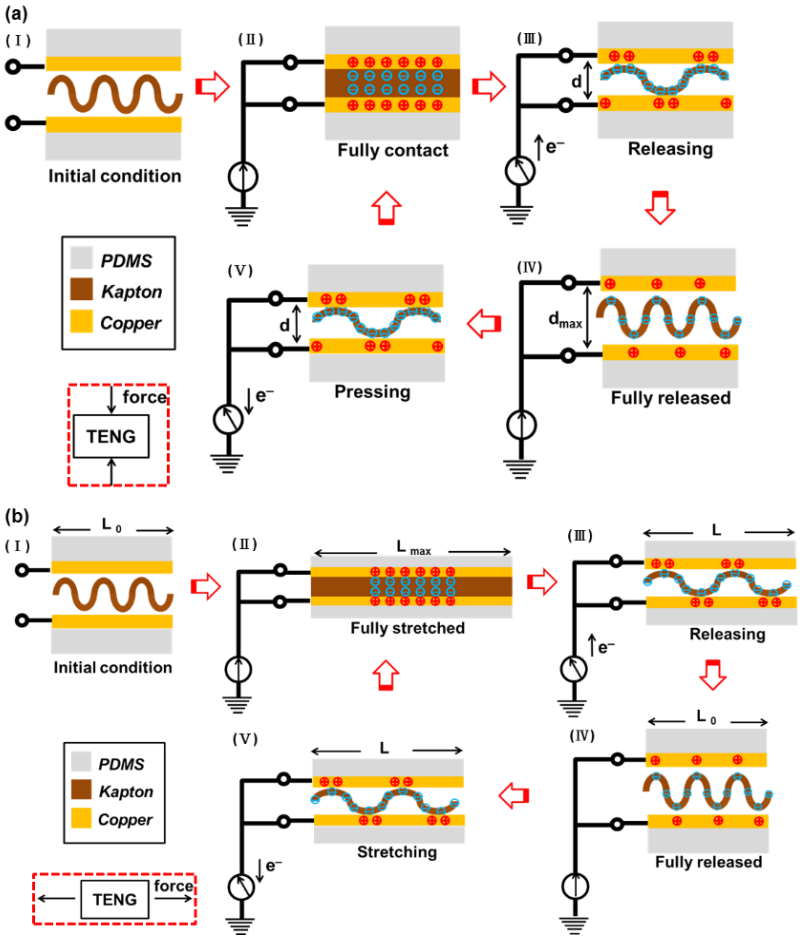

Figure 3.27 Working principles of the wavy-STENG. (a) Cross-sectional schematics illustrating the power generation process of the wavy-STENG under a cyclic compressive force. (I) Initial state with no force applied; (II) A compressive force has been fully loaded onto the STENG to bring the wavy-structured Kapton thin film and copper electrodes into complete contact; (III) The releasing of the compressive force, leading to the separation of the tribo-charged layers; (IV) The compressive force has been fully released, with the maximum separation distance between the tribo-charged layers; (V) The compressive force is being loaded for the next cycle. The insets show figure legends and the direction of the applied force. (b) Cross-sectional schematics illustrating the power generation process of the wavy-STENG under a cyclic stretching force. (I) Initial state with no force applied; (II) A stretching force has been fully loaded onto the STENG to bring the wavy-structured Kapton thin film and copper electrodes into complete stretched condition; (III) The releasing of the stretching force, leading to the separation of the tribo-charged layers; (IV) The stretching force has been fully released, with the maximum separation distance between the tribo-charged layers; (V) The stretching force is being loaded for the next cycle.[84]

The typical output performance of the STENG was first investigated on the compressive mode, as shown in Figure 3.28. To demonstrate the significance of the wavy-structured Kapton film, control measurements were carried out on the TENG with the same materials but a planar Kapton film. In the following discussion, the STENGs composed of a planar and wavy-structured Katpon films are denoted as the planar-TENG and wavy-STENG, respectively. Figure 3.28a-c displays the open-circuit voltage (V_{OC}), the amount of transferred charges (Q_{tr}), and the short-circuit current (I_{SC}) of the planar-TENG and wavy-STENG. It can be observed that the obtained V_{OC}, Q_{tr}, and I_{SC} are approximate 700 V, 160 nC, and 75 μA for the wavy-STENG, which are up to 70 times larger than those of the planar-TENG. The significant difference of the output performance could be attributed to the function of the wavy-structured Kapton film as an effective spacer, by which a much larger separation distance is guaranteed. In addition, the triggering frequency is another important factor that can significantly affect the TENG's output. The I_{SC} of the wavy-STENG under compressive force with different frequencies was measured, as shown in Figure 3.28d. As the frequency increases from 3 Hz to 10 Hz, the I_{SC} increases from 50 to 85 μA due to the elevation of the deformation rate and thus higher speed of the charge transfer process. The relationship between the output power density and the resistance was plotted in Figure 3.28e, and a high output power density of 5 W m^{-2} could be achieved for the wavy-STENG at a load resistance of 44 MΩ, which is much higher than that of the planar-TENG (0.06 W m^{-2} at 176 MΩ). An instantaneous energy conversion efficiency of up to 15% can be achieved at this condition. Moreover, the relatively smaller optimum resistance of the wavy-STENG is another advantage in the impedance match for the practical applications of the STENGs.

With such a high output power, the wavy-STENG was able to instantaneously power up serially-connected light-emitting diodes (LEDs) driven by gentle finger tapping (Figure 3.28f).

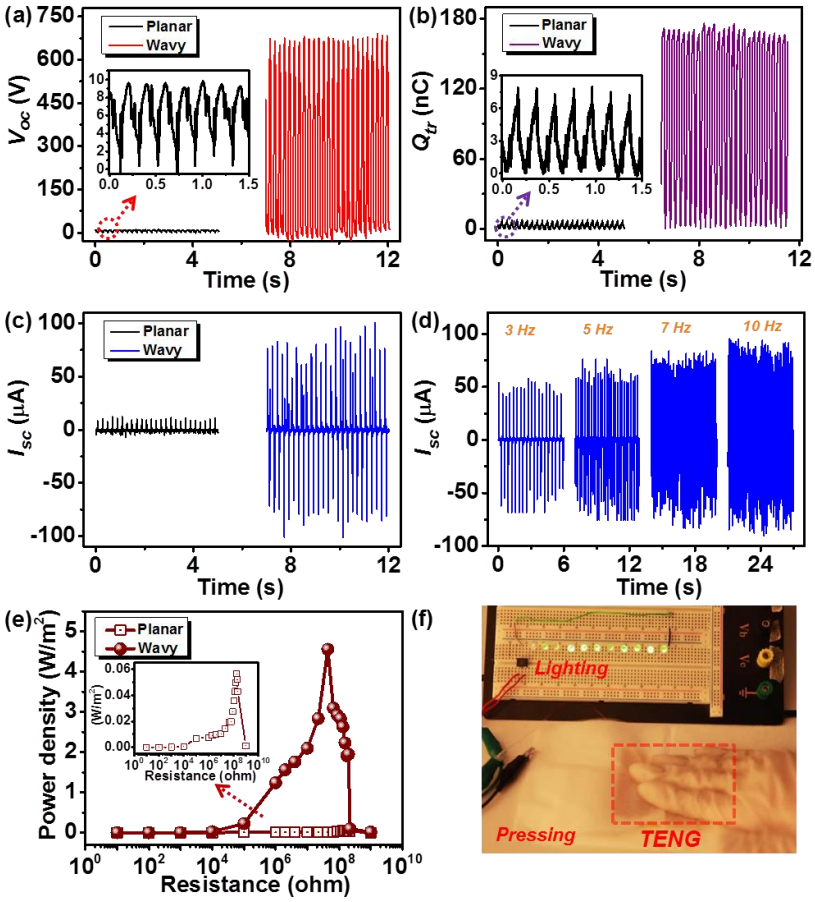

Figure 3.28 The output performance of the STENG at compressive mode. (a) The open-circuit voltage (V_{OC}) of the planar-TENG and the wavy-STENG. (b) The transferred charge quantity (Q_{tr}) of the planar-TENG and the wavy-STENG. The inset is an enlarged view of the Q_{tr} in the planar-TENG. (c) The short-circuit current (I_{SC}) of the planar-TENG and the wavy-STENG. The inset is an enlarged view of the I_{SC} of the planar-TENG. (d) Frequency responses of the I_{sc} in the wavy-STENG measured from 3 Hz to 10 Hz. (e) Relationship between instantaneous power density and the resistance of the external load for the planar-TENG and the wavy-STENG. The maximum power density can reach approximate 5 W/m^2 when the external load is 44 MΩ. (f) A photograph showing that 10 commercial green LEDs were directly driven by the wavy-STENG.[84]

The unique characteristic of the STENG in this work is to harvest energy from a stretching motion, and the output performance of the STENG was evaluated by a cyclic stretching force through a linear motor. Again, the performance of the planar-TENG was also measured as a control group. Representative data of the output performance with various tensile strains were recorded for both the planar-TENG and wavy-STENG in Figure 3.29a-c. It can be found that the V_{OC}, Q_{tr}, and I_{SC} of the wavy-STENG are monotonically increased with the applied tensile strain of up to 22% (at a maximum operation speed of 0.1 m s^{-1}). The maximum values of the V_{OC}, Q_{tr}, and I_{SC} obtained at 22% are 1.3 V, 0.6 nC, and 53 nA, respectively. Conversely, the output performances of the planar-TENG are relatively small and notably decreased after the tensile strain reaches 10%, which can be attributed to the limited spacing between the copper electrodes and planar Kapton thin film. Moreover, after the tensile strain reaches 15%, the largest difference in electric output performance between the planar-TENG and wavy-STENG can be perceived. From the above-mentioned results, it can be concluded that the wavy-structured Katpon film serves as a reliable spacer to maintain the electric output of the STENG under high tensile strains. Meanwhile, the stability test was carried out by continuously stretching the wavy-STENG at a speed of 0.1 m s^{-1}, as shown in Figure 3.29d. After 3600 stretching cycles, the output current density (J_{SC}) exhibits only negligible drops indicating the high durability of the wavy-STENG.

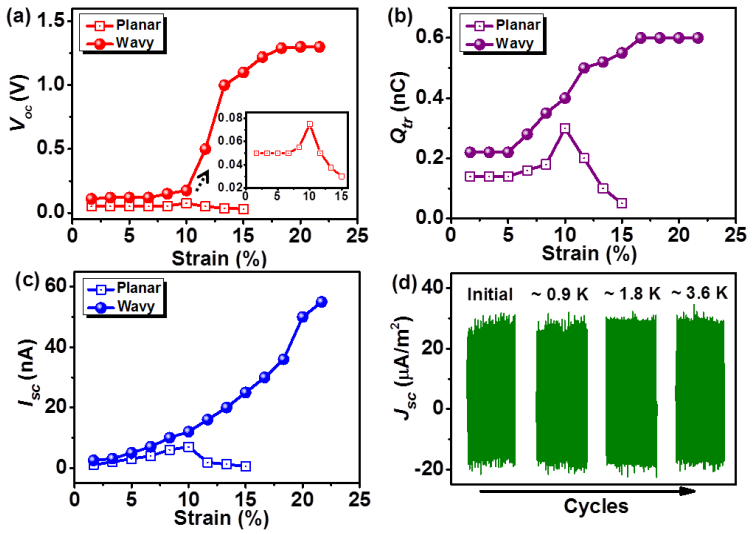

Figure 3.19 The output performance of the STENG at stretching mode**.** (a) The V_{OC} of the planar-TENG and wavy-STENG under various tensile strains. The inset image shows the enlarged view of V_{OC} of the planar-TENG. (b) The Q_{tr} and (c) the I_{SC} of the planar-TENG and the wavy-STENG under various tensile strains. (d) The measured results of the J_{SC} after the wavy-STENG has been continuously operated for 900, 1800, and 3600 cycles.[84]

Another substantial advantage of the wavy-STENG is its compatibility to work on curved surfaces and adaptability to effectively harvest energy as a bendable power source. To verify this superiority, the output performances of the wavy-STENG were measured at compressive mode on surfaces with different curvatures (from 12 cm^{-1} to 36 cm^{-1}), as displayed in Figure 3.30. As can be observed in Figure 3.30a-c, the output performances of the wavy-STENG reveal a great consistency on surfaces with different curvatures, indicating its good versatility to work on non-ideal surface conditions. For example, the wavy-STENG can be attached on human skins or joints for scavenging energy from human body motions as well as biomedical monitoring, which will be discussed later.

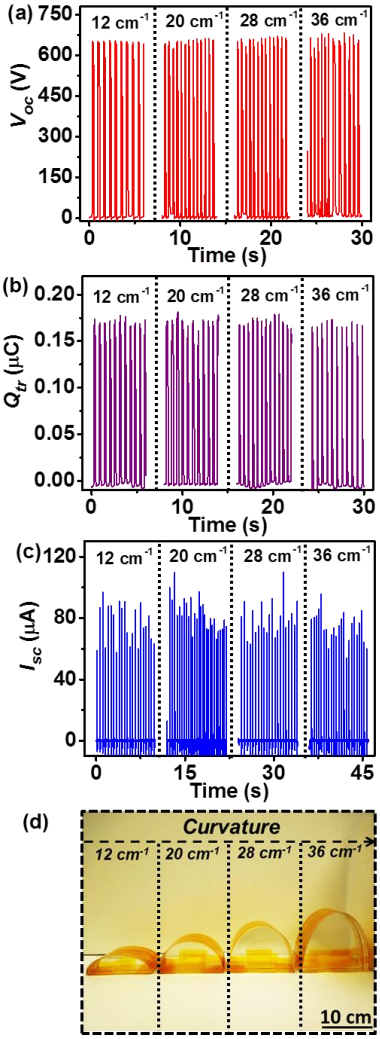

Figure 3.30 The output performance of the FTENG on curved surfaces**.** (a) The V_{OC}, (b) The Q_{tr} and (c) the I_{SC} of the wavy-FTENG on the surfaces with different curvatures, respectively. (d) The corresponding acrylic molds with different curvatures ranged from 12 cm^{-1} to 36 cm^{-1}.[84]

In summary, a flexible triboelectric nanogenerator has been developed for energy harvesting from various types of mechanical motions and self-powered body motion sensing. The high stretchability of the STENG is owing to the advanced structural designs including the wavy-structured Kapton film and the serpentine electrodes on elastic PDMS substrates. The STENG can be operated at both compressive and stretching

mode, and delivers an open-circuit voltage of 700 V and a short-circuit current of 75 μA, corresponding to an instantaneous output power density of 5 W m^{-2}. The wavy-STENG has presented several advantages as compared to its planar counterpart, such as much higher output performance, the capability of withstanding a tensile strain of up to 22%, and the high stability to work on curved surfaces. This work brings up new insights into further development of stretchable TENGs and their biomedical applications, which sheds light on advancements in electronic skins, epidermal electronics, and human-machine interfaces.

CHAPTER 4

APPLICATIONS OF NANOGENERATORS FOR SELF-POWERED SYSTEM

The ultimate goal of developing nanogenerators is to use it for powering electronic devices, or even for large scale power supply.[85-87] Hence, demonstration of its applications is an indispensable part towards a commercialized product. In my research, a few important demonstrations have been realized for the first time, including the direct powering of LEDs by a triboelectric nanogenerator, the sustainable charging of a cell phone battery, etc. In this chapter, the concept of "self-powered system" will be presented as live demonstrations that indicate a system can be integrated by a nanogenerator, an energy storage unit (if necessary), and electronic devices with various functions.

4.1 Piezoelectric nanogenerator for powering an electronic watch

As discussed in Chapter 2, the highest output performance I could achieve in piezoelectric nanogenerator is 20V and 6 μA, respectively. Such output current may be still low to directly power up electronic devices that require a certain level of current flow (except liquid crystal display). In order to drive commercial consumer electronics, one of the problems must be solved is convert the NG's AC signal into a regulated voltage with a constant current injection. To address this issue, a commercial buck convertor board (LTC3588-1, Linear Technology) was used, which integrates a low-loss full-wave bridge rectifier, capacitors for energy storage, and a high efficiency buck converter. The voltage

output after regulation is 1.8 V. The AC signals will first rectified by the full-wave bridge and the charges will be stored in the capacitor. After the energy harvested for 1000 strain cycles of the NG (around 20 minutes), an electronic watch was powered to working for more than 1 minute (Figure 4.1).

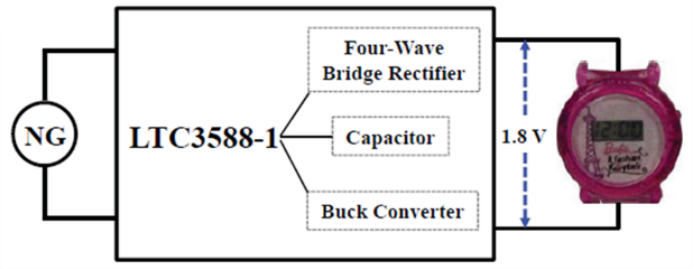

Figure 4.1 A demonstration showing that the harvested energy of the enhanced nanogenerator could be utilized for powering an electronic watch.[37]

4.2 Triboelectric nanogenerators for instantaneously powering light-emitting diodes

A light-emitting diode is a device that requires a certain level of applied voltage (more than 2 or 3 V) and current (up to 20 mA). In this work, the arch-shaped contact-mode TENG was employed to continuously power up LEDs driven by finger tapping. The real-time current signals flowing through the LED is given in Figure 4.2a. In comparison with the characteristic I-V curve of the LED, the peak current of 100 μA is way sufficient to turn the LED on. Figure 4.2b shows snapshots taken from a flashing LED. Each instant of lighting-up corresponds to a large peak of the output current. In coordination with the TENG's output characteristics discussed above, the resistance of the LED in "on" state is only about 23 kΩ, far below the range (1 MΩ to 100 MΩ) of rapid change of the current, so the current is almost the same as I_{SC}, but the voltage on the LED is only ~2.5 V. From Figure 4b, because the resistance of such a single LED is far

below the maximum power point, TENG can also drive the flashing of up to 50 LEDs connected in series, which only results in less than 5% decrease of the current. This demonstration clearly illustrates the ability of the TENG as a direct power source to continuously drive regular electronic devices. In the work of rotary disk TENG, the serially-connected LEDs can even be continuously powered up, owing to the high frequency of rotating motion and thus high output frequency from the disk TENG.

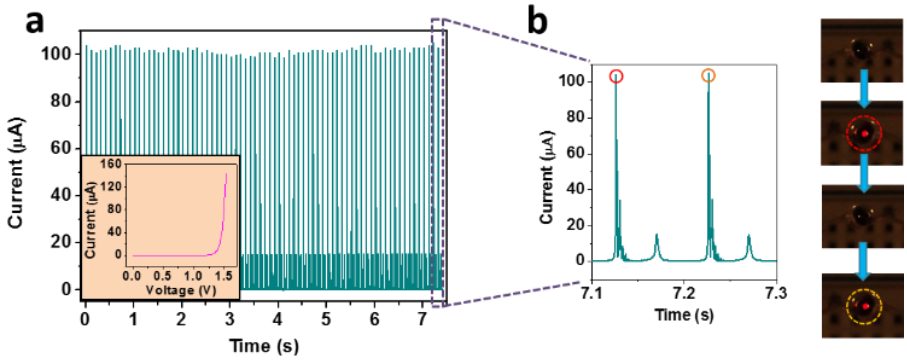

Figure 4.2 (a) The current through a LED driven by a rectified TENG under 8 Hz. The inset is the characteristic I-V curve of the LED. (b) The snapshots of the TENG-driven flashing LED, corresponding to the magnified current peaks.[81]

4.3 Integration of triboelectric nanogenerators and lithium-ion batteries for powering portable electronics

In many cases, the AC pulses from the nanogenerators may not directly satisfy the need of some electronic devices/systems, either because of the requirement for a constant DC current, or the higher power consumption than that generated by a single device. Thus, the output power needs to be regulated with an energy storage unit and a rectifier. As for the energy storage device, lithium ion batteries (LIBs) are the most widely used and promising choice. As the output (especially the current) from the arch-shaped TENG has reached the level to match the capacity of a LIB and overcome the self-discharge

current, it will be feasible to use a TENG to charge a LIB. The electrical circuit of such a power source module is shown in Figure 4.3a. At the standby mode, the LIB is continuously charged by a TENG through a rectifier and is disconnected from the load (switch S1 on; S2 off). When enough charges have been stored, the module will move on to the active mode, in which the battery will be disconnected from the TENG charger (S1 off) and start to power the system (S2 on). Such power source module is demonstrated using a home-made LIB, with $LiCoO_2$ as the cathode and graphite as the anode, with the same structure as commercial LIBs. In the standby mode, such a battery was fully charged by a TENG in 12.8 hours, with the battery voltage increased from 2.5 V to 4.2 V (Figure 4.3b), which is the standard charging window for a commercial LIB of this type. This is the first time a LIB is fully charged by a nanogenerator! Then in the "active mode", it can run for 5.2 hours with a constant discharge current at 2 μA, corresponding to a total capacity of 10.4 μAh.

Such an operation model of switching between the two modes is suitable for a lot of applications, such as wireless sensor network systems that have a long standby mode and a short active mode. If each module can be driven by an independent power source composed of a TENG and a LIB, the operation of the wireless sensor network could be maintenance-free. We demonstrated the powering of a wireless wind and humidex thermometer (Figure 4.3c), which consists of two parts—an outdoor remote sensor panel to measure the temperature, humidity and the wind speed, as well as to transmit the data back to the indoor receiver; a display panel with a data receiver, a data processing unit and an integrated temperature sensor. We use two TENG charged batteries (with charging curves similar as that in Figure 4.3b) to power these two components (located

~10 m apart) respectively, and a self-powered wireless sensor network system is realized. This type of power source module could solve two vital limitations for a battery: (1) the periodical replacement of a drained battery; (2) the relatively big size and weight of the battery to ensure a longer life operation. Thus, this will realize the miniature of a battery or extend its lifetime, especially for nanosystems, because they can be charged up at any time. The TENG can also be used together with a capacitor, in the case of fast charging and discharging, since it can charge a 47 μF capacitor to 10 V in 8 min.

Another huge application of the combination of nanogenerator with battery could be in people's daily life, to power personal electronics. With the greatly enhanced output from a 9 cm^2 size single-layer arch-shaped TENG, we successfully used it to charge a commercial cell phone battery (which was completed drained). Then, it could drive a cell phone up again including making a phone call (Figure 4.3d). Since the current of the TENG should be proportional to its area, if the TENG is scaled up in 3-dimensions, the charging rate could be tens of times higher, which is very feasible to fully charge a cell phone battery.

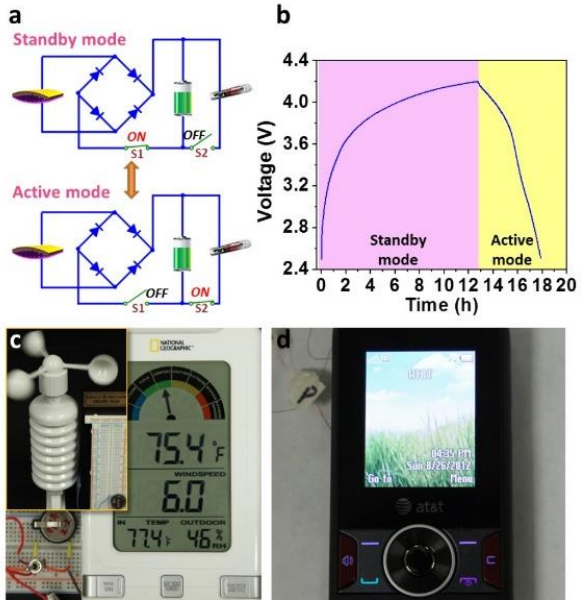

Figure 4.3 The power source module composed of an arch-shaped TENG and a lithium ion battery for driving a portable electronics that needs a regulated input power. (a) The schematic circuit diagram showing the switching between the "standby mode" and the "active mode" of the power source module. (b) The voltage curve showing the entire cycle of a lithium ion battery fully charged by TENG (standby mode) the subsequent constant current discharge at 2 μA (active mode). (c) A wireless wind and humidex thermometer, as an example of a whole wireless sensor network system, is driven by two such power source systems (one for the remote sensor module and one for the receiver-display module). (d) A commercial cell phone powered by its original battery that was charged by the TENG.[81]

4.4 Triboelectric-nanogenerator-driven electrochromic device for self-powered smart window

Electrochromic devices (ECDs) are developed to provide reversible changes of their optical properties via the electrochemical redox reactions corresponding to an external electric field, which are widely applied in displays, switchable mirrors, and electronic papers. Specifically, some types of ECDs with non-volatile memory effect make them ideal candidates for energy-saving smart windows on infrastructures and automobiles, since this type of ECD can maintain at a certain coloring state with no additional power supply. In this regard, the ECD can be integrated with a TENG as the power source instead of using batteries to provide a constant voltage across the device as a self-powered smart window system. Although the concept of "self-powered electrochromic window" can also be realized by integrated with solar cells as the power sources to drive the electrochromic device. However, unavoidable drawbacks, such as some part of ECD's surface area will be covered or sacrificed by solar cells or the transparency of integrated device will be reduced since most of solar cells are not fully transparent, which may limit its practical applications. Here, we proposed a new structure of self-powered electrochromic window, which is composed of the transparent TENG to

harvest natural mechanical energies to drive the ECD, and can completely solve the problems as mentioned above.

Here in this work, we established a fully-integrated self-powered smart window composed of a dual-mode TENG and an ECD. The entire device was a transparent, multi-layered structure, which was compatible with the smart window structure. The ECD was composed of Prussian blue (PB) nanoparticles and zinc hexacyanoferrate (ZnHCF) nanocubes as the electrochromic material and the ion storage layer, respectively. By operating with conventional electrochemical workstation, the maximum reversible change in transmittance (ΔT) of 32.6% could be achieved with respect to an external DC voltage. The TENG consisted of a multi-layered structure with micro-patterned polydimethylsiloxane (PDMS) thin films and transparent electrodes, which could be employed for harvesting the kinetic energy from wind impact and water droplet, with an optimized output power of 130 mW/m^2. By assembling the two devices on the same substrate, the self-powered smart window system was successfully realized with a transmittance change of up to 32.4% with visualized color variations as well, which could compete with the results demonstrated by the electrochemical workstation. This work sheds light on motion-driven electrochemical reactions and paves the way for a promising applications of the TENGs, which will push forward the development of self-powered systems.[88]

The multi-layer structure of the self-powered smart window is schematically illustrated in Figure 4.4a. On the top is a single-electrode TENG for scavenging the rain-drop kinetic energy that is composed of a PDMS thin film attached on a conducting substrate. A micro-patterned pyramid array structure (Figure 4.4b) was created on the

surface of the PDMS thin film through photolithography and template molding process, which plays an important role in improving the hydrophobic property and effective contact area of the surface, both aiming at enhancing the output performance of the single-electrode TENG. Other types of nanostructures, such as nanodots, nanogrates, nanomeches, can also provide a similar function to enhance its performance. With similar material system, a contact-mode TENG assembled by elastic springs was implemented right beneath the above-mentioned single-electrode-mode TENG. This structure was excellent in energy harvesting from wind impact, since the low-elastic-modulus springs could buffer the wind impact was on, and brought the device back to the original shape when the wind stopped. Both the TENGs were stacked on the ECD with a common Acrylic substrate to form a fully-integrated self-powered system.

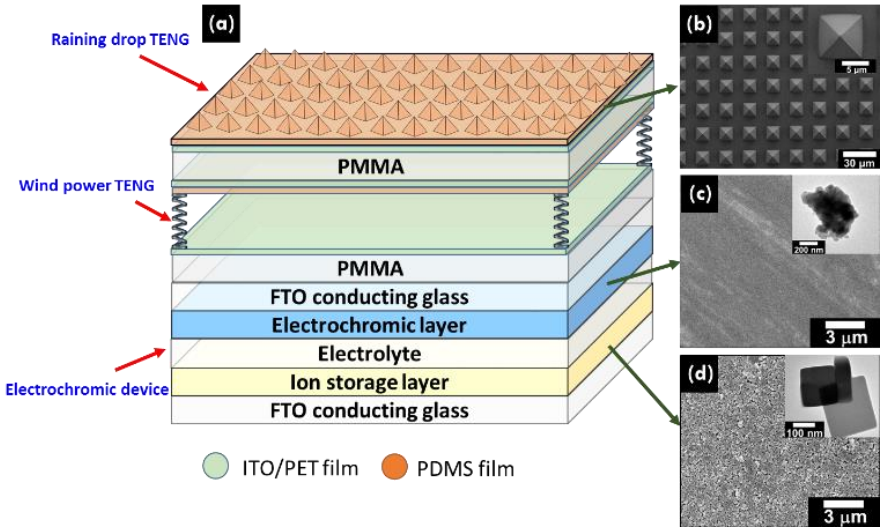

Figure 4.4 (a) Schematic diagram of the detailed structure for the self-powered smart window integrated with a raining drop-TENG, a wind powered-TENG, and an ECD from top to bottom; SEM images of (b) the PDMS film with a well-organized micro-pyramid array structure, (c) the PB and (d) the ZnHCF films; TEM images of PB nanoparticles and ZnHCF nanocubes are also presented as the insets.[88]

For the ECD, water-dispersible PB nanoparticles and ZnHCF nanocubes were synthesized as the electrochromic and ion storage materials, respectively. The phase compositions of the as-synthesized powders were confirmed by X-ray diffraction, and the peaks for each of the XRD patterns can be assigned to $Fe_4[Fe(CN)_6]_3 \cdot xH_2O$ (JCPDS, PDF No.73-0687) and $Zn_3[Fe(CN)_6]_2$ (JCPDS, PDF no.38-0688), suggesting that both compounds were successfully synthesized and the residual reagents were completely removed. Uniform PB and ZnHCF films were successfully prepared by spin coating the corresponding dispersions on the FTO conducting glass, as shown in the SEM images (Figure 4.4c and d**)**. Moreover, the morphologies of PB and ZnHCF powders were characterized by TEM (inset of Figure 4.4c and d), in which the particle-like PB and cubic-like ZnHCF can be clearly observed. PB coated and ZnHCF coated FTO conducting glasses were employed as the working and counter electrode, respectively. The ECD was assembled by sandwiching the solid state electrolyte (0.1 M $LiClO_4$/SN with 7% SiO_2) between the PB and ZnHCF films.

Before the concurrent operations of the self-powered device, the characterization of each device was carried out individually to evaluate their performances. First, the electrochemical property and electrochromic performance of the ECD were characterized by a conventional electrochemical workstation. Figure 4.5a shows the cyclic voltammetry analysis of the ECD at a scanning rate of 100 mV/s. Two obvious redox peaks at -1.0 and 0.5 V were observed, corresponding to the following reversible redox reaction for the coloring and bleaching process, as shown in Eqn. (4.1):

$$Fe_4^{III}[Fe^{II}(CN)_6]_3 + 2Li_2Zn^{II}_3[Fe^{II}(CN)_6]_2 \Leftrightarrow Li_4Fe_4^{II}[Fe^{II}(CN)_6]_3 + 2Zn^{II}_3[Fe^{III}(CN)_6]_2 \quad (4.1)$$

In this reversible reaction, the color change is mainly contributed by the PB electrode. In order to decrease the switching time between the bleached and colored state, a broader potential range between -2.0 to 2.0 V was applied with the consideration of the device stability and the maximum optical attenuation. The electrochromic property of the PB/ZnHCF ECD under various applied potentials was measured by the UV-vis spectrum (Figure 4.5b). As the voltage across the ECD reached -2.0 V, the absorbance spectrum is mostly referred as the pristine FTO conducting glass. As the potential difference increases to 2.0 V, a visible absorbance peak at 695 nm can be obtained, which is mainly contributed by the color change of the PB nanoparticles. To obtain a more intuitive view of the change of the optical property, the transmittance of the ECD was measured from 400 to 800 nm both before and after the coloring process, as shown in Figure 4.5c. It can be found that the transmittance decreased in full range during the coloring process, and the highest variation was achieved at 695 nm with the transmittance decreased from 53.5% to 20.9%. This transmittance change can also be observed by visualization, indicating that the appearance of the ECD changed from transparent (bleached state) to deep blue (colored state), as displayed in Figure 4.5d. The real time transmittance measurement of the ECD at 695 nm is shown in Figure 4.5e, by which a stable transmittance change (ΔT) of 32.6% could be verified by multiple cycles of potential scanning from -2.0 V to 2.0 V. In addition, the switching times for bleaching (τ_b) and coloring (τ_c) were calculated to be 30 and 20 s, respectively.

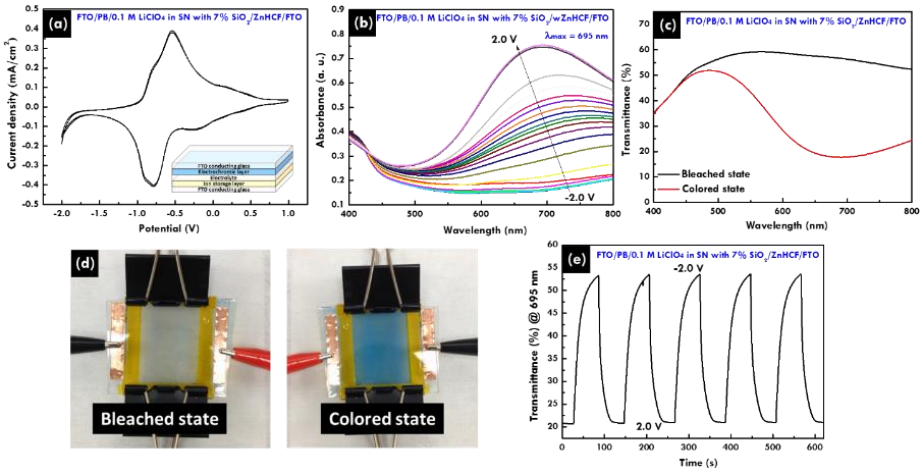

Figure 4.5 (a) Cyclic voltammogram of the PB/ZnHCF ECD with a SN electrolyte with 0.1M $LiClO_4$ and 7% SiO_2 under a scan rate of 100 mV/s, obtained between -2.0 to 1.0 V; (b) UV-absorption spectra of the PB/ZnHCF ECD, obtained at different applied potentials from -2.0 to 2.0 V; (c) the transmittance spectra and (d) photographs of the PB/ZnHCF ECD in bleached and colored states, depicting the colors change of the ECD from colorless to dark blue at applied potential from -2.0 to 2.0 V, respectively; (e) the transmittance change of the PB/ZnHCF ECD in repose to changing the potential between -2.0 V and 2.0 V at 695 nm.[88]

On the other hand, the output performances of the dual-mode TENG constituted by a raining drop-TENG and a wind impact-TENG were also investigated. To accomodate the its application in smart window system, high transparency is an essential factor of the dual-mode TENG, which was obtained by all-transparent materials and was revealed by the transmittance measurement in Figure 4.6a. Its high tranmittance of over 60% in most of the wavelength range guarantees its compatibility in smart window system, which is also confirmed by the photograph of the transparent TENG in Figure 4.6b.

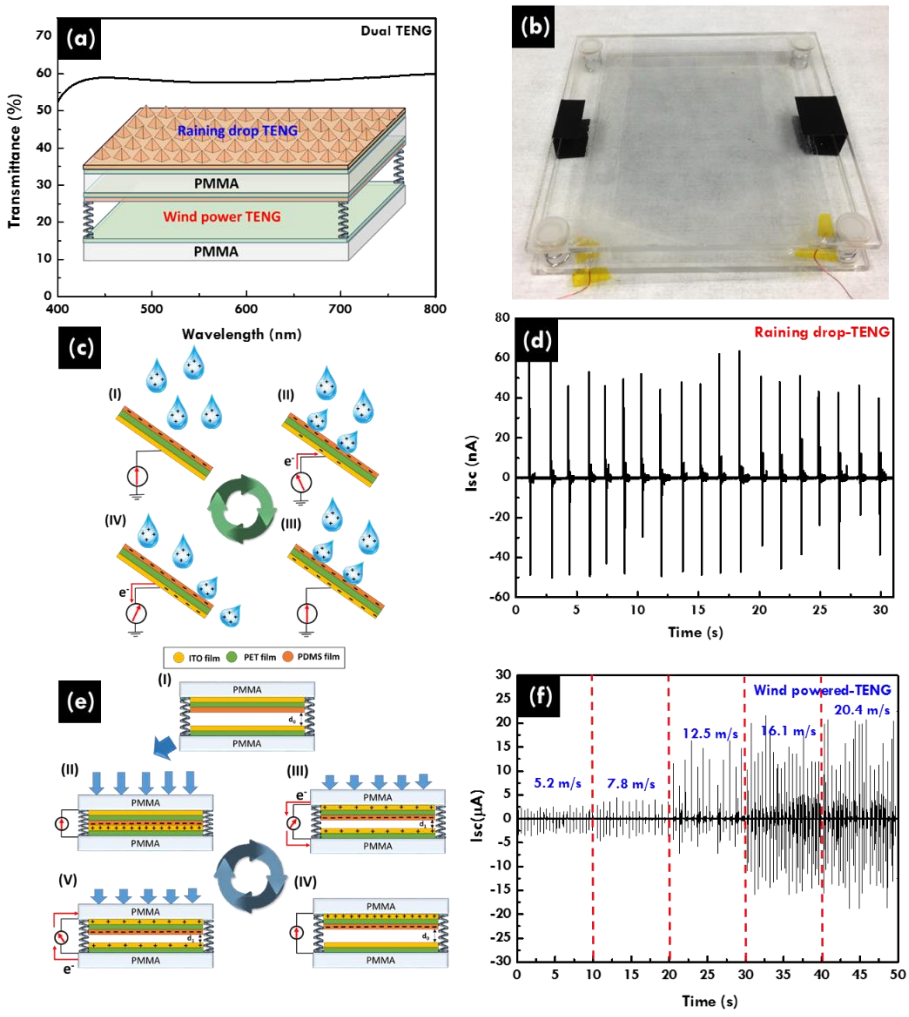

Figure 4.6 (a) The transmittance spectra of the dual mode-TENG; the schemetic structure of the dual-mode TENG was also embedded as the inset; (b) the photograph of the transparent dual-mode TENG; (c) the scheme of the working mechanism of raining drop-TENG for harvesting falling raindrop electrostatic energy; (d) the output of I_{SC} curve of the raining drop-TENG; (e) the scheme of the working mechanism of the wind powered-TENG for harvesting wind impacting energy; (f) the output of I_{SC} curve of the wind powered-TENG with various wind velocities.[88]

The working mechanism of the dual-mode TENG is based on the coupling of contact electrification and electrostatic induction, which can be explained in two seperate parts, as illustrated in Figure 4.6c and e, respectively. Single-electrode working mode was applied for harvesting falling raindrop energy, and the flowing of water droplet on the

surface of PDMS induces the change of potential difference and the corresponding charge flow between its bottom electrode and the ground, as indicated in Figure 4.6c. When the positively charged raining drops contact the hydrophobic PDMS layer with micro-pyramid structures on its surface (ii), a positive electric potential difference will be induced between the bottom electrode and the ground, which drives the electrons flow from the ground to the electrode to balance the electric field (iii). Once the charged raining drops is ejected away from the surface of the hydrophobic PDMS layer, the potential of the ITO electrode will be lower than that of the ground, which means the electrons will flow back in the opposite direction (iv) till the original state (i) is attained. To measure the electric output performance of the raining drop-TENG, the tap water was used to simulate the raindrops and sprayed on the PDMS surface, and the short-circuit current (I_{SC}) of the raining drop-TENG is recorded and shown in Figure 4.6d. The I_{SC} values of the raining drop-TENG is *ca.* 50 nA. This result indicates that raindrop energy generated from the natural environment can be easily harvested by the raining drop-TENG.

Alternatively, contact-mode TENG was used for harvesting the wind impacting energy. As shown in Figure 4.6e, an original separation distance (d_0) between the two triboelectri surfaces (*i.e.* ITO and PDMS) is determined by the elastic constant of the springs and the loading mass (i). The impact from the wind or other mechanical sources will bring the ITO and PDMS layers into full contact. Upon the contact, electrons in the ITO layer are transfered into the PDMS layer due to their diverse triboelectric polarities, which results in net negative charges on the PDMS surface and net positive charges on the ITO surface (ii). Once the wind impact stops, the contacting surfaces start to seperate

due to the restoring force of springs, and the seperation of triboelectric charges will induce potential difference between the top and bottom electrodes. In the meantime, the electric potential difference between the ITO and the PDMS layer drives electrons from the outter circuit to screen the positive triboelectric charges on the PDMS layer (iii). When the two triboelectric surfaces move back to the original position, another phase of electric equilibrium will be reached since negative triboelectric charges on the PDMS layer are screened completely and leaves an equal amount of induced charges on the top ITO layer (iv). Once another wind impacts on the surface of the top electrode to reduce the seperation distance (d_1), the change of electric potential difference with the reversed polarity would be generated and further induced electrons flow through the reversed direction (v). Another equilibrium state would be established after both electrodes reach fully contact with each other (ii). This cyclic process corresponds to instantaneously negative and positive induced currents from the wind powered TENG. For measuring the electric output performance of the wind powered-TENG, a compressed air outlet was used to simulate the wind impact. It can be clearly observed that the peak I_{SC} increases with the elevation of wind speed, which indicates that the dynamic current flow is determined by the deformation rate of the TENG (Figure 4.6f). The maximum I_{SC} value can reach up to 15 μA with the wind velocity of around 16.1 m/s. This result indicates that the wind energy generated from the natural environment can be easily harvested by the wind powered-TENG and the output signal can be utilized for monitoring the ambient wind speed. Moreover, robust test of wind powered-TENG was also performed to investigate its long-term stability.

After characterizing each individual unit of the self-powered smart window system, the electrochromic performance of the integrated ECD driven by the dual mode-TENG was investigated, as shown in Figure 4.7a. For simplicity purpose, only the wind powered TENG was involved in the powering of the smart window, and the implementation of the water drop TENG will add up to the output current and enhance the overall performance of the integrated device. Besides, a mechanical shaker was used to simulate the wind impact at a constant frequency of 5 Hz. The intensity of the motor impact was set as 28.5 kgf/m^2, which was equivalent to the wind velocity of 16.1 m/s. Moreover, a full-wave bridge rectifier was employed to convert the generated alternating-current (AC) pulses into direct-current (DC) signals, as shown in Figure 4.7b, and the rectified DC current could generate 140 nC of charge transfer per cycle for driving the ECD. The effective output power of the TENG was evaluated by monitoring the voltage and current across variable load resistances ranging from 10 Ω to 1 GΩ (Figure 4.7c), and an optimized power density of 130 mW/m^2 can be achieved with a load resistance of 4 MΩ (Figure 4.7d). Figure 4.7e shows the UV/vis-absorbance change of the self-powered ECD driven by the shaker with various durations from 0 to 5,000 s. Significant absorbance differences can be monitored by the UV/vis spectroscopy, and the photographs of the ECD under various durations is also presented as insets of Figure 4.7e showing the color switching of the ECD between colorless and dark blue driven by environmentally-induced mechanical motions. Figure 4.7f shows the transmittance change of the self-powered ECD at a certain wavelength (695 nm) for bleaching and coloring driven by a dual mode-TENG. These result provides a solid evidence to support

that the self-powered smart window is successfully realized by an integrated device with an ECD and a TENG.

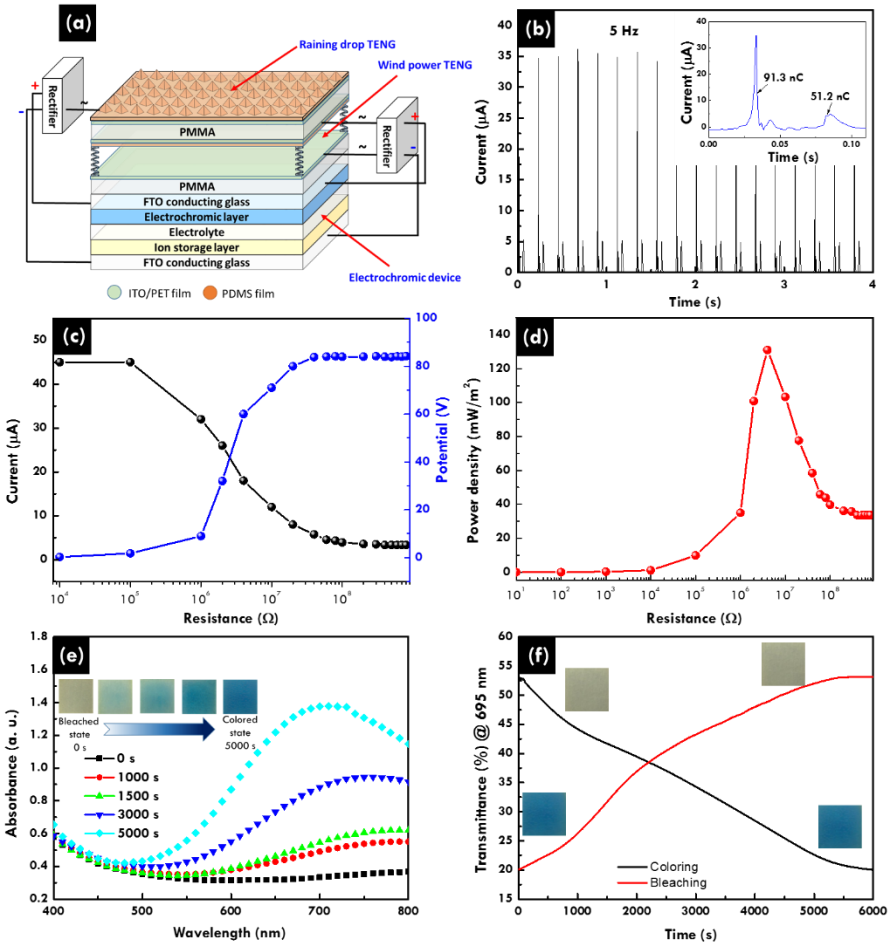

Figure 4.7 (a) The schematic diagram of the detailed structure for the self-powered smart window integrated with full-wave bridge rectifiers; (b) the output of the rectified I_{SC} curve of the dual mode-TENG, and enlarged views of a single current peak and related current charge were also shown as insets (c) the dependences of I_{load} and V_{load} of the dual mode-TENG at various load resistances ranging from 10 Ω to 1 GΩ; (d) instantaneous P of the dual mode-TENG on the resistance of the external load; (e) the UV-absorption spectra of the self-powered ECD obtained at different duration times, and the pictures of ECD at different duration times were also presented as insets for depicting the changed colors of the ECD at different times; (f) the transmittance change of the self-powered smart window in repose under various duration times for bleaching and coloring.[88]

To illustrate the working of the self-powered smart window as an integrated device, a series of schematics indicating the coupling of charge transfer and

electrochemical reactions in various steps are presented in Figure 4.8. Since the power generation process of the dual-mode TENG was already decribed in Figure 4.6, it will not be further discussed here. In the ideal case, the amount of charges injected into the PB layer of a ECD should be equal to the total amount charge transfer from the two output terminals of the TENG. Here, as dipicted in stage (iii) and (v), both the wind-impact and rain-drop TENGs generate an AC output current with distinct directions of charge flow during a full operation cycle. The direction of the current flow will be regulated by the full-wave bridge rectifier to ensure that the current flow through the ECD will be in a constant direction for charging the PB layer. The charging cycle from stage (ii) to (v) in Figure 4.6 will keep taking place for harvseting energy and then charging the ECD when the self-powered window system is subject to a continuous wind impact or raindrop falling.

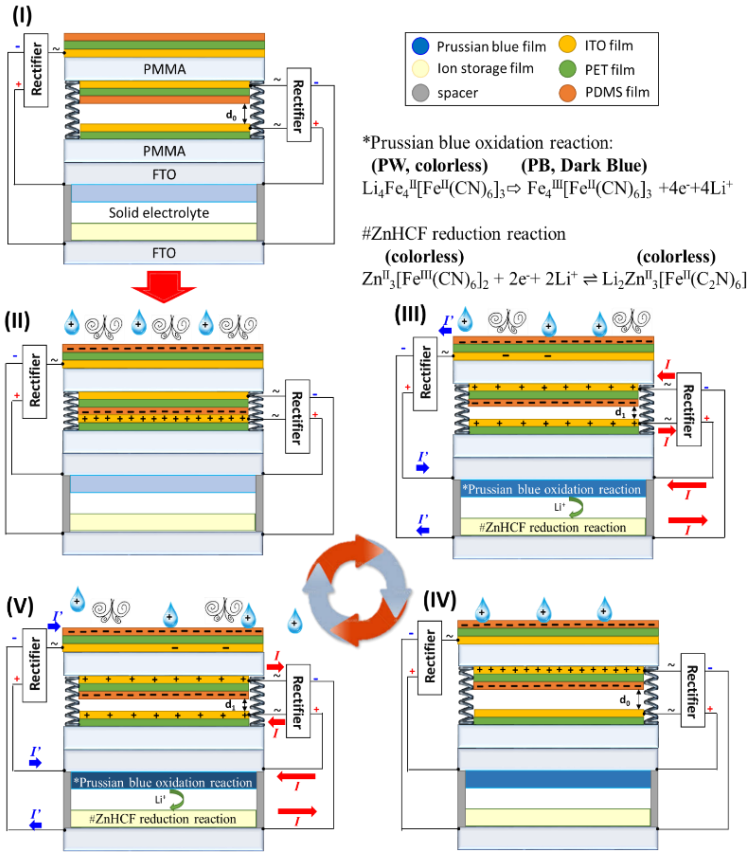

Figure 4.8 The scheme of the working mechanism of the self-powered window for spontaneously harvesting falling raindrop electrostatic energy and wind impacting energy.[88]

In summary, the concept of motion-driven self-powered smart window system was realized by integrating an electrochromic device with a dual-mode triboelectric nanogenerator. The TENG can take advantage of the environmental oscillations such as wind blowing and rain drops to deliver an output current of up to 45 μA, corresponding to an effective power density of 130 mW/m^2. Reversible electrochromic reactions can be driven directly by the TENG, and a maximum transmittance change of 32.4% as well as visible color change can be obtained, which is comparable to the ECD driven by an electrochemical workstation. This research presents a substantial advancement in the

practical applications of nanogenrators and self-powered systems, which will initiate promissing improvement in self-powered flexible displays, wearable electronics, and efficient buildings.

CHAPTER 5

APPLICATIONS OF NANOGENERATORS AS ACTIVE SENSORS

5.1 Piezoelectric nanogenerator for self-powered transportation monitoring

Besides the energy harvesting function, we also performed further investigation on the applications of the ZnO piezoelectric nanogenerator (NG) as a self-powered active sensor for transportation monitoring on the road. Herein, the NG device was employed to detect the vehicle speed and vehicle weight instantly. Figure 5.1a illustrates the basic principle of vehicle speed monitoring using NG. Generally, two NG devices with similar size were placed consequently along the rolling path of a moving vehicle. The distance between the two NG devices was fixed as Δs=0.6 m. As the front tire of the vehicle rolled on the two NGs subsequently, two successive voltage peaks could be recorded by the measurement system, with a measurable time interval of Δt. Assuming that the vehicle speed was constant during this quick process, we were able calculate the instant vehicle speed simply by $v=\Delta s/\Delta t$. Figure 5.1b-e lists the measured voltage peaks under the tire rolling of the vehicle at various speeds, from 1.0 m/s to 4.0 m/s. The high end detection limit was mainly determined by the sampling rate of the measurement system and the distance between the two NG devices (Δs). At current conditions (the sampling rate is 500 s^{-1} and the NGs' distance is 0.6 m), the detection limit was ~300 m/s and it was high enough even for vehicle speed detection even in an express way.

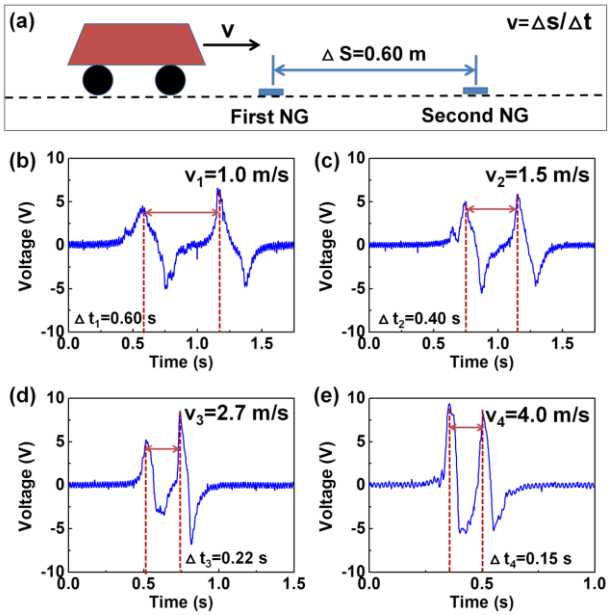

Figure 5.1 The application of the TFNG for self-powered transportation monitoring by detecting vehicle speed. (a) A schematic illustration showing the principle for measuring the vehicle speed on the road by the NG device. (b-e) The measured voltage-time relationship induced by vehicle tire with various speeds. The vehicle speed is calculated to be 1.0, 1.5, 2.7, and 4.0 m/s, respectively.[34]

Theoretically, the output voltage of piezoelectric NG increases with the applied strain (or stress) on the structure. This is the principle for the vehicle weight monitoring using NG. Figure 5.2a shows the output voltage of NG driven by different vehicles with various curb weights, but at a constant and relatively low speed. It could be found that the output voltage increased with the vehicle weight. Figure 5.2b shows that the averaged output voltages had shown a linear relationship as a function of the curb weight of the vehicles. This result demonstrates the possibility of using NG as a self-powered sensor for monitoring the weight of vehicles on the road. Compared to traditional techniques for transportation monitoring, like speed camera and electronic balance, the NG-based speed and weight monitor has the following advantages: (1) it is a self-powered sensor and does not require external power source or specific maintenance; (2) it is transparent and

flexible, which means it can be easily attached onto the road with any sort of environmental conditions, without interrupting the traffic.

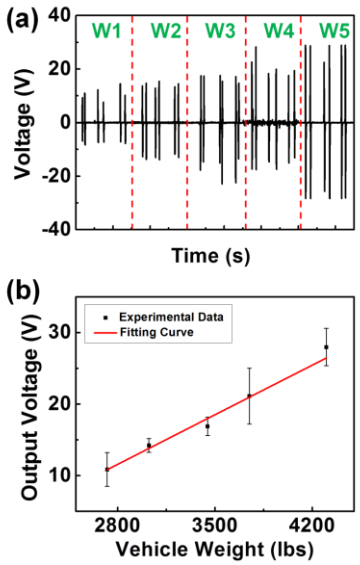

Figure 5.2 The application of the TFNG as self-powered pressure sensor for monitoring the vehicle weight. (a) Measured output voltages of NG device from tire rolling with various vehicle weights. It was observed that the output voltage increased with increasing vehicle weight. (b) Linear fitting of the average output voltage as a function of the vehicle weight.[34]

5.2 Spring-substrated piezoelectric nanogenerator for self-powered balance

Elastic spring is a commonly employed mechanical accessory in lots of equipment and automobiles, and it is one of the most traditional balances used for measuring weight in reference to the extended length of the spring. In this work, a spring-substrated nanogenerator (SNG) was fabricated to accomplish the monolithic integration of an active sensor device onto a mechanical component. The ZnO nanowires (NWs) were densely grown on the surface of the spring by the wet chemical approach. The SNG was fabricated by applying polymer passivation onto the textured ZnO NW film and silver electrode on the composite structure. The SNG showed stable output open-circuit

voltage and short-circuit current under a cyclic compressive force. Both the output voltage and current had linear relationship with the weight loaded on the spring, thus, the NG was utilized as an active mechanical sensor for measuring the weight applied onto the spring. The applicability of the active sensor was systematically analyzed for different parameters. This work is a new step towards practical applications of nanogenerators as self-powered sensors.[89]

The structure and general working principle of the SNG are schematically exhibited in Figure 5.3a-c. Compressive springs with variable sizes were selected as the skeletons of the SNG devices. The helix-shaped spring surface composed of high carbon steel, which was taken as the substrate for the growth of ZnO NWs and also employed as the inner electrode due to the conductive nature of the steel. The ZnO NWs were grown by the wet chemical approach on the treated spring surface. The surface morphology of the ZnO NWs is presented by the scanning electron microscopy (SEM) images in Figure 5.3d and e. The NWs were uniformly grown on the spring and densely packed as a textured film with the c-axes of the NWs pointing outward. The as-synthesized NW film was spin-coated with polymethyl methacrylate (PMMA) as a buffer layer and deposited with silver as the outer electrode. Both the inner and outer electrode was connected to the external measurement circuit by copper electric leads, and the whole device was encapsulated with polydimethylsiloxane (PDMS) to protect the electrode.

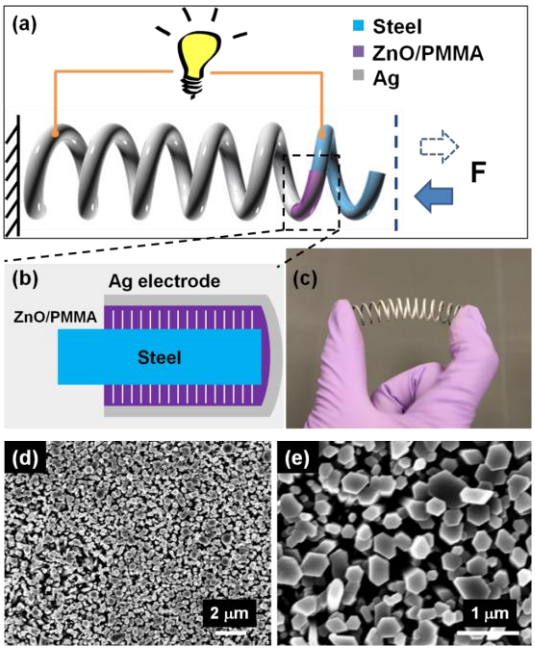

Figure 5.3 (a) Schematic structure of the spring-substrated nanogenerator, in which textured piezoelectric ZnO nanowire film is grown on the surface of the elastic wire. (b) A cross-sectional schematic illustration of the nanogenerator showing its detailed structure, which is composed of steel spring (substrate and inner electrode), ZnO nanowire film, PMMA insulating layer, as well as the outer Ag electrode. (c) A photograph of the spring-substrated nanogenerator. (d) Low magnification SEM image of the ZnO nanowire film indicating the uniformity of the NW film. (e) High magnification SEM image of the ZnO NW film showing the hexagonal structure of the ZnO nanowires.[89]

In the measurement for the output performance of the SNG, one end of the spring was fixed onto a three-dimensional stage; meanwhile a mechanical linear motor was employed to apply a periodic longitudinal compressive force to the SNG. As the compressive force is applied onto the spring, the strain-induced piezoelectric potential (piezopotential) in ZnO will be created and drive the electrons flowing in the external load until the accumulated electrons reach equilibrium with the piezopotential; once the applied force is released, the piezopotential diminishes and the accumulated electrons will flow back in the opposite direction, which leads to an AC current. With an applied

compressive force of 15.2 N (the corresponding displacement of the spring is 10 mm), for a spring with spring constant of 1.52 N/mm, the output open-circuit voltage and short-circuit current of the SNG was ~0.23 V and 5 nA, respectively, as displayed in Figure 5.4a and b. The stability of its output performance was also tested through continuously loading and unloading the periodic force for three days at a frequency of 0.32 Hz. From Figure 5.4c and d, it can be found that the output of the SNG only showed a decay of 3% ~ 4% after three days of continuous working (corresponding to ~80,000 cycles), owing to the high flexibility of the ZnO NWs and thus the high robustness of the SNG device. The stability of the SNG's output ensures its application as an active mechanical sensor, which will be discussed later.

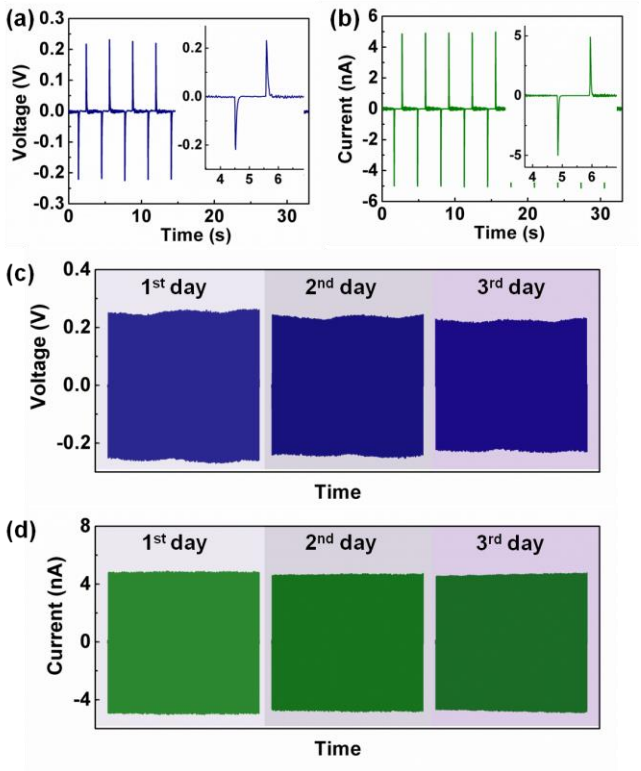

Figure 5.4 Electrical output performance of the SNG. (a) Open-circuit voltage and (b) short-circuit current of the SNG. The insets are the enlarged views of the open-circuit voltage and short-circuit current. (c, d) Stability tests of the (c) output voltage and (d)

current of the SNG with continuous working in three days at a frequency of 0.32 Hz. The data presented contains 200 cycles of the output voltage/current in each day.[89]

To achieve a fundamental understanding and offer guidance for the practical design of the SNG, its working mechanism was analyzed using finite element calculation. Due to the relative complexity of the stress distribution on the surface of the spring when loaded with a longitudinal force, only the tangent force term was considered as contribution to the piezopotential across the ZnO NW film. In the numerical calculation, a segment of the spring as well as the corresponding ZnO NW film was selected for the calculation. At a displacement of 10 mm for the spring deformation, the tangent force applied to the selected segment of spring/ZnO NW composite was calculated based on the following relationships:

$$F_0 = kx \tag{1}$$

$$F = F_0 \cdot \sin\alpha \tag{2}$$

Here, F_0 is the total longitudinal force, which is proportional to the displacement of the spring (x), F is the tangent force that will act parallel to the ZnO film, and α is the declination angle of the spring. With a spring constant of k = 1.52 N/mm, and the declination angle of $\alpha = 0.22^{\circ}$, it could be calculated that the applied tangent force is F = 3.3 N. Under this applied force, the potential distribution across the thickness direction of the ZnO NW film was calculated from finite element analysis, as given in Figure 5.5a. The calculated potential difference between the top electrode and the bottom spring electrode is 0.27 V, which is consistent with the measured open-circuit voltage under the same condition. Moreover, the relationship between the strain-induced piezoelectric

potential and the displacement of the spring was also calculated in the same way and displayed in Figure 5.5b. The piezoelectric potential shows linear relationship with the displacement of the spring, which is equivalent to the applied strain or force on the ZnO NW film. Based on this result, the SNG could be employed to serve as an active mechanical sensor, by which the information of the applied force is exhibited by the measured output open-circuit voltage and/or short-circuit current of the SNG without applying an external power source. The expected sensitivity was 27 mV/mm from the result of Figure 5.5b. A more detailed analysis of the periodical current flow behavior of the SNG under cyclic compressive force is illustrated in Figure 5.5c and d. As observed from the enlarged diagram showing a full cycle of the output current of the SNG (Figure 5.5c), it can be divided into four stages corresponding to different applied force conditions: (I) The spring was fixed at one end, and its free end was applied with a compressive force by a linear motor from its original position. The strain-induced piezopotential will drive the electrons flowing in the external circuit, until the accumulated electrons came to equilibrium with the piezopotential. Thus, a current peak was measured. (II) The compressive force reached its maximum value and kept constant, and there was no current flowing in the external circuit, which was reflected by the inset of Figure 5.5c (top left). (III) As the compressive force was released, the piezopotential vanished and the accumulated electrons would flow back through the external circuit to the original electrode, and a current peak with the opposite polarity was measured. (IV) At the end of the cycle, the accumulated electrons had fully flown back, and the current flow tended to be zero. However, different from stage (II), the linear motor was fully removed from the spring in this stage, and the free vibration of the spring would induce

an oscillation in output current of the SNG, which was also shown in the inset of Figure 5.5c (bottom right), indicating that the SNG had the function as a self-powered vibration sensor for monitoring buildings or bridges.

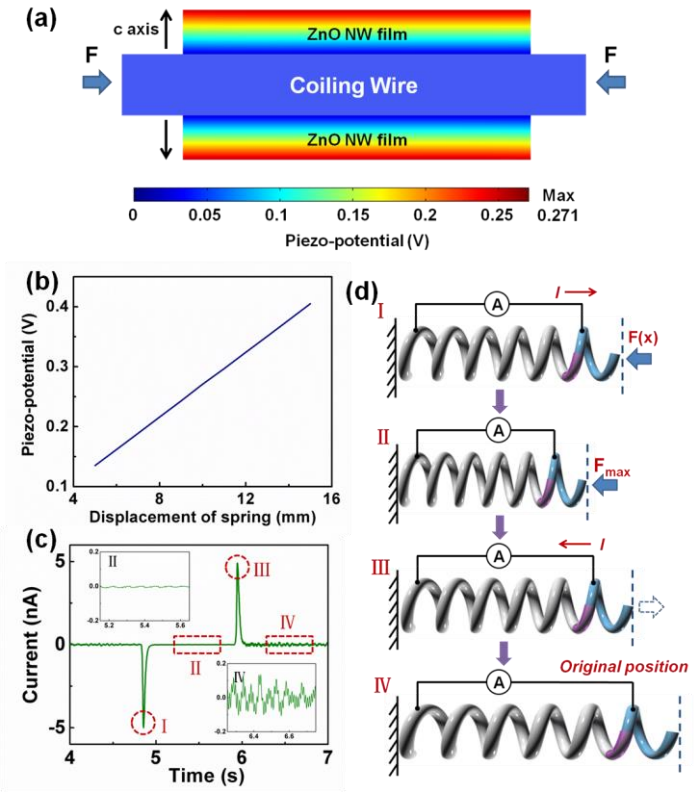

Figure 5.5 (a) The calculated piezopotential distribution in the ZnO nanowire film with an applied compressive force. Since the size of the spring is a lot larger than the size of the nanowire and the ZnO film thickness, the calculation was done for a simplified case that the 3D shape of the spring was not considered. This result only gives the potential distribution in a segment of the spring-substrated nanogenerator. (b) The calculated piezopotential across the ZnO nanowire film as a function of the displacement of the spring. (c) The detailed analysis of the output current of a SNG, which consists of four steps. (d) The schematic diagrams displaying the measurement process of the spring-substrated nanogenerator and an explanation of the AC output current.[89]

Since the displacement of the spring has a direct relationship with the applied force by the Hooker's Law, the output voltage and current of the SNG as a function of the displacement of the spring were measured to demonstrate the performance of the SNG as

an active mechanical sensor. Figure 5.6a and b shows the measured magnitude of the output open-circuit voltage and short-circuit current with a series of displacements ranging from 5 mm to 15 mm. The measurement result clearly indicates that both the open-circuit voltage and short-circuit current increase with the displacement of the spring. Through statistical analysis of the measured data, it was calculated that the voltage and current sensitivity of the active sensor was 7 mV/mm and 0.44 nA/mm, respectively. Based on these results, the application of the active sensor was proposed for self-powered weight measurement, as illustrated in Figure 5.6c. The SNG was placed vertically with a tiny plate on its top (the weight of the plate and the induced deformation of the spring was negligible compared to the heavy object for measurement), and the heavy object for measurement was then placed on top of the plate. The induced output voltage/current could be measured, from which the information of the weight of the object was derived. Figure 5.6d shows the linear relationship between the output voltage/current responses and the equivalent weight calculated from the spring displacement. It could also be calculated that the voltage and current sensitivity for the weight measurement were 45 mV/kg and 2.8 nA/kg, respectively.

The output of the SNG is mainly determined by the external force applied on the spring; however, it might also be affected by other parameters like the loading rate of the force, the spring size and the working frequency. Therefore, controlled experiments are indispensable to exclude other possible interferences and to validate the measured working curve of the active sensor. Since loading of the applied force is a dynamic process, the loading rate dictated by the acceleration of the motor, is one of the most important parameters to study. Ideally, the open-circuit voltage should merely depends on

the strain-induced piezopotential and thus the magnitude of the applied force; while the short-circuit current is not only dependent on the amount of charges transferred, but also affected by the charge flow rate, which is decided by the acceleration of the loaded force. Figure 5.6e and f shows the measured open-circuit voltage and short-circuit current as a function of the acceleration of the linear motor (the external force was kept constant at 15.2 N), and the voltage/current-acceleration relationship was statistically analyzed and summarized, as shown in Figure 5.6g and h. The results are consistent with theoretical expectation, in which the open-circuit voltage is generally independent of the acceleration, but the short-circuit current shows a slightly rising trend as the acceleration increases. Therefore, it clearly indicates that the open-circuit voltage is a more accurate and reliable way for the self-powered weight measurement. The short-circuit current, though changing with loading rate, could give more detailed information about the dynamic process for the applied force.

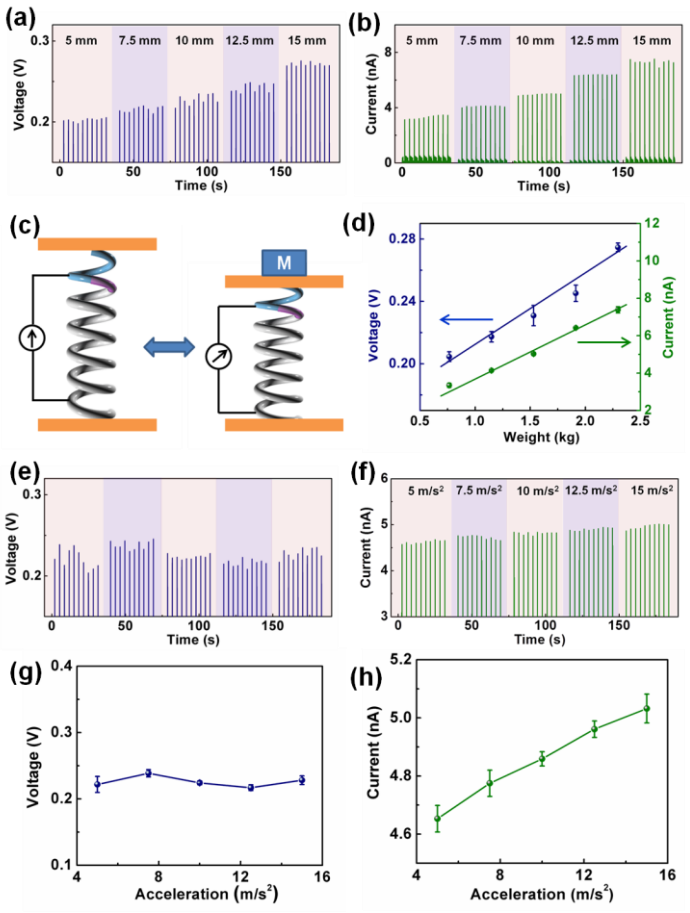

Figure 5.6 Electrical measurement of the active mechanical sensor for self-powered weight measurement. (a, b) Output open-circuit voltage and short-circuit current of the active sensor as a function of the displacement of the spring. (c) Schematic illustration showing the working mode of the active mechanical sensor for self-powered weight measurement. (d) Linear relationship between the output and loaded weight on the spring-substrated nanogenerator. (e, f) The measured open-circuit voltage and short-circuit current as a function of the acceleration of the linear motor by which the external force was loaded. (g, h) The statistical relationship between the output voltage/current and the acceleration of the linear motor.[89]

Within analogous to the acceleration of the linear motor, the frequency of the applied impact should have little effect on the output open-circuit voltage; while the output shirt-circuit current is more sensitive to the impact frequency. In this case, the frequency test of the open-circuit voltage is given in Figure 5.7 and indicates that the frequency of the impact has little impact on the magnitude of output open-circuit voltage especially in low

frequency range, which further confirms the effectiveness of using the output voltage as the signal for the active sensor.

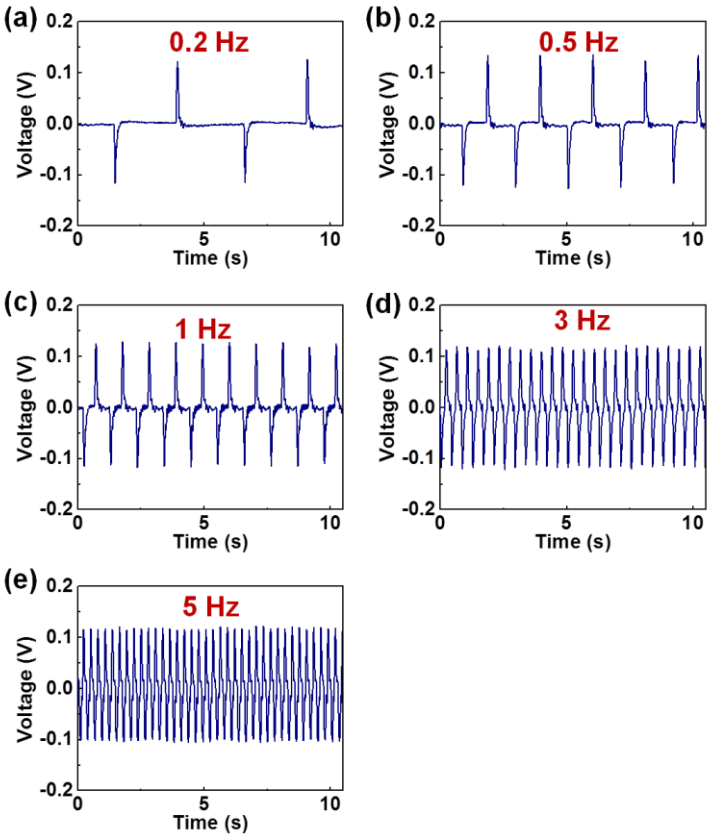

Figure 5.7 The measured output voltage of a smaller SNG with variable frequencies of the loading force, but the displacement of the spring was kept at a constant.[89]

In summary, by growing nanowire films of ZnO on the surfaces of the elastic wire for a spring, a spring-based nanogenerator has been demonstrated as an active sensor for measuring the weight applied onto the spring without the use of an external power source. Both the output voltage and current displayed linear relationship with the equivalent applied weight to the spring, and the weight measurement was validated by comparison with other effects like loading rate of the force, spring size, and impact frequency. Our study shows that the output voltage of the nanogenerator could be utilized

as an active sensor signal for self-powered weight measurement system, which can be further employed in transportation monitoring.

5.3 Triboelectric nanogenerator for self-powered pressure sensor

Tactile sensing/imaging has been an important area of research for its applications in artificial skin, flexible electronics, human-electronics interfacing, and micro-electromechanical system (MEMS). Major research efforts have been focused on improving the sensitivity, spatial resolution, response time, long-time stability, and cyclic reliability of the pressure sensor devices and the integrated matrix. The sensing capability of most of the established pressure sensors were enabled by the pressure-induced variations of their inner properties, such as conductance, capacitance, or even optical transmittance of the media (like pressure-sensitive rubbers) assisted by field effect transistors (FETs) as the read-out elements. Employing the state-of-art micro/nano-scale fabrication and integration technology, numerous advancements have been achieved through building matrix of nanodevices on flexible/transparent substrates for high-resolution shape-adaptive pressure imaging. But one common limitation is that most of these sensors rely on an externally supplied power source, otherwise none of them will work.

To solve this problem, we fabricated a flexible triboelectric active sensor (TEAS) with excellent performance and low processing cost. The working principle of the TEAS is similar to the TENGs and was theoretically verified by numerical calculations with finite element method (FEM). Both static and dynamic pressure sensing were

accomplished by the same device with different measurement approaches. Specifically, the open-circuit voltage as well as the amount of the transferred charge density was employed for static pressure detection, while the pulse-like short-circuit current peak was used for dynamic pressure monitoring. Owing to this active sensing principle, a supreme performance of pressure detection was achieved on the TEAS, including high sensitivity of 0.31 kPa^{-1}, fast response/relaxation time of < 5 ms, long-term stability/reliability of 30,000 cycles, as well as a low detection limit of 2.1 Pa. Multiple TEAS devices were integrated into a sensor array for tactile imaging, and distinguishable spatial profiles of the sensor array were realized for self-powered monitoring and mapping the applied local pressures distributions. This work is an unprecedented progress towards the practical application of nanogenerators, the realization of self-powered system, and further advancement of flexible electronic devices.[67]

The device structure of the TEAS was schematically depicted in Figure 5.8a. Based on the metal-insulator triboelectric pairs, the fabrication of the TEAS device could be divided into two parts. In the first part, the polydimethylsiloxane (PDMS) membrane was modified with micro-patterned pyramid structures through photolithography and template method. A scanning electron microscopy (SEM) image of its surface morphology is shown in Figure 5.8b. The pyramid micro-structures were uniformly distributed on the inner surface of PDMS, with the size of ~ 10 μm. The processed PDMS membrane was deposited with Au electrode on its outer surface. In the second part, a piece of Al was assembled with the composite of Ag nanowires and nanoparticles that were prepared by a seed-mediated approach. The micro/nano structures on both inner surfaces were introduced to enhance the triboelectric effect and the effective contact area

between the two surfaces, which would help to improve the pressure response of the TEAS. The two layers were bonded by non-conductive tapes and both electrodes were connected to electrical leads. Due to the elastic resilience of the materials, the device naturally forms an arch shape, with an air gap presented for effective charge separation (Inset of Figure 5.8a). The size of the TEAS is 2 cm×2 cm, which of course can be much reduced in size.

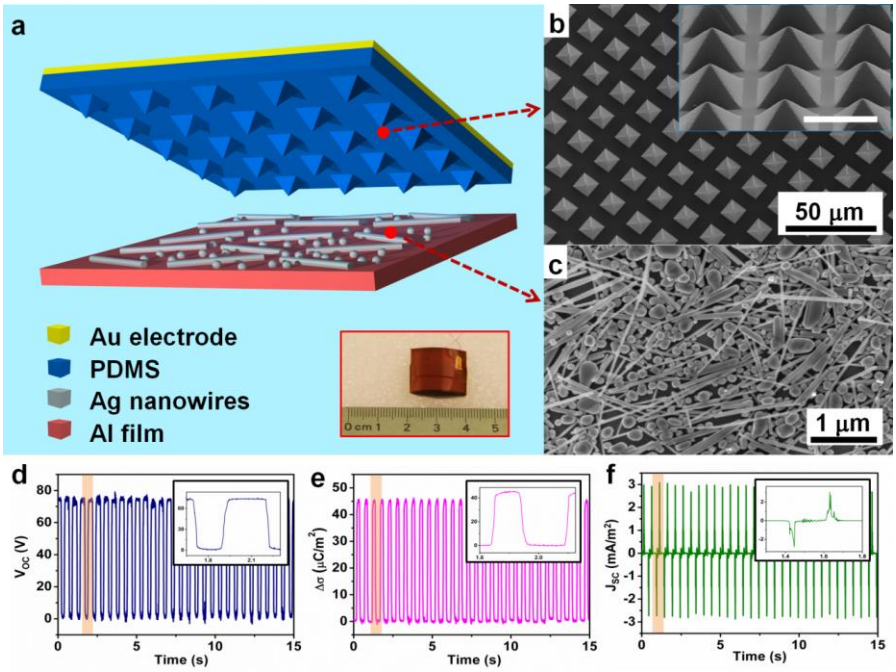

Figure 5.8 The basic structure and typical electrical response of the triboelectric active sensor applied with a cyclic pressure. (a) The schematic illustration of the TEAS device with both inner surfaces modified by micro-pattern PDMS structures and Ag nanowires/nanoparticles composite. The inset is a photograph of the TEAS device. (b) The SEM image of the pyramid-structured micro-patterns fabricated on the inner surface of the PDMS membrane. The inset is a high magnification SEM image of the micro-patterns, and the inset scale bar is 10 μm. (c) The SEM image of the Ag nanowires/nanoparticles composite assembled on the inner surface of the Al foil. (d-e) The measured typical electrical response including (d) the open-circuit voltage, (e) the transferred charge density, and (f) the short-circuit current density of the TEAS upon a cyclic pressure.[67]

The typical electrical responses of the TEAS under external agitations by a mechanical shaker (ET-126-1-4, Labworks Inc.) are shown in Figure 5.8d-f. With a 2 Hz cyclic pressing force applied on the TEAS, it produces an open-circuit voltage (V_{OC}) of ~ 75 V, transferred charge density ($\Delta\sigma$) of ~ 45 $\mu C/m^2$, and short-circuit current density (J_{SC}) of ~ 3 mA/m^2. The working principle of the TEAS is based on the coupling effect of contact electrification and electrostatic induction. When the two triboelectric layers are brought into contact by an external force/pressure, the electrons will be injected from the Al layer into the PDMS layer (due to the difference in ability to attract electrons), leaving net positive charges in Al foil and net negative charges on the surface of the PDMS membrane. In the open-circuit (OC) condition, as the external pressure is withdrawn, the V_{OC} will increase linearly corresponding to the vertical gap distance between the two layers (d) *via* the following equation:

$$V_{OC} = \frac{\sigma \cdot d}{\varepsilon_0} \tag{5.1}$$

ε_0 is the permittivity in vacuum and σ is the triboelectric charge density, which is considered as constant in this work. It should be noted that the V_{OC} starts decreasing when the external pressure is applied (with smaller d), and reverts to its maximum level when the pressure is fully removed ($d = d_0$). As for the short-circuit (SC) condition, this change of potential difference in correspondence to the mechanical agitation will drive the electrons moving back and forth in the external circuit, leading to a current flow with AC manner. The amount of the transferred charge density ($\Delta\sigma$) as a result of pressure change is also a function of d, which is given by:

$$\Delta\sigma = \frac{Q_0 - Q}{S} = \frac{\sigma \cdot d_0}{\frac{d_{PDMS}}{\varepsilon_{r,PDMS}} + d_0} - \frac{\sigma \cdot d}{\frac{d_{PDMS}}{\varepsilon_{r,PDMS}} + d} \tag{5.2}$$

Q and Q_0 are the amount of induced charges on one electrode with and without pressure, respectively, S is the effective area of electrodes, d_{PDMS} and $\varepsilon_{r,PDMS}$ is the thickness and relative dielectric constant of the PDMS membrane, respectively, and d_0 is the maximum gap distance without pressure. Apparently, the $\Delta\sigma$ increases as d is reduced, but not with linear relationship. Hence, the J_{SC} could be deducted as

$$J_{SC} = \frac{d(\Delta\sigma)}{dt} = -\frac{dQ}{S \cdot dt} = -\frac{\sigma \cdot \frac{d_{PDMS}}{\varepsilon_{r,PDMS}}}{(\frac{d_{PDMS}}{\varepsilon_{r,PDMS}} + d)^2} \cdot \frac{\delta d}{\delta t} \tag{5.3}$$

It can be found that the magnitude of the J_{SC} is not only dependent on the gap distance but also affected by the loading rate of the external pressure ($\delta d / \delta t$). This expectation was confirmed in the measurement with higher frequency of the applied pressure (6 Hz), and the J_{SC} displays a gigantic increase up to ~ 40 mA/m^2.

Therefore, the output open-circuit signal from the TEAS (see Eq. (5.1)) is a static signal that is only dictated by the gap distance d, which is a measure of the magnitude of the applied pressure/force. The output current (Eq. (5.3)) is a dynamic signal that is determined by the speed at which the gap was squeezed, thus, it gives the information about the rate of the pressure/force being applied.

Continuing from the above analysis, the V_{OC} has direct and linear relationship with d, and thus will be an ideal parameter for static pressure measurement. Therefore, a numerical calculation regarding to the V_{OC}-d relationship is necessary to verify the theoretical basis of the TEAS. For simplicity purposes, the TEAS device is treated as

parallel-plate capacitor in the established model, where the PDMS plate with Au electrode was placed parallel with the Al plate with variable gap distances ranging from 0 to 20 μm. The triboelectric charge density on the inner surface of PDMS plate was assigned as 45 $\mu C/m^2$, which is equal to the measured transferred charge density in Figure 5.8e. The calculated potential distribution around the parallel-plate structure is displayed with color scaling in Figure 5.9a-e. It can be found that the potential difference between the top and bottom electrodes shows an obvious decreasing trend with decreasing gap distance (increasing pressure). The potential difference decreases to 0 when the two plates reach a full contact (Figure 5.9e, d=0), as expected from Eq. (1). The calculated potential difference displays perfect linear relationship with the gap distance and very little deviation from the proposed relationship in Eq. (5.1) (Figure 5.9f). Little difference could be observed from the list of calculation results, indicating that the edge effect could be excluded on condition that the size of the device far surpasses the gap distance.

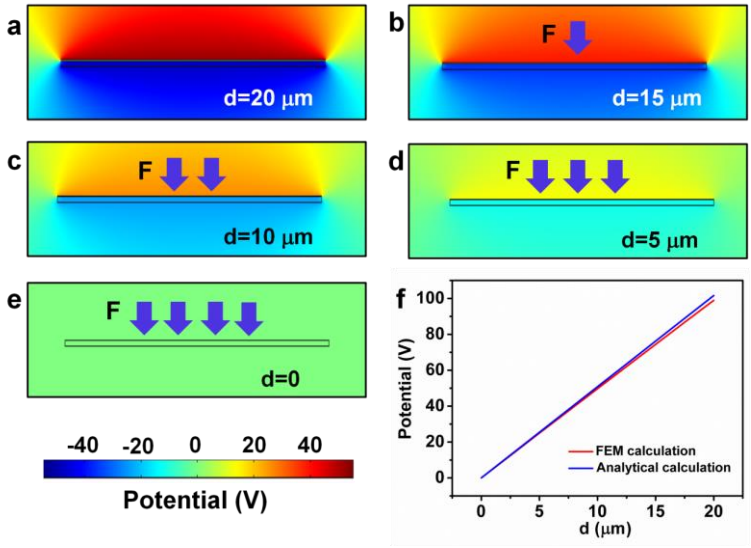

Figure 5.9 Numerical calculations of the correlation between the potential difference and the gap distance of the TEAS. (a-e) The calculated potential distributions around the TEAS with variable gap distances ranging from (a) 20 μm, (b) 15 μm, (c) 10 μm, (d) 5

μm, and (e) 0 μm. The bottom inset is the color scale of the potential. (f) The summarized calculation results indicating the relationship between the potential difference and the gap distance, as well as the comparison of the calculation results *via* the finite element method and the analytical formula.[67]

In order to correlate the external pressure with the V_{OC}, the material resilience of the TEAS was considered as the spring-entangled structure using the Hooker's Law:

$$p = \frac{k \cdot x}{S} = \frac{k \cdot (d_0 - d)}{S} \tag{5.4}$$

p is the pressure and k represents the elastic property of the materials in the TEAS. Combining Eq. (1) and (4), we can get

$$\frac{V_{OC,0} - V_{OC}}{V_{OC,0}} = \frac{d_0 - d}{d_0} = \frac{S}{k \cdot d_0} \cdot p \tag{5.5}$$

Hence the relative variation of the V_{OC} should be expected to show directly linear relationship with the applied pressure, and thus it is a reliable parameter for measuring the magnitude of the external pressure applied onto the TEAS, while the J_{SC} is able to provide the dynamic information of the applied pressure (i.e. loading rate). Combining the analysis on the measurement of both the V_{OC} and the J_{SC}, the TEAS device is capable of giving the detailed information about the ambient mechanical stimulations. On this basis, we designed and conducted a series of measurements to characterize the performance of the TEAS, as discussed below.

In the measurement setup, the TEAS device was attached onto a flat plate and fixed on the end of a force gauge (Vernier Software & Technology), and cyclic external pressures were applied by a mechanical linear motor. The data for both the output parameters (the V_{OC}, $\Delta\sigma$, and J_{SC}) and the real-time force/pressure were recorded and

analyzed in the same computer. Figure 5.10a is the real-time measurement result of V_{OC} under series of different pressures. The reference level of voltage was selected in the way that the V_{OC} approached 0 with the maximum pressure when the two surfaces came into full contact. It could be observed that the V_{OC} stays at the maximum level (V_0 = 60 V) when there is no pressure, and decreases to a lower level once the external pressure is applied. The voltage variation (V_0-V) increases with increasing pressure, and the relationship between relative voltage variation (V_0-V)/V_0 and magnitude of pressure is plotted in Figure 5.10b (the subscript "OC" is omitted here for convenient expression). The plot can be divided into two regions based on difference in sensitivity. In the low pressure region (Region I), the sensitivity of the TEAS is 0.31 kPa^{-1}, which is much higher than that of the high pressure region (0.01 kPa^{-1} in Region II). The separated fittings of the data in both regions display good linear behavior (R_I^2=0.965, and R_{II}^2=0.985), which reveals the validity of the device as a reliable pressure sensor. The reason for different sensitivities can be explained based on the previous analysis. In Region I, the pressure increase results in drastic gap distance change as estimated in Eq. (4), introducing larger voltage variations; while it is quite probable that the gap distance has already been close to 0 from the turning point in Region II, and the increasing pressure only works for enhancing the effective contact area between the two layers. In another word, the V_{OC} tends to saturate to zero in Region II, and the applied pressure has little effect on the voltage variation.

To verify the theoretical expectation that the V_{OC} merely depends on the magnitude of the applied pressure rather than the loading rate, the voltage response of the TEAS was tested at a constant pressure of ~ 2 kPa but of different loading rates that were

controlled by the accelerations of the linear motor. As shown in Figure 5.10c-d, as the accelerations vary from 2.5 to 30 m/s^2, the relative voltage variations almost remain constant; though a minor increasing trend is present, possibly resulting from minor pressure variations. The stability of the TEAS device was examined through continuously loading and unloading a constant pressure (~ 2.5 kPa) for over 30,000 cycles, as exhibited in Figure 5.10e. The voltage response was measured after every 10,000 cycles, during which 300 cycles were recorded and displayed in Figure 5.10e. The voltage response only shows a minor decay of ~ 6.7% after 30,000 cycles, through which the stability of the TEAS is confirmed. Moreover, in Figure 5.10f, the real-time pressure measurement and voltage response was displayed in the same plot and both plots match perfectly. Hence, the voltage response is capable of revealing the detailed information of the loading process of an external pressure. From the comparison of plots for the loading and unloading process of the external pressure, it is estimated that both the response time and the relaxation time are < 5 ms, demonstrating the prompt response of the nanogenerator-based active pressure sensor and proving its superior advantage to conventional sensors.

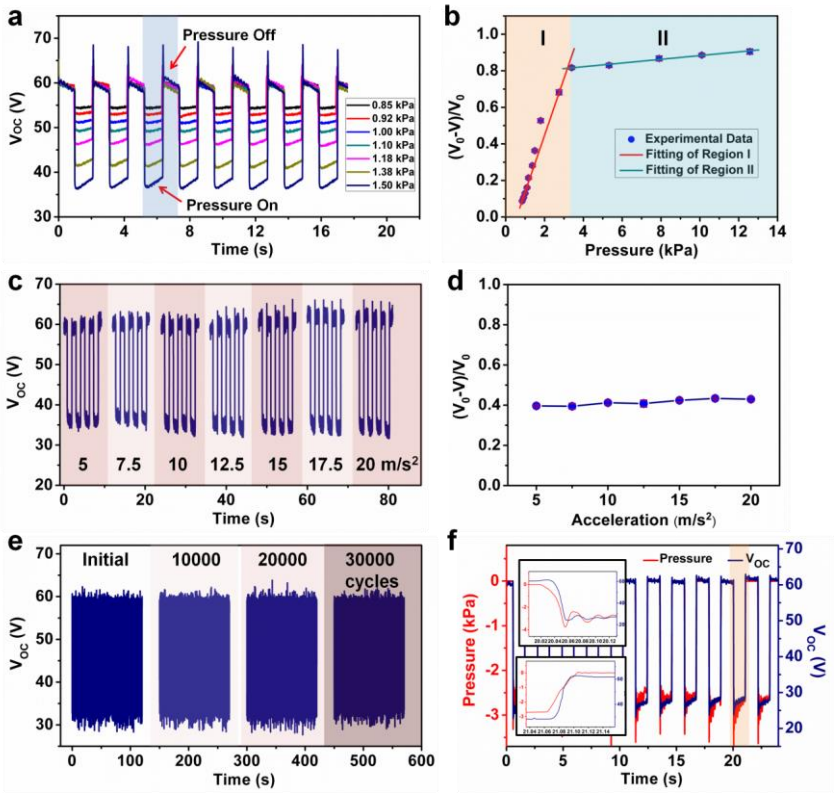

Figure 5.10 The static pressure sensing of the TEAS through measurement of the open-circuit voltage. (a) The real-time measurement of the V_{OC} with cyclic and variable pressures applied on the TEAS device. The highlighted region indicates one cycle of the pressure loading and unloading process. (b) The summarized relationship and linear fitting between the relative variations of voltage and the pressure applied on the TEAS device. (c) The measurement of the V_{OC} with a cyclic and constant pressure (2 kPa) applied on the TEAS with variable accelerations. (d) The summarized relationship between the relative voltage variations and accelerations. (e) The stability test for static pressure sensing of the TEAS with continuous loading and unloading a cyclic pressure (2.5 kPa) for 30,000 cycles. The V_{OC} was measured after each 10,000 cycles and 300 cycles of data were recorded and presented in the plot. (f) The comparison of the real-time measurement of both the applied pressure (red curve) and the V_{OC} (blue curve). The top inset and bottom inset are the enlarged view of the loading and unloading process in the highlighted cycle, respectively. The response/relaxation times are < 5 ms from the time interval of the two curves.[67]

Furthermore, beside the V_{OC}, the $\Delta\sigma$ was also a reliable parameter that could be used for static pressure sensing. In this aspect, the similar measurements were then carried out with variable pressures loaded on the TEAS device, and the data of the $\Delta\sigma$

was recorded and displayed in the same way. Different from the V_{OC}, the $\Delta\sigma$ is 0 without pressure and increases as the applied pressure is elevated. Similarly, the relationship of the $\Delta\sigma$ with increasing pressure also has two different sensitivity regions: a high sensitivity region at lower pressures and a drastically decreased sensitivity at higher pressures. The acceleration dependence at constant loading pressure was measured, and the amount of $\Delta\sigma$ also keeps constant with variable accelerations of the linear motor, though small variation exists. The stability of this type of measurement was confirmed by continuously loading and unloading a constant pressure of 2.5 kPa for 30,000 cycles.

Different from the V_{OC} and the $\Delta\sigma$, the J_{SC} is not only dependent on the applied force/pressure, but also related to the loading rate of the external force, as discussed in Eq. (3) above. Furthermore, the output profile of the J_{SC} is a pulse-like current peak, which enables its application for dynamic pressure detection. Based on this expectation, both the effect of the force/pressure magnitude and the acceleration were tested on the TEAS for peak current measurement. The measured rectified J_{SC} with variable pressures under the same loading rate were displayed in Figure 5.11a, showing a clearly increasing trend with elevated pressures. The full data summarized in Figure 5.11b shows the reversibility of the current response. The loading pressure was first increased from low pressure region (< 1 kPa) to a high pressure region (~ 9 kPa), and then decreased to the original magnitude. The resulted current response in the decreasing-pressure curve does not exhibit much deviation in reference to the original curve, thus demonstrating the reliability of the current measurement. Similarly, the current response with a constant pressure (0.75 kPa) and variable accelerations was measured and shown in Figure 5.11c-d. The peak values of the output J_{SC} also have positive correlation with the acceleration of

the applied pressure. Both the relationship between the peak value of the J_{SC} and the applied pressure/acceleration could be explained using Eq. (3), where the loading rate $\delta d/\delta t$ is positively related to the acceleration of the linear motor. Therefore, with increasing applied pressure or acceleration, the term d will decrease or $\delta d/\delta t$ will increase, both leading to the enhancement of the absolute value of the J_{SC}.

Furthermore, the cycling stability test of the rectified J_{SC} under continuous pressure triggering for 30,000 cycles was carried out in the same way as the test of the V_{OC}, and little decay could be found in the measurement results (Figure 5.11e). In addition, the dynamic reliability of the TEAS was further confirmed by recording the peak current response with variable pressures after every 10,000 triggering cycles. The results shown in Figure 5.11f also demonstrates that the measured J_{SC}-pressure relationship after continuous triggering is close to the original test. More impressively, the dynamic pressure sensing limit of the TEAS was examined by comparing the output signals of both a gentle pressure (0.125 kPa) and the corresponding noise level. The low-end detection limit (p_0) of the TEAS is then calculated by the following equation:

$$p_0 = \frac{p}{J_{SC}/J_{SC,noise}} = \frac{0.125}{0.15/0.0025} kPa = 2.1Pa \tag{5.6}$$

the low-end detection limit of the TEAS is merely 2.1 Pa, elaborating the high sensitivity of the nanogenerator as an active pressure sensor.

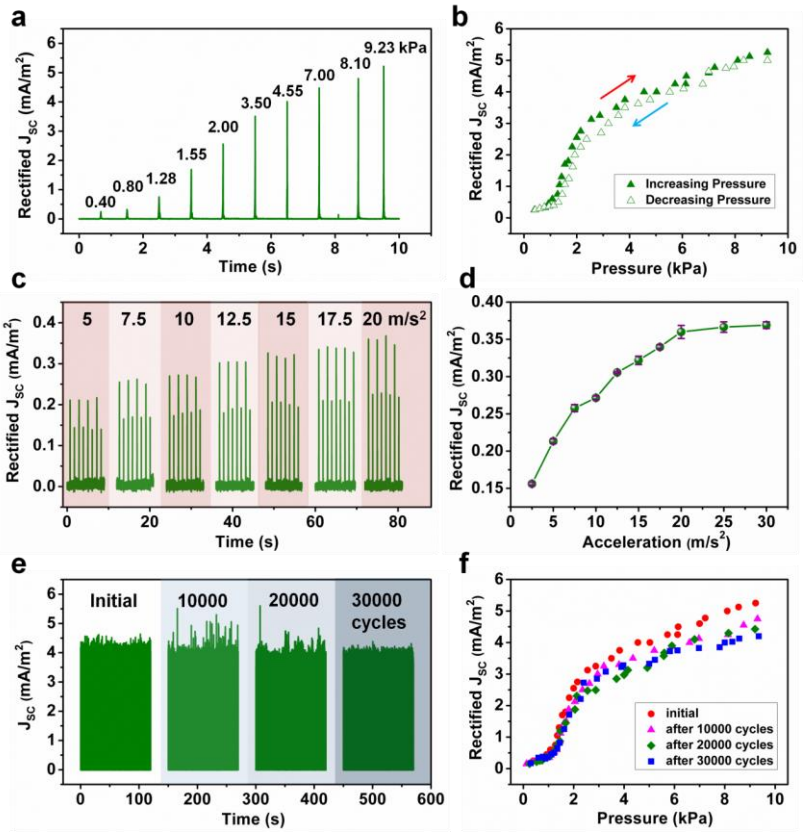

Figure 5.11 Dynamic pressure sensing of the TEAS through measurement of the short-circuit current density. (a) The measured rectified pulse-like J_{SC} with variable pressures applied on the TEAS device. (b) The summarized data of the rectified J_{SC} with variable pressures applied on the TEAS device and the reversibility test by increasing the pressure in the first test cycle and decreasing the pressure in the second test cycle. (c) The measured rectified J_{SC} with a constant pressure (0.75 kPa) applied on the TEAS device but with variable accelerations. (d) The summarized data of the rectified J_{SC} with a constant pressure but with variable accelerations ranging from 2.5 to 30 m/s^2. (e) The stability test for dynamic pressure sensing of the TEAS with continuous loading and unloading for 30,000 cycles. The J_{SC} was measured after each 10,000 cycles and 300 cycles of data were recorded and presented in the plot. (f) The reliability test of the dynamic pressure sensing. The measurement of the rectified J_{SC} with variable pressures was carried out after each 10,000 cycles and compiled in the same plot.[67]

Above all, it could be clearly found that the high sensitivity range of the TEAS is confined within a low pressure region (< 5 kPa), as both the voltage and current signal tends to get saturated when the pressure reaches a higher level. This performance might limit the practical applications of the TEAS, and the extension of higher detection range

is highly desirable. In this regard, we designed a new type of TEAS with the original device entangled by a plastic bracket with elastic springs to enforce the whole structure. Based on this newly fabricated device, the voltage, charge transfer, and current responses of the TEAS with variable pressures were measured. From the summarized results, we can find that the linear and high sensitivity region has been expanded to ~ 40 kPa.

5.4 Triboelectric pressure sensor array for self-powered tactile imaging

The array of the TEAS devices was fabricated on a flat plate with deposited Al thin film as a common electrode, as schematically illustrated in Figure 5.12a. The unit of the array device has the same size as the single TEAS device mentioned above. Each pixel was marked the letter/number coordinates from "A1" to "F6". The response of the TEAS array with local pressure was measured through a multi-channel measurement system (National Instruments). The Al electrodes of all the TEAS units were connected to a common electrode on the plate with conductive paste, while the upper Au electrode of each unit was connected to the probe of each measurement channel. The measurement instrument is a voltage meter with an internal resistance of ~ 10 MΩ, and a corresponding voltage peak will be recorded as response of a local pressure on the corresponding TEAS unit in the matrix. For example, a quarter of pixels (Pixels A1-C3) in the array were pressed simultaneously, and the voltage peaks were only detected from Pixels A1-C3, while the output profile of the other channels remain almost unchanged in the same time period.

Based on this working principle, we demonstrated the tactile imaging capability of the TEAS matrix by loading pressure through pre-designed plastic architecture with

the calligraphy of the letters “TENG”, respectively. Before applying the pressure, the voltage outputs from all the pixels of the TEAS matrix were at the background level, as displayed in Figure 5.12b. Figures 5.12c-f shows the two-dimensional contour plotting of the peak value of the voltage responses that were measured when external pressures were applied through each architecture, respectively. The highlighted color represents the area under pressing through each letter, as outlined by the white dash lines. These plots elaborate the spatial resolution of the TEAS matrix for distinguishably mapping the calligraphy of the applied pressure, and its potential applications such as personal signature recognition. In addition, to gain a more intuitive understanding of the “self-powered” pressure mapping functionality of the TEAS matrix, each nine units of the same array device were connected in parallel to power up a serially-connected array of LEDs showing “T”, “E”, “N”, “G” characters, respectively. This demonstration proves that the TEAS matrix can work as an external power source and a sensor array simultaneously for a truly stand-alone self-powered system.

The active pressure sensor and the integrated sensor array based on the triboelectric effect presented in this work have several advantages over conventional passive pressure sensors. First, the active sensor in this work is capable of both static pressure sensing using the open-circuit voltage and dynamic pressure sensing using the short-circuit current, while conventional sensors are usually incapable of dynamic sensing to provide the loading rate information. Second, the prompt response of both static and dynamic sensing enables the revealing of details about the loading pressure. Third, the detection limit of the TEAS for dynamic sensing is as low as 2.1 Pa, owing to the high output of the TENG. Last but not least, the active sensor array presented in this

work has no power consumption and could even be combined with its energy harvesting functionality for self-powered pressure mapping. Future works in this field involve the miniaturization of the pixel size to achieve higher spatial resolution, and the integration of the TEAS matrix onto fully flexible substrate for shape-adaptive pressure imaging.

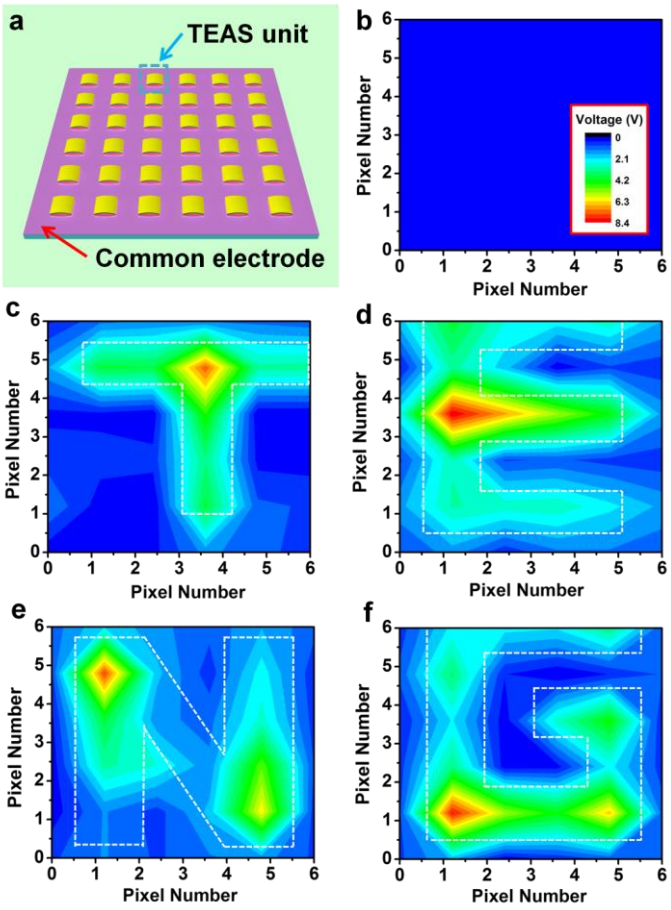

Figure 5.12 Self-powered pressure mapping based on the TEAS array. (a) A schematic illustration of the TEAS array device. (b) The background signal with no pressure applied on the TEAS matrix. The inset is color scaling of voltage for all the measurements in this figure. (c-f) The two-dimensional voltage contour plot from the multi-channel measurement of the TEAS matrix with an external pressure uniformly and locally applied onto the device through architectures with calligraphy of "T", "E", "N", and "G", respectively.[67]

In summary, a self-powered, highly sensitive, and fast responsive pressure sensor was demonstrated based on the triboelectric effect. The performance of the triboelectric

active sensor was characterized by static sensing with the open-circuit voltage, and dynamic sensing with the short-circuit current. The long-term stability, cycling repeatability, as well as adjustable sensing range were realized owing to the robustness of the active pressure sensor. Multiple triboelectric active sensors were integrated into a sensor array for self-powered pressure mapping, and spatially distinguishable tactile imaging was demonstrated. This work is a milestone progress in nanogenerator-based active sensor, which not only realizes its energy harvesting and pressure sensing functionalities at the same time, but also initiates possible applications such as personal signature recognition or electronic skins.

CHAPTER 6

CONCLUSIONS

In this dissertation, I have presented my major research achievements in the past five years as a PhD student and a graduate research assistant at Georgia Tech. My major goal is to improve the output performance of nanogenerators for harvesting the ambient mechanical energy. The enhanced performance of both piezoelectric and triboelectric nanogenerators can be employed to power up small-scale electronic devices or integrated with energy storage unit for self-powered system. Taking advantage of the relationship between the mechanical input and electric output, the nanogenerators could also be employed as self-powered sensors to active detect the changes of external stimuli including pressure, motion, vibration, etc. In this chapter, my research achievements and technological innovations are summarized, and several suggestions on future works in this field are given for those who will continue investigations in nanogenerators.

6.1 Improvement of piezoelectric nanogenerators

Preceding this endeavor, ZnO-based piezoelectric nanogenerator had been studied for five years, but its output voltage and current was limited to about 2 V and 50 nA, which was not sufficient to power up electronic devices. In this regard, vertical integration of single-wire-nanogenerators was fulfilled by synthesizing ZnO nanowires directly on flexible PDMS substrate through wet chemical approach. Furthermore, several approaches were also adopted to reduce the free carrier density of the n-type

nanowires including oxygen plasma treatment, thermal annealing, and surface functionalization. The output voltage of the piezoelectric nanogenerator was boosted up to 20 V, with a volume power density of 0.2 W/cm^3. The high output was sufficient to drive a buck converter board for continuously powering an electronic watch, which presented a significant step towards the application of piezoelectric nanogenerators in real-world situations.

6.2 Improvement of triboelectric nanogenerators

The development of triboelectric nanogenerators is the core part of my thesis research, and I have completed several pioneering works since the first invention of this new energy technology. The working principle of the TENG was successfully clarified, and four fundamental working modes were subsequently developed to accommodate different types of mechanical energy harvesting. Many prototypes have been designed and fabricated, such as the arch-shaped structure, the linear-sliding structure, the rotary disk structure, and stretchable-polymer-based structure, and so on. With these advanced structural designs and micro-patterned surface modifications, the output power density of the TENG has been enhanced up to 35.6 W/m^2, with a high open-circuit current of 1200 V, an excellent energy conversion efficiency of 55%, and outstanding device durability of over 300,000 cycles. TENGs were enabled to scavenge mechanical energy from versatile power sources, including vibration, finger typing, walking, tire rotation, wind, hydropower, etc.

6.3 Nanogenerators for self-powered system

The concept of self-powered system has been established since 2008. By integrating nanogenerators with functional electronic devices, the entire system will be able to work effectively without external power supply. In my research, the improved piezoelectric nanogenerator could be enabled to directly power up a liquid crystal display, and it could also be integrated with a buck converter board to drive an electronic watch. The enhanced triboelectric nanogenerator could instantaneously power up light-emitting diodes. Its high output could also be integrated with a lithium ion battery to power up commercial wireless sensors. Furthermore, a self-powered smart window system was constructed that consisted of a transparent TENG and an electrochromic device. The TENG was utilized to harvesting wind or raindrop energy to power up the electrochromic device, and a reversible change of its optical property was achieved with a transmittance difference of up to 36.2%. The concept of self-powered system has revealed its promising applicability in sensor networks, implanted devices, and smart buildings and infrastructures.

6.4 Nanogenerators as active sensors

Taking advantage of the strong relationship between the mechanical input and electrical output signals, nanogenerators were employed as self-powered active sensor to detect and measure the external mechanical stimuli. In this regard, a transparent flexible piezoelectric nanogenerator was utilized to monitor the speed and weight of a moving vehicle on the road; and a spring-based piezoelectric nanogenerator could be directly

employed as a self-powered balance. Furthermore, owing to the high output performance of triboelectric nanogenerators, a self-powered pressure sensor with superior high sensitivity (0.31 kPa^{-1}) and low detection limit (2.1 Pa) was accomplished. Multiple sensor units were also integrated into an array structure to measure the pressure distribution over the sensor array, and the applied pressure could be clearly mapped with multi-channel measurement.

6.5 Future works

Though advancements have been made to improve nanogenerators as an effective mechanical energy harvesting approach, some problems still remain to be solved to make this technology applicable as commercial product. To assist future research in this field, the problems and suggested investigation topics are summarized as follows.

(1) The fundamental understanding of contact electrification still needs clarification. Despite of its effect in charge generation, the underlying physics of this phenomenon is still not clear, and it will be vitally important to fully disclose the mechanism or process of electrification, with which optimized performance of TENG could be realized.

(2) A reliable packaging technology is highly desirable to make a compact device available to work in harsh environment. This may be a challenge since there must be moving part in the TENG device.

(3) A power transforming system is required to bring down the output voltage and improve the output current of the TENG. TENG usually displays huge output voltage up to thousands of volts, but it is not necessary, while the output current is still lower than those of solar cells or thermoelectric cells. Hence, such a power transformation technology with low energy loss is indispensable for integration with functional devices.

(4) Improving the spatial resolution of TENG-based self-powered pressure sensor array is also a major task to move this technology forward. The current resolution is still low due to the large size of the TENG unit. Miniaturization of the TENG device by microfabrication would be the initial step to accomplish high spatial resolution of the pressure mapping array.

REFERENCES

1. Hammond, A. L. *Science* **1977,** 195, 564-566.

2. Barnham, K.; Mazzer, M.; Clive, B. *Nat. Mater.* **2006,** 5, 161-164.

3. Atzori, L.; Iera, A.; Morabito, G. *Computer Networks* **2010,** 54, 2787-2805.

4. Gershenfeld, N.; Krikorian, R.; Cohen, D. *Sci. Am.* **2004,** 291, 76.

5. Carlson, D. E.; Wronski, C. *Appl.Phys. Lett.* **1976,** 28, 671-673.

6. Hagfeldt, A.; Boschloo, G.; Sun, L.; Kloo, L.; Pettersson, H. *Chem. Rev.* **2010,** 110, 6595-6663.

7. Law, M.; Greene, L. E.; Johnson, J. C.; Saykally, R.; Yang, P. *Nat. Mater.* **2005,** 4, 455-459.

8. Chen, T.; Barton, S. C.; Binyamin, G.; Gao, Z.; Zhang, Y.; Kim, H.-H.; Heller, A. *J. Am. Chem. Soc.* **2001,** 123, 8630-8631.

9. Willner, I.; Yan, Y. M.; Willner, B.; Tel-Vered, R. *Fuel Cells* **2009,** 9, 7-24.

10. Logan, B. E.; Murano, C.; Scott, K.; Gray, N. D.; Head, I. M. *Water Research* **2005,** 39, 942-952.

11. Hochbaum, A. I.; Chen, R.; Delgado, R. D.; Liang, W.; Garnett, E. C.; Najarian, M.; Majumdar, A.; Yang, P. *Nature* **2008,** 451, 163-167.

12. Snyder, G. J.; Toberer, E. S. *Nat. Mater.* **2008,** 7, 105-114.

13. Venkatasubramanian, R.; Siivola, E.; Colpitts, T.; O'quinn, B. *Nature* **2001,** 413, 597-602.

14. Fang, H.-B.; Liu, J.-Q.; Xu, Z.-Y.; Dong, L.; Wang, L.; Chen, D.; Cai, B.-C.; Liu, Y. *Microelectr. J.* **2006,** 37, 1280-1284.

15. Glynne-Jones, P.; Beeby, S. P.; White, N. M. *IEE Proc. A* **2001,** 148, 68-72.

16. Jeon, Y.; Sood, R.; Jeong, J.-H.; Kim, S.-G. *Sensor Actuat. A-Phys.* **2005,** 122, 16-22.

17. Liu, J.-Q.; Fang, H.-B.; Xu, Z.-Y.; Mao, X.-H.; Shen, X.-C.; Chen, D.; Liao, H.; Cai, B.-C. *Microelectr. J.* **2008,** 39, 802-806.

18. Shearwood, C.; Yates, R. B. *Electr. Lett.* **1997,** 33, 1883-1884.

19. Beeby, S. P.; Torah, R.; Tudor, M.; Glynne-Jones, P.; O'Donnell, T.; Saha, C.; Roy, S. *J. Micromech. Microeng.* **2007,** 17, 1257.

20. Glynne-Jones, P.; Tudor, M. J.; Beeby, S. P.; White, N. M. *Sensor Actuat. A-Phys.* **2004,** 110, 344-349.

21. Van De Graaff, R. J. *Phys. Rev.* **1931,** 38, 1919-1920.

22. Tashiro, R.; Kabei, N.; Katayama, K.; Ishizuka, Y.; Tsuboi, F.; Tsuchiya, K. *JSME Int. J. C-Mech. Sy.* **2000,** 43, 916-922.

23. Tashiro, R.; Kabei, N.; Katayama, K.; Tsuboi, E.; Tsuchiya, K. *J. Artif. Org.* **2002,** 5, 0239-0245.

24. Saha, C.; O'donnell, T.; Wang, N.; McCloskey, P. *Sensor. Actuat. A-Phys.* **2008,** 147, 248-253.

25. Suzuki, Y.; Miki, D.; Edamoto, M.; Honzumi, M. *J. Micromech. Microeng.* **2010,** 20, 104002.

26. Wang, Z. L.; Song, J. *Science* **2006,** 312, 242-246.

27. Wang, X.; Song, J.; Liu, J.; Wang, Z. L. *Science* **2007,** 316, 102-105.

28. Qin, Y.; Wang, X.; Wang, Z. L. *Nature* **2008,** 451, 809-813.

29. Yang, R.; Qin, Y.; Dai, L.; Wang, Z. L. *Nat. Nanotechnol.* **2009,** 4, 34-39.

30. Zhu, G.; Yang, R.; Wang, S.; Wang, Z. L. *Nano Lett.* **2010,** 10, 3151-3155.

31. Xu, S.; Qin, Y.; Xu, C.; Wei, Y.; Yang, R.; Wang, Z. L. *Nat. Nanotechnol.* **2010,** 5, 366-373.

32. Hu, Y.; Zhang, Y.; Xu, C.; Zhu, G.; Wang, Z. L. *Nano Lett.* **2010,** 10, 5025-5031.

33. Hu, Y.; Zhang, Y.; Xu, C.; Lin, L.; Snyder, R. L.; Wang, Z. L. *Nano Lett.* **2011,** 11, 2572-2577.

34. Lin, L.; Hu, Y.; Xu, C.; Zhang, Y.; Zhang, R.; Wen, X.; Wang, Z. L. *Nano Energy* **2013,** 2, 75-81.

35. Gao, Y.; Wang, Z. L. *Nano Lett.* **2007,** 7, 2499-2505.

36. Gao, Y.; Wang, Z. L. *Nano Lett.* **2009,** 9, 1103-1110.

37. Hu, Y.; Lin, L.; Zhang, Y.; Wang, Z. L. *Adv. Mater.* **2012,** 24, 110-114.

38. Gopel, W. *Prog. Surf. Sci.* **1985,** 20, 9-103.

39. Gulino, D.; Kren, L.; Dever, T. *Thin Solid Films* **1990,** 188, 237-246.

40. Park, W. I.; Kim, J. S.; Yi, G.-C.; Bae, M.; Lee, H.-J. *Appl. Phys. Lett.* **2004,** 85, 5052-5054.

41. Huang, C.-T.; Song, J.; Lee, W.-F.; Ding, Y.; Gao, Z.; Hao, Y.; Chen, L.-J.; Wang, Z. L. *J. Am. Chem. Soc.* **2010,** 132, 4766-4771.

42. Lin, Y.-F.; Song, J.; Ding, Y.; Lu, S.-Y.; Wang, Z. L. *Appl. Phys. Lett.* **2008,** 92, 022105.

43. Huang, C. T.; Song, J.; Tsai, C. M.; Lee, W. F.; Lien, D. H.; Gao, Z.; Hao, Y.; Chen, L. J.; Wang, Z. L. *Adv. Mater.* **2010,** 22, 4008-4013.

44. Lin, L.; Lai, C.-H.; Hu, Y.; Zhang, Y.; Wang, X.; Xu, C.; Snyder, R. L.; Chen, L.-J.; Wang, Z. L. *Nanotechnology* **2011,** 22, 475401.

45. Castle, G. *J. Electrost.* **1997,** 40, 13-20.

46. Duke, C.; Fabish, T. *J. Appl. Phys.* **1978,** 49, 315-321.

47. Horn, R. G.; Smith, D. T. *Science* **1992,** 256, 362.

48. Fan, F.-R.; Tian, Z.-Q.; Wang, Z. L. *Nano Energy* **2012,** 1, 328-334.

49. Zhu, G.; Zhou, Y. S.; Bai, P.; Meng, X. S.; Jing, Q.; Chen, J.; Wang, Z. L. *Adv. Mater.* **2014,** 26, 3788-3796.

50. Tang, W.; Jiang, T.; Fan, F. R.; Yu, A. F.; Zhang, C.; Cao, X.; Wang, Z. L. *Adv. Funct. Mater.* **2015**, 25, 3718-3725.

51. Xie, Y.; Wang, S.; Niu, S.; Lin, L.; Jing, Q.; Yang, J.; Wu, Z.; Wang, Z. L. *Adv. Mater.* **2014,** 26, 6599-6607.

52. Jing, Q.; Zhu, G.; Bai, P.; Xie, Y.; Chen, J.; Han, R. P. S.; Wang, Z. L. *ACS Nano* **2014,** 8, 3836-3842.

53. Yang, W.; Chen, J.; Zhu, G.; Yang, J.; Bai, P.; Su, Y.; Jing, Q.; Cao, X.; Wang, Z. L. *ACS Nano* **2013,** 7, 11317-11324.

54. Yang, W.; Chen, J.; Zhu, G.; Wen, X.; Bai, P.; Su, Y.; Lin, Y.; Wang, Z. *Nano Res.* **2013,** 6, 880-886.

55. Yang, J.; Chen, J.; Yang, Y.; Zhang, H.; Yang, W.; Bai, P.; Su, Y.; Wang, Z. L. *Adv. Energy Mater.* **2014,** 4, 1301322.

56. Yang, W.; Chen, J.; Jing, Q.; Yang, J.; Wen, X.; Su, Y.; Zhu, G.; Bai, P.; Wang, Z. L. *Adv. Funct. Mater.* **2014,** 24, 4090-4096.

57. Zhu, G.; Lin, Z.-H.; Jing, Q.; Bai, P.; Pan, C.; Yang, Y.; Zhou, Y.; Wang, Z. L. *Nano Lett.* **2013,** 13, 847-853.

58. Lin, L.; Wang, S.; Niu, S.; Liu, C.; Xie, Y.; Wang, Z. L. *ACS Appl. Mater. Interfaces* **2014,** 6, 3031-3038.

59. Lin, L.; Wang, S.; Xie, Y.; Jing, Q.; Niu, S.; Hu, Y.; Wang, Z. L. *Nano Lett.* **2013,** 13, 2916-2923.

60. Zhu, G.; Chen, J.; Zhang, T.; Jing, Q.; Wang, Z. L. *Nat. Commun.* **2014,** 5, 3426.

61. Xie, Y.; Wang, S.; Lin, L.; Jing, Q.; Lin, Z.-H.; Niu, S.; Wu, Z.; Wang, Z. L. *ACS Nano* **2013,** 7, 7119-7125.

62. Yang, Y.; Zhu, G.; Zhang, H.; Chen, J.; Zhong, X.; Lin, Z.-H.; Su, Y.; Bai, P.; Wen, X.; Wang, Z. L. *ACS Nano* **2013,** 7, 9461-9468.

63. Bae, J.; Lee, J.; Kim, S.; Ha, J.; Lee, B.-S.; Park, Y.; Choong, C.; Kim, J.-B.; Wang, Z. L.; Kim, H.-Y.; Park, J.-J.; Chung, U. I. *Nat. Commun.* **2014,** 5, 4929.

64. Lin, Z.-H.; Cheng, G.; Lin, L.; Lee, S.; Wang, Z. L. *Angew. Chem. Int. Ed.* **2013,** 125, 12777-12781.

65. Lin, Z.-H.; Cheng, G.; Lee, S.; Pradel, K. C.; Wang, Z. L. *Adv. Mater.* **2014,** 26, 4690-4696.

66. Zhu, G.; Su, Y.; Bai, P.; Chen, J.; Jing, Q.; Yang, W.; Wang, Z. L. *ACS Nano* **2014,** 8, 6031-6037.

67. Lin, L.; Xie, Y.; Wang, S.; Wu, W.; Niu, S.; Wen, X.; Wang, Z. L. *ACS Nano* **2013,** 7, 8266-8274.

68. Yang, Y.; Zhang, H.; Lin, Z.-H.; Zhou, Y. S.; Jing, Q.; Su, Y.; Yang, J.; Chen, J.; Hu, C.; Wang, Z. L. *ACS Nano* **2013,** 7, 9213-9222.

69. Yang, W.; Chen, J.; Wen, X.; Jing, Q.; Yang, J.; Su, Y.; Zhu, G.; Wu, W.; Wang, Z. L. *ACS Appl. Mater. Interfaces* **2014,** 6, 7479-7484.

70. Fan, F.-R.; Lin, L.; Zhu, G.; Wu, W.; Zhang, R.; Wang, Z. L. *Nano Lett.* **2012,** 12, 3109-3114.

71. Chen, J.; Zhu, G.; Yang, J.; Jing, Q.; Bai, P.; Yang, W.; Qi, X.; Su, Y.; Wang, Z. L. *ACS Nano* **2015,** 9, 105-116.

72. Zhu, G.; Yang, W. Q.; Zhang, T.; Jing, Q.; Chen, J.; Zhou, Y. S.; Bai, P.; Wang, Z. L. *Nano Lett.* **2014,** 14, 3208-3213.

73. Tang, W.; Han, Y.; Han, C. B.; Gao, C. Z.; Cao, X.; Wang, Z. L. *Adv. Mater.* **2015,** 27, 272-276.

74. Wen, X.; Yang, W.; Jing, Q.; Wang, Z. L. *ACS Nano* **2014,** 8, 7405-7412.

75. Zhu, H. R.; Tang, W.; Gao, C. Z.; Han, Y.; Li, T.; Cao, X.; Wang, Z. L. *Nano Energy* **2015**, 14, 193-200.

76. Baytekin, H.; Patashinski, A.; Branicki, M.; Baytekin, B.; Soh, S.; Grzybowski, B. A. *Science* **2011,** 333, 308-312.

77. Terris, B.; Stern, J.; Rugar, D.; Mamin, H. *Phys. Rev. Lett.* **1989,** 63, 2669.

78. McCarty, L. S.; Whitesides, G. M. *Angew. Chem. Int. Ed.* **2008,** 47, 2188-2207.

79. Lowell, J.; Rose-Innes, A. *Adv. Phys.* **1980,** 29, 947-1023.

80. Wang, Z. L. *Faraday Discuss.* **2014,** 176, 447-458.

81. Wang, S.; Lin, L.; Wang, Z. L. *Nano Lett.* **2012,** 12, 6339-6346.

82. Wang, S.; Lin, L.; Xie, Y.; Jing, Q.; Niu, S.; Wang, Z. L. *Nano Lett.* **2013,** 13, 2226-2233.

83. Lin, L.; Xie, Y.; Niu, S.; Wang, S.; Yang, P.-K.; Wang, Z. L. *ACS Nano* **2015,** 9, 922-930.

84. Yang, P. K.; Lin, L.; Yi, F.; Li, X.; Pradel, K. C.; Zi, Y.; Wu, C. I.; He Jr, H.; Zhang, Y.; Wang, Z. L. *Adv. Mater.* **2015**.

85. Wang, Z. L. *Sci. Am.* **2008,** 298, 82-87.

86. Wang, Z. L. In *Self-powered nanosystem: From nanogenerators to piezotronics*, Solid-State and Integrated Circuit Technology (ICSICT), 2010 10th IEEE International Conference on, 2010; IEEE: pp 4-4.

87. Wang, Z. L. *ACS Nano* **2013,** 7, 9533-9557.

88. Yeh, M.-H.; Lin, L.; Yang, P.-K.; Wang, Z. L. *ACS Nano* **2015**.

89. Lin, L.; Jing, Q.; Zhang, Y.; Hu, Y.; Wang, S.; Bando, Y.; Han, R. P.; Wang, Z. L. *Energy Environ. Sci.* **2013,** 6, 1164-1169.

VITA

LONG LIN

LONG LIN was born in Dalian, Liaoning, P. R. China. He attended Tsinghua University, Beijing, P. R. China, where he received a Bachelor of Engineering in Materials Science and Engineering in 2010. He then went to begin his doctoral research and study in School of Materials Science and Engineering at Georgia Institute of Technology, under the supervision of Prof. Zhong Lin Wang in 2010. Long Lin's research interests include semiconductor nanomaterials, mechanical energy harvesting, self-powered system, and active sensors. When he is not working on his research, Long enjoys sports, hiking, and traveling.